Author:
Klinger, Adam G

Title:
Insights into the rupture physics and geomechanics of microseismicity induced during hydraulic fracturing operations

Insights into the rupture physics and geomechanics of microseismicity induced during hydraulic fracturing operations

By

ADAM G. KLINGER

School of Earth Sciences
UNIVERSITY OF BRISTOL

A dissertation submitted to the University of Bristol in accordance with the requirements of the degree of DOCTOR OF PHILOSOPHY in the Faculty of Sciences.

MARCH 2022

Word count: 29479

Abstract

Exploiting the subsurface through high pressure injection of fluids is used for multiple geo-energy industrial activities, including enhanced geothermal systems, waste water disposal and hydraulic fracturing. However, earthquakes caused by industrial activity are of concern to the government, operators and the public. In the U.K. hydraulic fracturing activities were banned as a result of induced earthquakes in 2019. Injection activities continue in Cornwall as part of a geothermal project, which are causing felt earthquakes. Induced earthquakes offer a unique controlled environment to ask scientific questions about the rupture physics of earthquakes and to inform mitigation strategies to reduce the risks of injection induced earthquakes.

In this thesis I use induced seismicity to ask some fundamental questions about the rupture physics of tiny earthquakes (i.e., $M_w \leq 0.6$). I use a dataset of high quality microseismic events collected during hydraulic fracturing operations in the Horn River basin, Canada, and exploit the borehole-geophone setup, which is near the reservoir, to probe seismic events at high frequencies (i.e., > 200 Hz). I focus on the largest seismic events which are linked to a re-activated structure that extends from the stimulated shale into the underlying crystalline basement. These events show the clearest phase arrivals and the best signal to noise ratio.

Using the data, I first analyse the nature of the geophone response to noise and signal. In chapter 2 I show that the resonances and high frequency compromising effects of geophones significantly hamper our ability to produce sub-catalogues of high frequency source parameters. Such features were not easily noticeable but are likely to be common in studies that use a borehole geophone setup when monitoring microsiesmicity. Here I document systematic resonance features and interpret them as near-receiver effects, although the exact provenance is still unclear. I also observe high frequency cut-offs, which can in turn generate spurious source parameter estimates, resulting in an apparent scaling of stress drop with M_w. Spectral ratios account for resonances better than using the raw geophone signals but do not eradicate resonances completely. My observations have been documented empirically and theoretically by others as an issue when probing high frequency microseismic events using borehole geophones and our results support these studies.

The results from Chapters 2 and 4 contribute to our understanding of how earthquake ruptures scale. Smaller earthquakes hosted within shallower crust are expected to have a lower stress drop budget than deeper tectonic earthquakes. I show that there is no evidence that challenges the independence of stress drop with magnitude (self-similarity). The absolute stress drops and rupture radii I calculate are consistent with those expected if tectonic earthquakes are scaled down to a microseismic size. However, the results also highlight the epistemic uncertainty in stress drop resulting from the chosen method, which in this case leads to an average stress drop that is twice as large when using spectral ratios compared to directly fitting source models, as reported from other datasets as well.

I investigate the spatio-temporal variation of stress drops within the studied dataset and test the hypothesis that stress drop decreases from the point of injection, as observed in other datasets. In Chapters 2 and 4 I show that using two independent methods for estimating stress drop, there is no signal of an increasing stress drop with distance from the injection point (which is unexpected if differential stresses decrease near to the injection point). One plausible explanation for this empirical observation is that the injected fluids diffuse relatively quickly along the fault zone, thereby decreasing effective stresses over a larger spatial footprint in a shorter amount of time compared to other settings. My interpretation is consistent with a previous study of the same dataset which shows that additional pore pressure most likely drives the fault to failure.

A closer temporal analysis of the stress drop variations within clusters of co-located and highly cross-correlated events (Chapter 4) reveals that although the average stress drop is stable with respect to distance from injection there are large variations within these clusters within short time periods. A plausible explanation is that small scale pore pressure differences could cause significant differences in stress drop. However, many different theories used to explain empirical observations of stress drop differences in other datasets such as fault roughness, fault strength and small pore pressure differences could also explain these variations. Future research that provides a controlled lab study on how stress drop varies when fault properties are systematically changed would be a greatly beneficial reference for interpreting the signals of stress drop from datasets.

I delve further into the geomechanics of the fault structure in Chapter 3 with particular focus on the Fault Slip Potential (FSP) model, which has been used by others to identify which structures are critically primed for failure. My observations show very large uncertainties in the amount of additional pore pressure that an operator might use as a guiding upper limit when perturbing a reservoir. Here, I highlight the large uncertainties linked to the choice of the maximum principal stress direction one believes is affecting a reservoir, when deferring to data from the world stress map. Such uncertainties preclude robust calculations of fault stability estimates before any drilling has occurred. In-situ measurements of the maximum principal stress reduce the uncertainty in fault stability estimates and are preferable. However, the small scale variations of the maximum principal stress direction, even within the same reservoir, may still result in significant uncertainty of fault stability estimates for fault planes hosted in rocks which are below the reservoir, in the case of hydraulic fracturing of tight shales.

I show that stress drops can reveal interesting observations about the nature of induced seismicity during subsurface geo-energy exploitation. However, the paucity of high quality stress drop measurements, which is linked to the difficulties when accurately resolving high frequencies along a borehole geophone array, makes interpreting the empirical observations more difficult. I also question the confidence that we have when estimating how stable fault structures before, and during a subsurface geo-energy operation, which varies significantly depending on the tectonic length scales one believes is acting on the structure. Future studies will benefit from a better understanding of how sensitive stress drop signals are to the various attributes of a fault, wider azimuthal coverage during an operation and more in-situ measurements to characterise the stress state of a reservoir and the underlying basement.

Dedication and acknowledgements

I would like to thank Max Werner for being a great supervisor. None of this would have been possible without the tutoring and guidance that I received throughout the Ph.D from Max. I am thankful for the many, many hours of looking at figures, editing my manuscripts, helping me develop ideas, and being an all-round easy person to talk to. My enthusiasm for the earthquake problem has been significantly increased by Max's enthusiasm and the inspiring research environment that Max fosters within the research group.

I also must thank Joanna Holmgren for her expertise and support. In many ways it was a god send to have Joanna join the research group just as I was getting into methods used in my last chapter. I thank her for the many meetings where we would often stare at similar figures, to the point when any sane person would surely start to seriously question life choices. I also thank her for the moral support which helped pep me up at times when I really needed it.

Thanks to James Wookey, Mike Kendall and Heidi Mader for the annual guidance during my APM meetings. The broader views helped steer the project in the right direction.

I have been at the Earth Sciences department in Bristol now for 8.5 years. I am very lucky to have been in such a friendly and easy-going environment. Throughout my whole university experience I have felt included in a supportive atmosphere. Within the Geophysics group I have also also felt part of a friendly and easy-going group of people. The many coffee mornings and annual Christmas parties were always something to look forward to. Thanks to Alan Baird, Anthony Butcher, Tom Laurioux, Tom Kettlety, James Verdon, James Wookey, Jessica Sanchez, Nick Teanby, Mark Bemelmans, Joe Asplet, Robbie Churchill, Toño Bayona, Alex Jenkins, James Dalziel, Luke Wedmore, Melody Sylvestre, Dave Schlaphorst, Bob Myhill, Jason Sharkey, Wen Zhou and to the many others who have been and passed (through Bristol uni).

My time in Bristol is also highlighted by two other communities: the Jewish community and the capoeira community. Thanks to Bristol Chabad for providing a communal environment where I have made strong friendships. Thanks to the capoeira community for inviting me into a group where I could learn this special practise and be part of a community of people quite different to where I grew up.

Lastly I'd like to thank my family for their love and support. Throughout the Ph.D my family grounded, encouraged and supported me. It would of made it a lot harder to complete this without their support.

Author's declaration

I declare that the work in this dissertation was carried out in accordance with the requirements of the University's Regulations and Code of Practice for Research Degree Programmes and that it has not been submitted for any other academic award. Except where indicated by specific reference in the text, the work is the candidate's own work. Work done in collaboration with, or with the assistance of, others, is indicated as such. Any views expressed in the dissertation are those of the author.

SIGNED: Adam Klinger .... DATE:5th March 2022 ....

Table of Contents

List of Tables

List of Figures

CHAPTER 1

INTRODUCTION

1.1 Background to injection induced seismicity

The subsurface is consistently observed to deform in response to fluid injection, which can cause earthquakes. One relatively early example is from the disposal of contaminated wastewater into the Rocky Mountains Arsenal (Evans, 1966). 710 earthquakes were observed since the start of injection and a positive correlation between volume/pressure of fluid and the frequency of earthquakes was found. Another early example is from an injection experiment in Rangely, Colorado (Raleigh et al., 1976) where the number of earthquakes appeared to be correlated with fluid reservoir pressure.

The interest in understanding human induced seismicity is motivated by risk mitigation, geo-energy and probing earthquakes in an environment where drivers are better understood. The largest earthquake caused by conventional gas extraction is the M_w = 7 earthquake in the Urals (Simpson and Leith, 1985). Unconventional methods such as hydraulic fracturing (HF) of tight shale reservoirs made it possible to economically harness trapped gas (US Energy Information Administration, 2013) and the advent of horizontal drilling techniques has significantly increased seismic rates within continental interiors (Ellsworth, 2013). As a result, there has been increased public concern about the hazards linked to hydrocarbon extraction, which can lead to a cessation of operations (Ellsworth, 2013). Although most earthquakes caused by HF are unlikely to be felt (Rubinstein and Mahani, 2015), there are many observations of felt seismicity. One example is the M_w = 4.7 earthquake that occurred in the Sichuan basin, China, heavily damaging structures in the nearest villages (Lei et al., 2017). Another example is the M_L = 2.9 earthquake that occurred during operations at Preston New Road (PNR), Lancashire (Verdon and Kettlety, 2020). As a result, a moratorium banned any further hydraulic fracturing activities in the UK.

With the move towards net-zero technologies other geo-energy options are being actively explored, such as enhanced geothermal systems (EGS). However, the associated hazards can be significant. In Switzerland, a M_w = 3.2 earthquake resulted in significant insured damage costs at the Basel geothermal field (Edwards et al., 2015) and the 2013 M_w = 3.3 induced event in the St.Gallen geothermal reservoir led to a halting of operations (Carstens, 2019). Another example of an earthquake caused by EGS is the 2017 M_w = 5.5 earthquake in Pohang, Korea, which led to dozens of hospitalisations, one fatality and was the most damaging earthquake for centuries within the Korean peninsula. This earthquake is thought to be induced by a well which activated a previously unmapped fault (Ellsworth et al., 2019).

To understand the nature of these earthquakes, and mitigate the risks associated with them, seismology can be a useful tool. Current prospective approaches to mitigating hazards apply the 'traffic light scheme' which assigns M_w thresholds that indicate when operations should be halted. In the case that injection volume controls seismicity and maximum magnitudes (McGarr, 2014; van der Elst et al., 2016), as observed in some datasets (e.g., Kwiatek et al., 2019), the traffic light scheme could be a useful mitigation strategy. However, in many datasets there are unexpected jumps in magnitude (Verdon and Bommer, 2021). In 33 % of hydraulic fracturing induced seismicity (HF-IS) cases a M_w jump of more than one unit of magnitude is observed; in such cases more intricate statistical methods are more appropriate (Verdon and Bommer, 2021).

1.2 Basic rupture/earthquake mechanics

A Mohr-Coloumb frictional framework is usually used to describe how the stresses on faults respond to perturbances (such as fluid injections) in the subsurface. Earthquakes can occur because either a new fracture surface is created or an existing surface is reactivated due to reduction of effective stresses, in the case of pore fluid perturbations. If a fracture surface already exists, then a certain amount of effective normal stress reduction is needed such that the surface, which can be idealised as a plane, will slip when a certain amount of additional pore pressure is added according to:

$$P_c = \sigma_n - \frac{|\tau|}{\mu_{fric}}, \tag{1.1}$$

where τ is shear stress, σ_n is normal stress, μ is the coefficient of friction and P_c is pore pressure. For a given differential stress, the coefficient of friction controls what plane orientation will fail first.

If we model the crust as an elastic material, when failure occurs the stored potential energy (mostly in the form of elastic, gravitational and frictional) is transferred to creation of new fractures, work done on the fault (i.e., friction), plastic yielding and and radiated seismic waves (Kanamori and Rivera, 2006). A certain amount of shear stress is dropped, and the fault will begin building back stresses through tectonic strain or additional anthropogenic perturbation.

As seismic energy is an observable parameter, we can quantify it both theoretically and from far-field displacements. Energy portioning caused by faulting can be simply expressed using (Kanamori and Rivera, 2006)

$$E_T = E_R + E_{NR}, \tag{1.2}$$

where E_T is total energy, E_R is radiated energy and E_{NR} is non radiated energy. E_R refers to energy radiated as seismic waves and E_{NR} expresses energy linked to creation of new surfaces on the fault edge and dissipation of heat energy (i.e., friction).

Considering a simple shear fault, the radiated energy can be expressed by (Kanamori and Rivera, 2006)

$$E_R = \frac{1}{2}(\tau_1 - \tau_2)DA, \tag{1.3}$$

where τ_1 and τ_2 are the initial and final shear stresses on the fault plane, A is rupture area and D is the critical slip distance, often refereed to as D_c, as shown in Figure 1.1. This is a highly simplified way of expressing energy partitioning and in reality some energy will go into the creation of new fractures. A measure of the static stress drop can then be calculated using

$$\Delta\tau = \tau_1 - \tau_2. \tag{1.4}$$

The initial or final stresses are very difficult to measure, however, the average stress change on a fault can be measured from seismological data using (Kanamori and Anderson, 1975)

$$\Delta\sigma = \mu\bar{D}/L \tag{1.5}$$

where $\bar{D}$ is the average offset, L is the characteristic dimension (i.e., radius for a circular fault or width for a rectangular fault) and μ is rigidity. $\bar{D}/L$ is proportional to the strain drop and is dimensionless. When multiplied by the rigidity we obtain units of stress (i.e., Pa/m^2). $\bar{D}$ can be measured directly from low frequency seismic data using (Kanamori and Anderson, 1975)

$$\bar{D} = \frac{cM_o}{\mu L^2}. \tag{1.6}$$

where c is a geometric constant of order 1. A circular rupture is usually assumed for simplicity. Therefore the stress drop can be expressed as (Eshelby, 1957)

$$\Delta\sigma = \frac{7}{16}\frac{M_o}{R^3}, \tag{1.7}$$

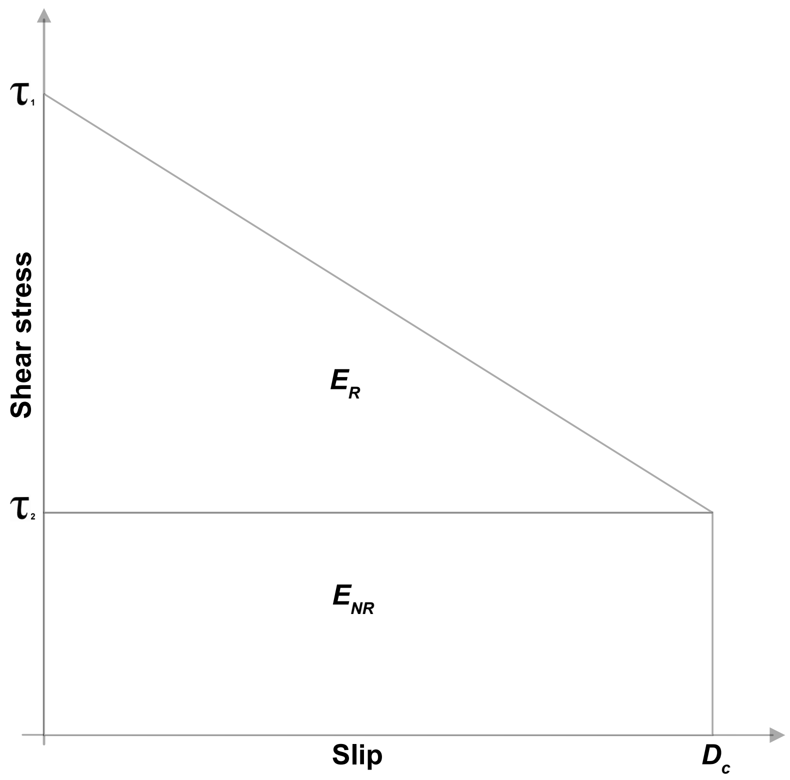

Figure 1.1: A schematic showing energy partitioning of radiated and non radiated energy on a unit area.

where R is rupture radius.

For large earthquakes where the rupture breaks the surface, the area of the fault is one of the unambiguous source parameters (Kanamori and Anderson, 1975). However, for smaller earthquakes which do not break the surface, the dimensions of the fault are more difficult to constrain and require inversion of rupture models. Radiated energy can be calculated directly from the energy flux in the far-field (Brune, 1970) using

$$u(f) = \frac{M_o}{[1 + (\frac{f}{f_c})^{\gamma n}]^{1/\gamma}}, \tag{1.8}$$

where *u(f)* is the far-field displacement spectrum, which can be obtained by directly fitting source models with an attenuation operator or using an empirical based approach to correct for path effects such as the spectral ratio method (Mueller, 1985). M_o denotes the seismic moment, f is frequency and f_c is corner frequency, γ and n are model dependent parameters that describe the spectral fall off. Many studies use n = 2 and γ = 1 (Anderson and Hough, 1984; Abercrombie, 1995; Prieto et al., 2004). A further modification by Boatwright (1980) gives a sharper corner frequency (n = 2 and γ=2) and is preferred in some cases (Ide et al., 2003; Holmgren et al., 2019). Corner frequency can then be used to calculate R using

$$R = \frac{\kappa\beta}{f_c}, \tag{1.9}$$

where f_c is the corner frequency of the Fourier displacement spectrum of a phase arrival, β is shear wave velocity and κ is a model constant which depends on the model used, for which there are a range (e.g., Brune, 1970; Madariaga, 1976; Kaneko and Shearer, 2014).

1.3 Stress drop observations and debates

Since stress drop was conceived of as a seismic parameter, it is sometimes included in earthquake catalogues which have an appropriate signal to noise ratio for calculations. The circular dislocation model proposed by Aki (1967) implicitly assumes (using a square decay in the high frequency) that slip scales with earthquake size, such that stress drop remains constant across magnitude. The scaling of rupture size with slip, so called self-similarity, was found to be consistent for observations of earthquakes from Parkfield, California, which supported the theoretical model proposed by Aki (1967). However, Aki (1967) acknowledged that scaling laws may differ between geological environments. Kanamori and Anderson (1975) then showed that for relatively large earthquakes (i.e., surface wave magnitude > 6) the ratio of the fault area with the slip distance follows a remarkably linear scaling of ~ 2/3 in log space between 1-10 MPa with relatively little scatter which supports the theoretical assumptions of a constant stress drop by Aki (1967).

Since then many other studies have found stress drop shows a stable average across many datasets, as reported in the global study by Allmann and Shearer (2009); observations from 2000 earthquakes show that stress drop varies between 0.4 to 50 MPa with a median value of 4 MPa, albeit with a large variability. For tiny earthquakes Kwiatek et al. (2019) report self-similarity down to M_w -4.1 but others find a breakdown in the scaling at lower magnitudes.

Initial observations of a breakdown in self-similar scaling for smaller earthquakes (e.g, Archuleta et al., 1982) have since been interpreted to be an artifact of compromising high frequency effects (Ide and Beroza, 2001; Deichmann, 2017), although some authors still interpret stress drop scaling with magnitude due to a physical mechanism. For example, Lin et al. (2016) observe a breach of self-similar scaling for smaller earthquakes which is interpreted due to slip patch heterogeneity (Lin and Lapusta, 2018) rather than the perfectly circular assumption made by Aki (1967).

Some authors have calculated lower stress drops from induced seismicity compared to tectonic seismicity (e.g, Abercrombie and Leary, 1993; Hua et al., 2013; Hough, 2014). The interpretation often given is that within an induced setting additional injection of pore fluids decreases the crustal strength and results in lower stress drops. However, many others find stress drops are comparable between induced and tectonic settings (Huang et al., 2016; Zhang et al., 2016; Huang et al., 2017; Ruhl et al., 2017; Kwiatek et al., 2019), but that closer to the injection point stress drops are lower (Ruhl et al., 2017).

The first observation of lower stress drops close to the injection point was made during the hot dry rock experiment developed at Fenton hill, New Mexico, which showed that seismicity rates appeared to increase from the point of injection and that stress drop also correlated positively with migration from the point of injection (Pearson, 1981). Others (Allmann et al., 2011; Kwiatek et al., 2014) have also reported increases in stress drop with respect to injection point. The interpretation is that under the assumption of linear fluid diffusion, crustal strength is lower closer to the injection point due to higher effective normal stress reduction. I will examine this mechanism in more detail in Chapters 2 and 4.

Others (e.g, Kwiatek et al., 2015; Sumy et al., 2017; Wu et al., 2018) do not observe a positive correlation between stress drop and distance from the injection point. In the case of earthquakes that occur during wastewater disposal in Oklahoma (Sumy et al., 2017), the lack of correlation suggests that the entire fault system experienced elevated pore pressures from previous injection. Thus the observation of stress drop may be sensitive to the geological setting and any previous injection that has occurred.

According to laboratory stick-slip experiments we expect that at larger confining pressures (i.e., larger depth), stress drop should increase (e.g, Byerlee, 1978). Some authors report increases of stress drop with depth (Hardebeck and Hauksson, 1997; Venkataraman and Kanamori, 2004). However, the depth dependent effects of attenuation appear to remove systematic variations of stress drop with depth (Abercrombie, 2021). Different faulting types could also cause larger stress drops in some datasets (Huang et al., 2017). Within induced seismicity datasets most authors do not report an increase in stress drop with depth (Kwiatek et al., 2015; Ruhl et al., 2017; Wu et al., 2018); such trends may not be revealed in induced seismicity datasets because of the relatively smaller depth range of seismic events compared to tectonic seismicity.

1.4 Signal retrieval challenges during HF-IS and effects on stress drop

During a hydraulic fracturing operation a borehole geophone array can be deployed to monitor the microseismicity that is caused by the stimulation of fractures (Figure 1.2a). Most of the seismicity occurs within the stimulated shales but the most hazardous seismicity is hosted on pre-existing fault structures where it may grow into larger earthquakes (Figure 1.2a). From source to receiver there are various perturbations to the emitted body waves that can change the spectral signal.

Along the path the body waves travel through fractures within the rocks, of which some have become expanded and filled with proppant to allow tight gas to flow (Figure 1.2a). For high frequency signals (i.e., >100 Hz) that are produced from microseismicity, the normal attenuating effect from friction (i.e., intrinsic attenuation) becomes exponentially larger. Butcher et al. (2020) exemplify the effect of disproportionately larger attenuation when observing the mismatch between estimated local and moment magnitudes. Such observations can be explained, theoretically, by the saturation of corner frequencies (Deichmann, 2017) because of preferentially higher attenuation. As a result R artificially remains the same in equation 1.7 and stress drop scales with magnitude. A schematic for the spectral signal produced by the effect of saturating corner frequencies is shown by the purple line in Figure 1.2b, where the signal suddenly drops off; this can cause an artificial increase in stress drop with respect to M_w.

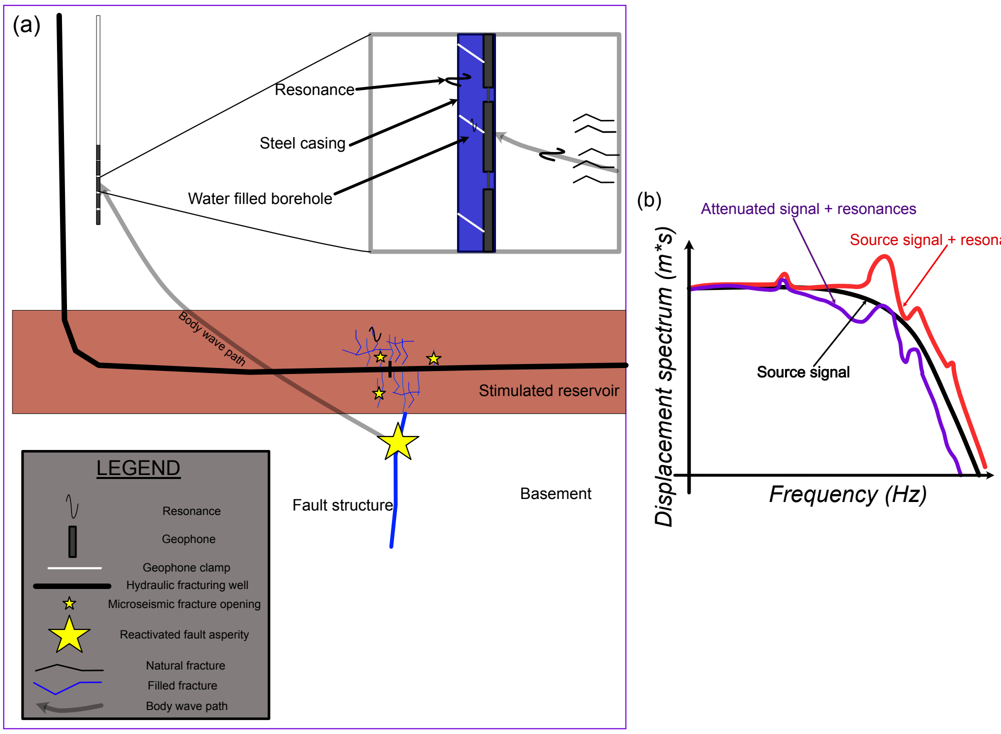

Figure 1.2: Schematic diagrams of (a) hydraulic fracturing operation and some of the key features a body wave passes through from source to receiver. (b) Schematic displacement spectra showing the unperturbed source signal (black line), resonance-perturbed signal (red line) and attenuated and resonance perturbed signal (purple line).

Another perturbance to the signal comes from resonances at various point along the path and near/at the receiver (Tary et al., 2014) which is illustrated in Figure 1.2a. Along the path, water filled fractures may resonate (Pettitt et al., 2009); closer to the geophone we expect resonances along the steel casing and in the wellbore (Sun and McMechan, 1988), the clamping system (Gaiser et al., 1988) and within the instrument itself (Faber and Maxwell, 1997). These resonances may cause bumps in the spectral signal (Figure 1.2b) which may affect corner frequency estimates (e.g., Holmgren et al., 2020). The effect of resonances on the spectral signal is exemplified by the red schematic line in Figure 1.2b. A systematic overestimate of corner frequencies will correspond to overestimates of stress drop.

1.5 Geological and operational setting of dataset

The dataset used in this thesis is collected during hydraulic fracturing operations. Hydraulic fracturing exploits gas which is trapped in tight shales and cannot be obtained through conventional hydrocarbon acquisition. By injecting high pressure fluids into the shale reservoir at perforations along a horizontal well, fractures are formed, which volumetrically opens up the rock and allows the gas to flow along a pressure gradient to the well. To optimise the volume amount a fracture opens, operators typically use a zipper frac technique whereby fractures are stimulated by alternating between two wells from the well toe to the well heel (Figure 1.4).

In this study we analyse seismic events linked to stimulation of a shale reservoir in the The Horn River basin (British Columbia) within the Western Canadian Sedimentary basin (Figure 1.3), and is one of the largest unconventional plays in North America (Yoon et al., 2018). Within the Horn River formation (Yoon et al., 2018) there are three over pressured shale units of Devonian age: Muskwa, Evie and Otter Park (Barker, 2014). These formations are characterised by fine grained, siliceous sediments which indicate a deep water setting during deposition (Yoon et al., 2018) during a period of multiple sea level changes and continental subsidence (Wilson, 2019). The Muskwa shale is overlain by the Fort Simpson shale unit and underlain by dolomites of the Keg River formation (Wilson, 2019). Hydrocarbon generation likely started in the Early Jurassic period and a subsequent change of tectonics from transpressional to transtensional during the Eocene resulted in uplift and erosion of the thermally mature Muskwa, Evie and Otter Park units (Wilson, 2019).

HF activities have occurred in the Horn River Basin since 2005 and as of December 2013, 291 horizontal and 78 vertical wells have been drilled for exploiting the shale-trapped gas (Barker, 2014). In this thesis we use a catalogue of microseismic events collected during operations between July-August 2013. A zipper frac technique was used to stimulate perforations and open fractures in the Muskwa, Otter Park and Evie formations along 10 wells. Along each well, 10 stages of perforations are completed for stimulation from toe-heel, apart from Well G which has 20 perforations (Figure 1.4). During operations 90,000+ microseismic events were recorded by the contractor between $-3 < M_w < 0.5$ (Figure 1.4) and the largest seismicity is hosted in the underlying limestone basement. The clearest fault structure is linked to injection along well A, where at stage 14, seismicity illuminates a fault structure that strikes roughly NE-SW (Figure 1.4).

The seismic events were recorded using three borehole geophone arrays (K, S and M-wells) positioned between ~1200-1700 m. Compared to broadband seismometers geophones enable a significantly higher frequency resolution necessary for analysing microseismicity. However, geophones are prone to high frequency resonances and have a poorer low frequency resolution. Each borehole consists of a vertical string of 35 geophones with a sampling frequency of 4000 Hz and a natural frequency of 15 Hz. For the studied events, we only have recordings from the K- and S-wells. For the purpose of calculating stress drops in Chapters 2 and 3 we also limit analysis to the P-phase only because of compromising features in the spectra.

Most of the seismic events contained within the dataset are at or below the noise floor (i.e., the amplitude of the noise) and are therefore not suitable for source parameter analysis. An example of a relatively large event (contractor M_w = 0.4) is shown in Figure 1.5. Firstly, any events below M_w = - 1 are likely to have a signal to noise ratio that is unsuitable for determining

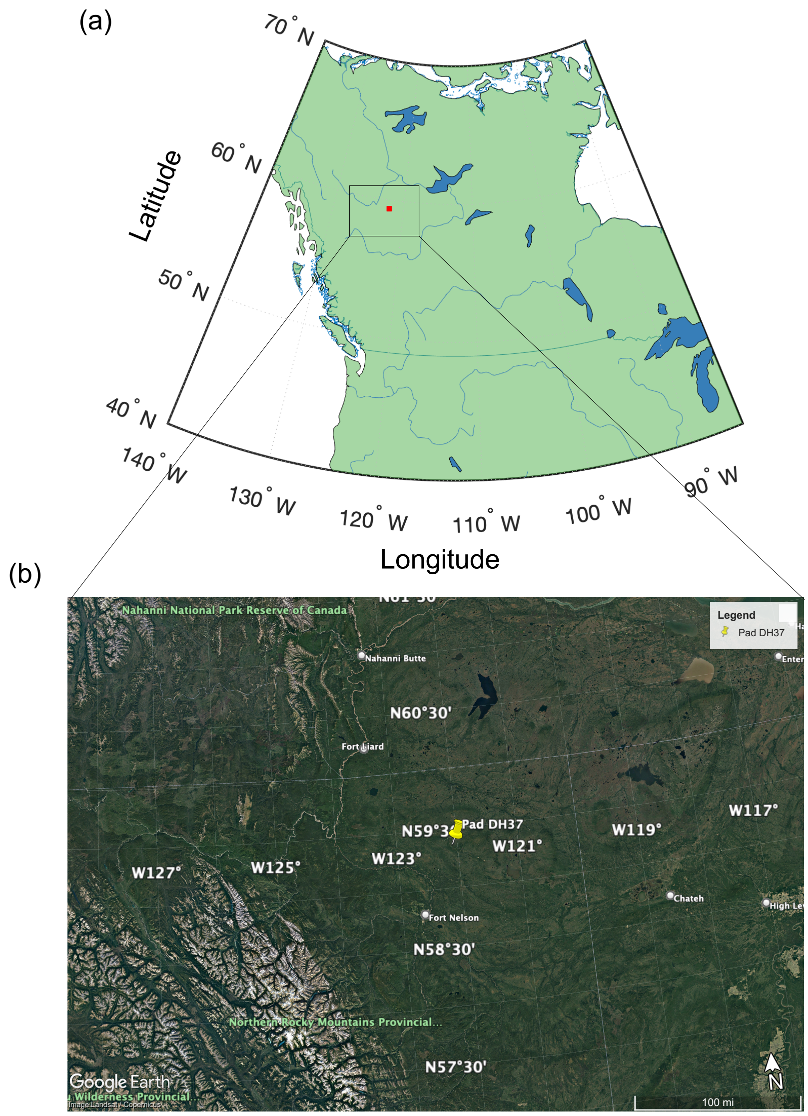

Figure 1.3: (a) Map of North America with the studied hydraulic fracturing pad denoted as a red square. (b) Zoomed image showing terrain around the pad, nearby towns, rivers and the pad location.

stress drops (Figure 1.5b). Above M_w = -1, seismic events may be considered for further analysis, which limits our analysis to 3599 events. Further limitations based on signal to noise ratio, high frequency cut-offs and quality phase arrival picks further limit our analysis to a more refined subcatalogue in Chapters 2 and 3.

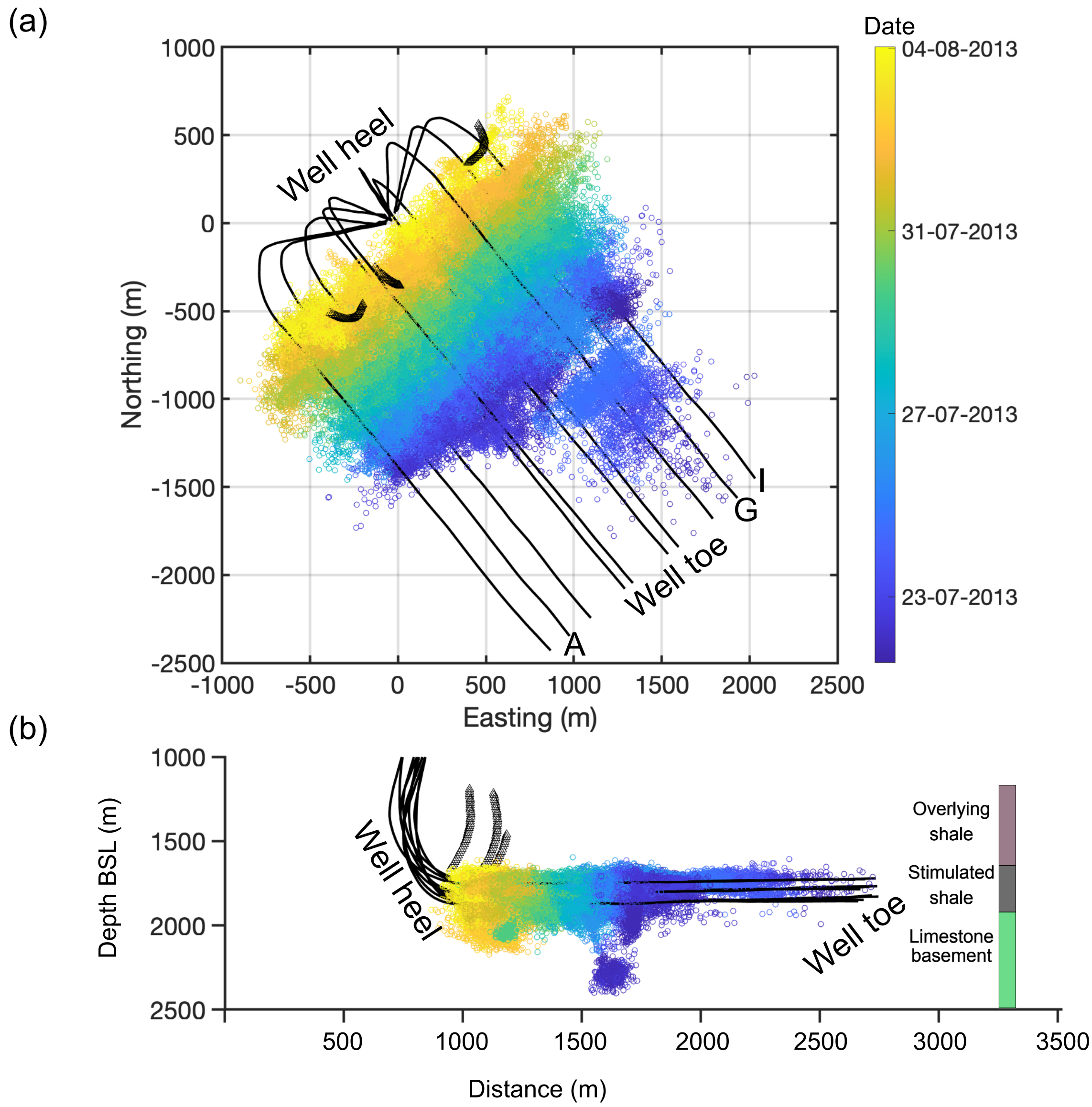

Figure 1.4: The seismic catalogue from hydraulic fracturing activities at a pad in the Horn River basin (Baird et al., 2017). Seismic events are denoted by circles, coloured according to date recorded. Black lines are wells, as labelled in (a). Triangles denote geophone arrays used for recording seismicity.

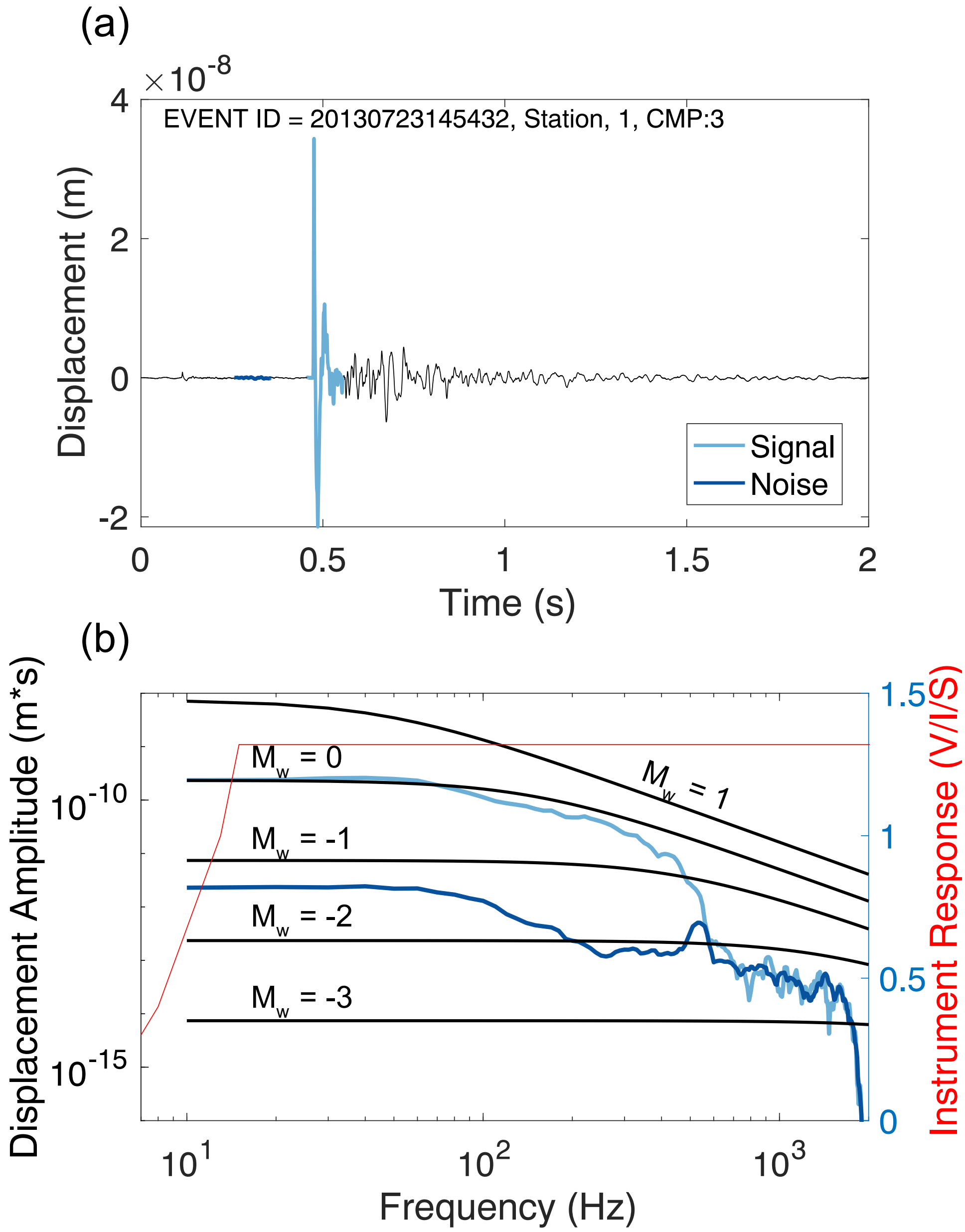

Figure 1.5: Example of a seismogram and the corresponding spectrum displaying the noise floor with respect to idealised spectra. (a) Time series of a seismic event in the basement rock. Light blue denotes signal and dark blue shows noise. (b) Multi-taper transform of signal and noise coloured as in (a) with black lines showing idealised synthetic spectra as labelled. right y-axis shows the instrument response in Volts per Inch per second.

1.6 Fault reactivation and stress drop applications

The primary seismic hazard from HF-IS operations is reactivating an existing fault structure in the subsurface. For some datasets the structures may extend above the stimulated formation (e.g, Eaton et al., 2018) or below in the underlying basement rock (e.g, Kettlety et al., 2019). Failure can be described using the Mohr-Coloumb failure envelope:

$$\tau > \mu_{fric}(\sigma_n - P), \tag{1.10}$$

where τ is shear stress, μ_{fric} is the coefficient of friction which is typically between 0.6-0.9 (Byerlee, 1978), P is pore pressure, σ_n are normal stresses and C is the cohesion. As additional pore pressure is added, the fault plane moves closer to the Mohr-Coloumb failure envelope (Figure 1.6).

There are a variety of ways that shear and normal stresses on a fault structure may change, potentially bringing a fault closer to failure. One mechanism for stress change is through elasto-static stress transfer from one asperity to another, assuming the strain field is changed through slip (e.g, Stein, 1999; Catalli et al., 2013) or from the opening of hydraulic fractures (Kettlety et al., 2020). Direct hydraulic connections to a fault can change the effective normal stresses and bring a fault to failure (e.g, Kettlety et al., 2019). In other cases poro-elastic effects are observed to be the primary cause of failure (e.g, Deng et al., 2016), which also changes shear and normal stresses. Aseismic deformation can cause slow failure and release elastic strain energy without necessarily causing seismic slip (e.g, Guglielmi et al., 2015; Eyre et al., 2020). Lastly, dynamic stress changes may also alter the stress state on a fault and possibly bring it to failure (e.g, Kilb et al., 2000).

For HF operations at the pad of interest, Kettlety et al. (2019) evaluate the possible failure mechanisms on major fault structures. Elasto-static stress transfer is unlikely to be the primary cause of failure because the imparted stress changes do not show a clear signal of driving fault structures towards failure (Kettlety et al., 2019). The maximum magnitude of expected stress changes (i.e., ± 1 MPa) are also significantly lower than the shear strength on faults to induce failure (Kettlety et al., 2019). Therefore it is more likely that a direct hydraulic connection causes fault instability, which significantly reduces effective normal stresses (Kettlety et al., 2019).

The stress changes on a stable structure in the Horn River basin can be illustrated on a schematic Mohr circle diagram (Figure 1.6). The circle describes the range of possible shear and normal stresses that can act on a 2D plane rotated through 360°. If the plane is perpendicular to the maximum principle stress the stresses on the plane can be represented by point 1 on the Mohr circle (Figure 1.6); if the plane is perpendicular to the smallest principle normal stress (σ_3) there will be no shear stress because shear stresses are parallel to the plane (point 2 on Figure

1.6) and the normal stress is σ_3. All the possible stress states between these two scenarios are described by the circle.

The relatively small normal and shear stress changes we might expect from elasto-static stress transfer is illustrated by the red circle (Figure 1.6), compared to the significantly larger effective normal stress reduction because of hydraulic fluid addition (blue circles). Once the failure criterion is met there is a stress drop of $\Delta\tau_1$ and the differential stress decreases. From laboratory experiments it is shown that at larger confining pressures there is a larger decrease in differential stresses during brittle failure (Byerlee, 1968; Cieślik, 2015), and therefore a larger decrease in the stress drop ($\Delta\tau_{1-3}$) (Figure 1.6) according to Mohr Coloumb frictional failure as effective normal stresses are reduced. Thus, we expect that the rock mass nearer the point of injection should have a lower differential stress compared to the rock volume further away; this would correspond to a lower average stress drop signal close to the point of injection relative to farther away, which some authors have observed (Pearson, 1981; Allmann et al., 2011; Kwiatek et al., 2014). However, others observe no such trends (Kwiatek et al., 2015), which questions the ubiquity of linear pore fluid diffusion used to explain observations of a growing stress drop.

Stress drop trends and failure mechanisms are likely sensitive to the type of induced seismicity. Enhanced geothermal systems purposefully exploit fracture networks in the subsurface to allow the flow of heated water, which most likely induces failure. Most of the observations of a growing stress drop are reported in EGS datasets (Pearson, 1981; Allmann et al., 2011). Wastewater injection typically involves injection into high-permeability rocks (Rubinstein and Mahani, 2015), with multiple rounds of injection which can decrease the strength of faults over some distance and lead to small perturbations in shear stress needed to induce seismicity (Sumy et al., 2017). For HF activities, low permeability shales are targeted, which are not as obvious conduits for fluid flow as the high porosity rocks in waster water injection or enhanced geothermal systems. However, existing fault structures may favour fluid induced mechanisms of failure (Kettlety et al., 2019).

1.7 Scientific questions and thesis outline

Stress drop continues to be an important parameter which is sometimes included within earthquake catalogues. Although many studies have calculated stress drops and tested the spatio-temporal patterns of stress drop from different datasets, key questions about our understanding of earthquake scaling, stress drop variations and the connection between stress drops and geomechanics remain unclear. The presented dataset will contribute to better understanding the role of stress drop in the context of HF-IS. The scientific questions we address are:

1. How robustly can we calculate high frequency source parameters from microseismic signals recorded along geophone arrays during hydraulic fracturing activities?

2. Do tiny earthquakes obey the expected scaling of earthquake slip with rupture size?

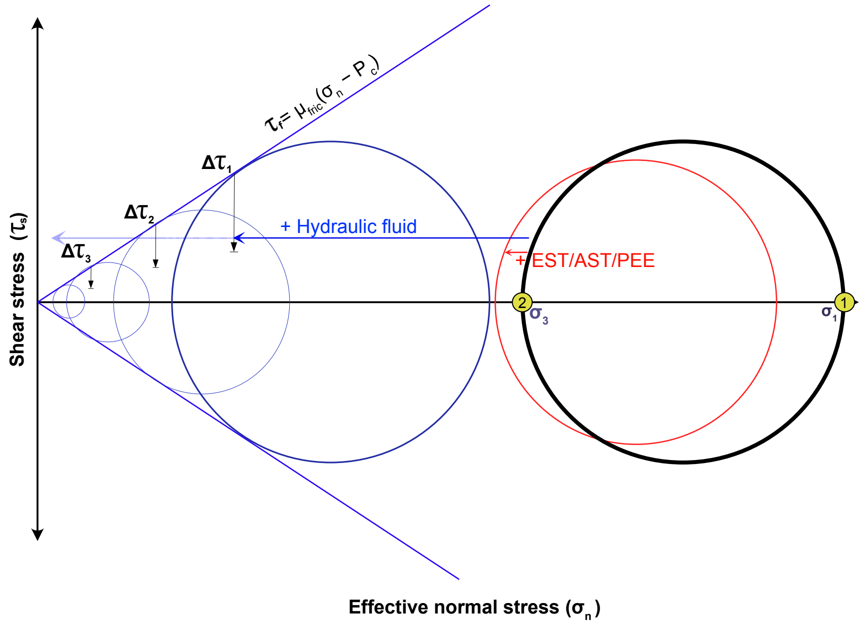

Figure 1.6: A Mohr-Coloumb schematic illustrating how stress states on a 2D plane could develop on a stable fault because of elastostatic stress transfer (EST), aseismic stress transfer (AST), poro-elastic effects (PEE) or addition of hydraulic fluid. The unperturbed stresses are denoted by a thick black circle with principle stresses labelled σ_1 and σ_3. Yellow points labelled 1 and 2 represent the planes where no shear stress is imparted. The red circle describes the stress state after elasto-static stress changes and the red arrow shows effective normal stress reduction. The blue arrow and blue circles show stress states after hydraulic fluid is added, which reaches the failure criterion (τ_f) and results in a stress drop ($\Delta\tau_1$). As hydraulic fluid is further added (light blue arrow) subsequent stress drops ($\Delta\tau_{2-3}$) are shown by vertical arrows.

3. What do spatio-temporal variations in stress drop reveal about the mechanism for reactivating fault planes?

4. How robustly can we estimate stability of major fault structures?

Questions 1-3 are addressed in Chapters 2 and 3. In Chapter 2 we start by showing observations of high frequency resonance features and high frequency limits imposed by the nature of microseismicity recorded along borehole geophone arrays. Then we provide an estimate of the crustal attenuation and calculate stress drop estimates using a model-fitting procedure. In Chapter 3 we use a more sophisticated approach (i.e., spectral ratio method) of removing the effect of attenuation and estimating stress drop estimates. Then we analyse variations within highly similar and co-located events. Question 4 is addressed in Chapter 4 where we delve into the geomechanics of the clear fault structure which reactivates.

CHAPTER 2

HIGH FREQUENCY CHALLENGES OF CALCULATING STRESS DROPS ALONG GEOPHONE ARRAYS

The contents of the following chapter has been published as *Stress drops of hydraulic fracturing induced microseismicity in the Horn River basin: challenges at high frequencies recorded by borehole geophones* by Adam G. Klinger and Maximilian J. Werner in Geophysical Journal International, Volume 228, Issue 3, March 2022, Pages 2018–2037. I conducted all analysis and wrote the manuscript for this paper, with edits by Maximilian Werner. All figures were produced by myself. Alan Baird, Tom Kettlety and James Verdon all provided background information of this dataset in this work.

I began this thesis by qualitatively analysing the noise characteristics of geophone arrays and the compromised signals which are then used to calculate stress drops. The microseismic dataset is used in all chapters of this thesis and the high frequency features reported in Chapter 1 are a common theme in Chapter 4 as well.

The ground motions caused by seismicity associated with fluid injection can pose a significant hazard. Borehole geophone arrays can provide access to tiny seismic events, which can extend the investigated magnitude range. However, the high frequency phase arrivals (i.e., > 100 Hz) also present challenges associated with high frequency cut-offs (f_{max}), stronger attenuation and resonances within geophones. These effects limit our ability to accurately constrain attenuation models and high frequency source parameters. We investigate 112 -0.6 ≤ M_w ≤ 0.7 seismic events and calculate corner frequencies and stress drops from 90 of these events recorded during hydraulic fracturing treatment in the Horn River basin, British Columbia. High frequency resonances (> 250 Hz) caused by spurious frequency excitation and/or coupling issues can significantly distort the shape of phase arrival spectra and affect source parameter estimates.

Critically, resonances vary in strength between (nearly) co-located events, which may compromise the validity of a spectral ratio approach. For stations showing the cleanest spectra, the Brune model provides a decent fit to the displacement spectra. However, bandwidth limitations, low signal to noise ratios, high frequency cut-offs and significant attenuation still hinder our ability to retrieve high frequency source parameters. We find that a frequency independent Q_p = 180 ± 40 provides a reasonable model for crustal attenuation but the large uncertainty caused by resonances prevents a robust constraint. From those events that show the best fits, we find a mean Madariaga corner frequency of 210 Hz ± 30 from P-phase arrivals, which is in the range of expected values if self-similarity extends into negative magnitudes. We also calculate a mean stress drop of 1.6 MPa ± 1.2, which is within the tectonic range but slightly lower than other deeper regional studies, which can be explained by lower effective stresses and/or a lower crustal shear strength. We find no evidence for a change in stress drop with depth or distance from the point of injection. A plausible explanation is that effective stresses are lowered relatively quickly over the entire fault zone via direct hydraulic connections. However, the large uncertainties make it difficult to interpret source parameter variability in detail. For high resolution monitoring and source properties of microseismicity, there is an urgent need for high quality high frequency recordings unaffected by spurious frequencies.

2.1 Introduction

In recent years, subsurface industrial activity has increased in both renewable and non-renewable energy sectors. Hydraulic fracturing, (e.g., Clarke et al., 2014), enhancement of geothermal systems (e.g., Deichmann and Giardini, 2009; Holmgren and Werner, 2021), carbon capture and storage (e.g., Verdon et al., 2013) and waste water injection (e.g., Keranen et al., 2014) have demonstrated the ability to cause felt seismicity. This study focuses on seismicity induced by hydraulic fracturing, which in most cases is not felt (Rubinstein and Mahani, 2015), but via the re-activation of pre-existing faults can induce damaging earthquakes (e.g., Lei et al., 2017; Tan et al., 2020). To mitigate the seismic risk linked to fluid injection, we need to better understand the physical mechanisms causing induced seismicity and how the mechanisms vary between data sets. Some authors suggest direct hydraulic pressure dominates as the main mechanism, whilst others posit diffusion of pore-pressure fluids (e.g., Goebel et al., 2017; Goebel and Brodsky, 2018), aseismic slip (Eyre et al., 2019) or stress transfer due to the opening of hydraulic fractures (Kettlety et al., 2020).

The spatio-temporal analysis of microseismic event locations is fundamental to understanding how fracture networks develop. To understand how the rupture physics are related to the injection of fluids, however, source properties (e.g., moment tensors, moment magnitude and stress drop) are needed. Stress drop is a particularly insightful metric because it is a function of two physical attributes: seismic moment (M_o) and corner frequency (f_c). Seismic moment is related to the rupture size and slip; corner frequency is the curvature change point on a displacement spectrum that can be interpreted, using the model of Madariaga (1976), as related to rise time and finite propagation length (Aki and Richards, 2002). In enhanced geothermal systems, some studies have found that the stress drop can be used as a proxy for the pore-fluid pressure (Pearson, 1981; Allmann et al., 2011; Lengliné et al., 2014). These studies suggest stress drops decrease nearer to the point of injection as a result of a lower effective stress.

Stress drops can be used to better understand the scaling of high frequencies for different M_w's, which is also important when developing ground motion prediction equations. Many tectonic studies support the geometrical similarity of tectonic earthquakes implicit in the canonical model for far-field radiation (e.g., Abercrombie, 1995; Hiramatsu et al., 2002; Ide et al., 2003; Allmann and Shearer, 2009). However, it is still debated as to whether self-similarity is also applicable to microseismicity (Ide et al., 2004; Venkataranman et al., 2006; Lin et al., 2016).

Source parameters from microseismicity are particularly difficult to accurately determine because of unaccounted attenuation under the assumption of frequency-independent anelastic attenuation and bandwidth limitations. Unaccounted attenuation has also been observed in the form of a high frequency cut-off (Hanks, 1982), often termed f_{max}, which led to the introduction of κ, a term which expresses an additional filter to high frequencies. κ can be expressed as a contribution of a path (κ_p) and site term (κ_o) (Ktenidou et al., 2014). f_{max} is interpreted to be a κ_o effect due to fractures in the shallow crust. However, the physical meaning behind κ_o remains to be established. Most studies attribute κ_o to a shallow crustal site effect (Ktenidou et al., 2014) but it might also manifest in borehole environments (Ide et al., 2003). Others have used a frequency dependent Q and argued that it is particularly needed for source parameter estimation along boreholes (Ide et al., 2003). Bandwidth limitations can also cause spurious scaling of apparent stress with magnitude, as shown by Ide and Beroza (2001), due to an underestimation of radiated energy.

Stress drops also allow us to better understand how the underlying physics may differ between deeper, tectonic settings and shallower induced settings. Some studies suggest similar stress drops in induced and tectonic environments (e.g., Tomic et al., 2009; Yenier and Atkinson, 2015; Huang et al., 2016; Zhang et al., 2016; Abercrombie, 2015; Ruhl et al., 2017; Holmgren et al., 2019) whereas others find differences (e.g., Hua et al., 2013; Lengliné et al., 2014; Hough, 2014). It may also be important to account for the faulting style and depth of the events when interpreting the differences in stress drop between tectonic and induced datasets (Huang et al., 2017).

In recent years, the Empirical Green's function (EGF) method and spectral decomposition method (Trugman and Shearer, 2017) have been used widely to determine stress drop (Shearer et al., 2019). Both methods attempt to remove path and receiver effects using deconvolution from a far-field signal, which presumes a form of linearity of these effects. The EGF method, in particular, can show biased estimates of the target event corner frequency based on the smaller event corner frequency (Abercrombie, 2015; Shearer et al., 2019). EGFs must be smaller than the targets, therefore finding suitable EGFs for microseismic events is limited by the poorer signal to noise ratio from already very small events. As such, it can be difficult to generate a comprehensive catalogue of stress drop values using the spectral ratio approach in a microseismic dataset. Practically, picking an EGF requires more time compared to directly fitting a source model, which can be done in real time. For these reasons, there is still a need to understand the far-field spectra and identify features that could compromise more sophisticated approaches, such as the high frequency resonances documented here.

For source parameter estimation, it is useful to have seismic data from both surface and borehole data. Downhole data show arrivals with a higher SNR (signal to noise ratio), reduced surface attenuation effects and vast catalogues of microseismic events. However, downhole geophones can record resonances that are less likely to occur at surface seismometers. At the receiver these are: low frequency plane waves propagating through the fluid in a wellbore (Sun and McMechan, 1988); high frequency dispersive waves propagating along the pipe-interface, also known as Stoneley waves (Haldorsen et al., 2006); reverberations in the casing and coupling issues (Gaiser et al., 1988). At the event source side, resonances can be caused by fluid-filled cracks (Aki et al., 1977) and small undetected events (e.g., Pettitt et al., 2009). Along the path, waves can be trapped within reflecting layers (waveguides) especially when there are alternating layers of sandstone and shales (e.g., Van Der Baan, 2009). In addition to all these effects, downhole geophones can show spurious resonances caused by the movement of the geophone system orthogonal to the normal working axis (Faber and Maxwell, 1997).

The objective of this study is to calculate stress drops from microseismicity at one of the plays within the Horn River basin, one of the largest unconventional reservoirs for gas-trapped shales in North America (Yoon et al., 2018). Previous studies have used this dataset to conduct statistical modelling (Verdon and Budge, 2018), elasto-static stress transfer modelling (Kettlety et al., 2019), and to study shear wave splitting (Baird et al., 2017). Here, we first show examples of amplifications in the pre-event noise and phase arrivals from a sub-catalogue of 112 events which are selected according to quality criteria from a vast dataset of 90,000+ events. These high frequency amplifications are most likely caused by coupling issues and the excitation of spurious resonances in the instruments. Secondly, we calculate M_w estimates and determine a crustal attenuation model. Thirdly, we test the depth and distance dependence of stress drop (limited to P-phase arrivals only) from a single injection point (e.g., Allmann et al., 2011) by focusing on 90 of the 112 events linked to injection at stage A14, where microseismicity illuminates a fault zone (Verdon and Budge, 2018; Kettlety et al., 2019). For these 90 events, we estimate corner frequency and stress drop. Our results add further evidence that self-similarity extends down to negative magnitudes and that the absolute stress drop values are within the tectonic range. We also find no correlation between stress drop and depth or distance from the point of injection. Unfortunately, corner frequency and stress drop estimates have a large uncertainty, which makes it difficult to infer statistically significant physical correlations.

2.2 Data

We use data acquired by a contractor during hydraulic-fracturing operations in the Horn River basin, British Columbia. There are three stratigraphic units that were targeted during operations: The Muskwa, Otter Park and Evie formations. These are all fine-grained, organic rich shales that likely formed in an open marine environment (Yoon et al., 2018).

The contractor used a multi-well, multi-stage approach to stimulate fractures in the shale formation in the Horn River basin. 10 wells were drilled and 237 stages were completed using a toe-heel zipper frack technique. During operations, the contractor recorded continuous seismic data and provided us with continuous SEG-D tapes recorded using 15 Hz GEO-OMNI-2400 borehole geophones at 2 arrays (K and S), each with 35 stations, as shown in Figure 2.1. The instrument response, as determined from the lab, shows the amplitude of the output increases up to the natural frequency (15 Hz), after which the instrument dampening enables a flat response up to at least 500 Hz with an output of 1.1 volts per inch per second. Instrument specifications also mention that spurious frequencies are expected at frequencies greater than 365 Hz. The instrument samples at 4000 Hz. The contractor also provided us with original station orientations determined from perforation shots. The Z component is mostly aligned in the direction of the well at both the K- and S-well, whilst the first and second components are sub-horizontal.

The K-well geophones were deployed at 1215 - 1695 m and the S-well geophones between 1193 -1663 m with 13-15 m spacing between geophones. Phase arrivals have larger amplitude at the shallower stations, which might be related to a crustal amplification effect (Figure 2.2). We were also provided with a catalogue of more than 90,000 moment magnitudes (-3 < M_w < 0.55), stress drops, fault radii and locations for all events and full moment tensor inversions for 35% of events. The methods used for determining source parameters were not available, nor their uncertainties. For this reason, we recalculate corner frequencies and stress drops. We also recalculate M_w estimates in section 2.4.2. From here on magnitudes provided by the contractor are denoted by $M_{w,c}$ and estimates from this study are denoted as M_w.

Previous research shows that the stimulation of stage 14 in well A (stage A14) resulted in microseismicity that extended into the basement rock, indicating fault reactivation (Kettlety et al., 2019). The microseismicity is usually largest underneath the play, and therefore of particular interest from a seismic hazard perspective. We can also test the hypotheses relating stress drop to depth or distance form an injection point by limiting stress drop analysis to events linked to stage A14 (Figure 2.1b), which we implement in section 2.5.5.

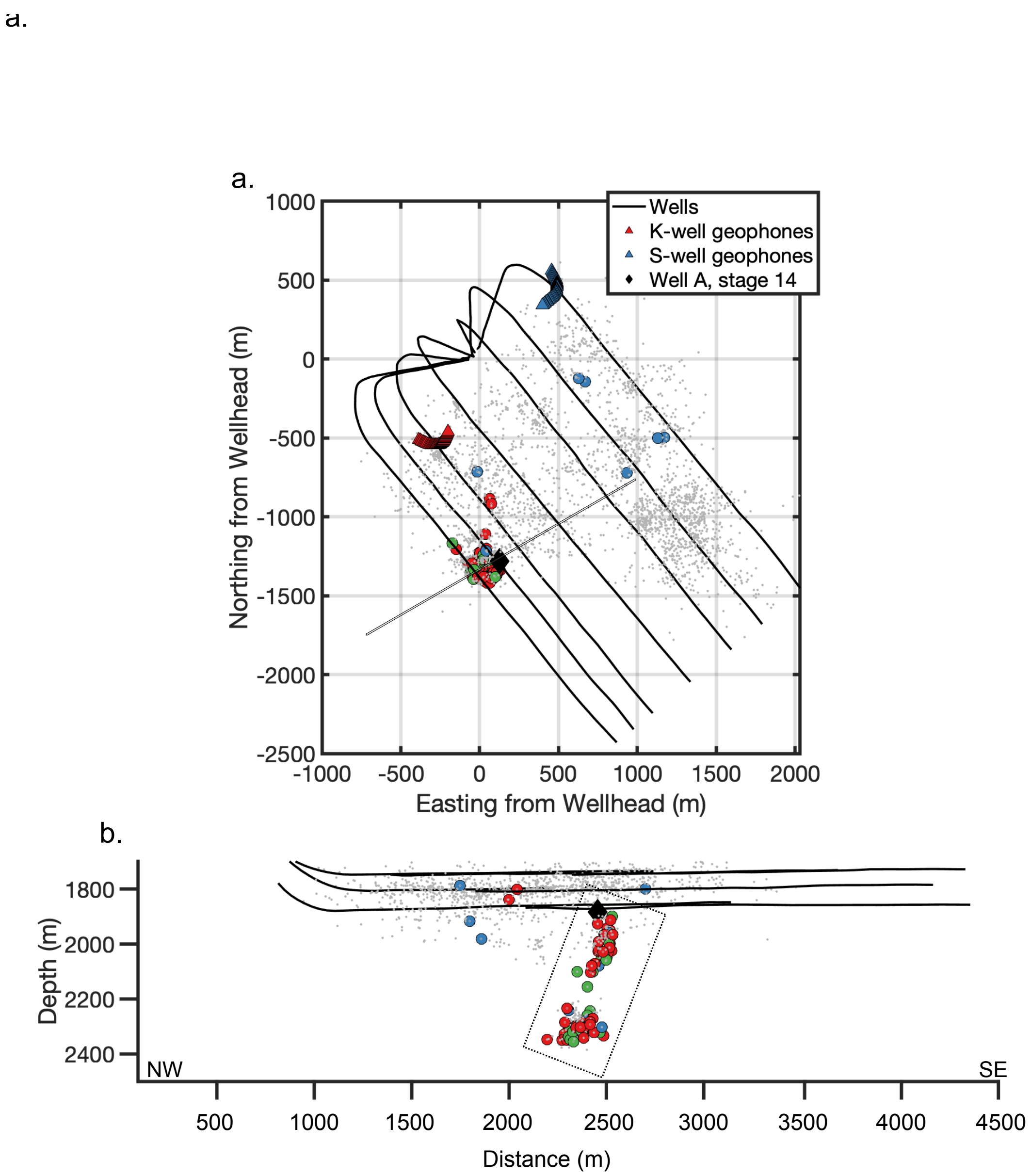

Figure 2.1: (a) Map and (b) Cross sectional view along the grey line in (a) illustrating the multi-well hydraulic fracturing operation, monitoring wells and locations of induced seismicity. The colored events correspond to those that meet processing criteria. Circles denote seismic events where green symbols are events recorded at both the K and S well (38 events), red circles are events only recorded at the K-well (56 events) and blue circles are only recorded at the S-well (18). Grey circles show $M_{w,c}$ > -1 events. (b) The dotted rectangle outlines seismicity (90 events) linked to stimulation at stage A14, denoted by a black diamond.

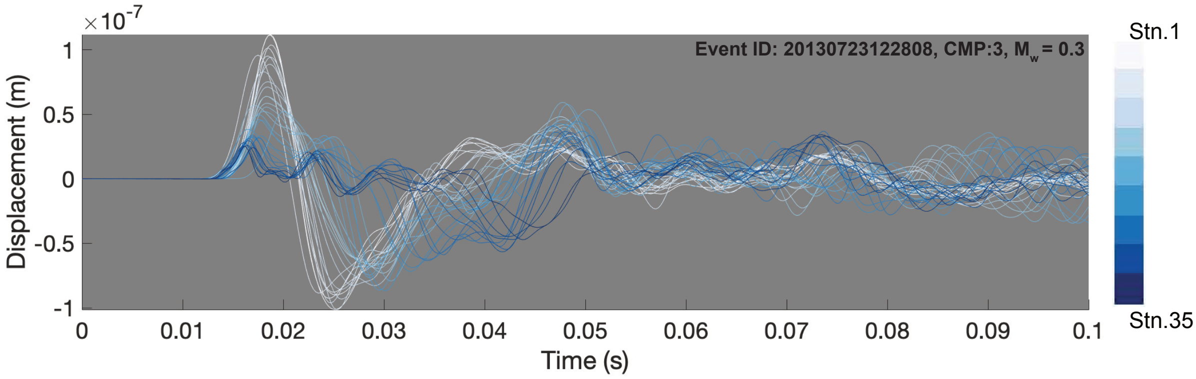

Figure 2.2: Displacement time series of a seismic event hosted along the re-activated structure for all stations at the K-well showing the P-phase arrival. Each line is coloured according to the station, where darker blue indicates a deeper station.

2.2.1 Velocity model and locations

The contractor provided us with the event locations and a velocity model (Figure 2.3). The seismic event locations were improved by the contractor using double difference relocation (Waldhauser and Ellsworth, 2000). Uncertainty is estimated at ± 50 m for relative locations and ± 100 m for absolute locations (Kettlety et al., 2019). Travel times were not provided by the contractor.

2.2.2 Travel times

To determine travel times we use a finite-difference approach to solve the eikonal equation (Podvin and Lecomte, 1991) using NonLinLoc (Lomax et al., 2009). In doing so, we calculate the fast travel times to each grid point over a 2D matrix to construct travel time lookup tables for the P- and S-phase arrivals. We then use the locations provided in the catalogue to calculate the geometric distance between source and receiver and interpolate the lookup table to calculate travel times for each station.

2.2.3 Data and Results availability

Although operator-provided data are not currently available publicly, we provide an open-access dataset of our results on Zenodo (Klinger and Werner, 2021). The spreadsheet contains event IDs, magnitudes, corner frequencies and stress drops as well as their uncertainties of the 94 events analysed in section 2.5.5. The data may be useful for testing the replicability of our conclusions with other datasets or to compare stress drops.

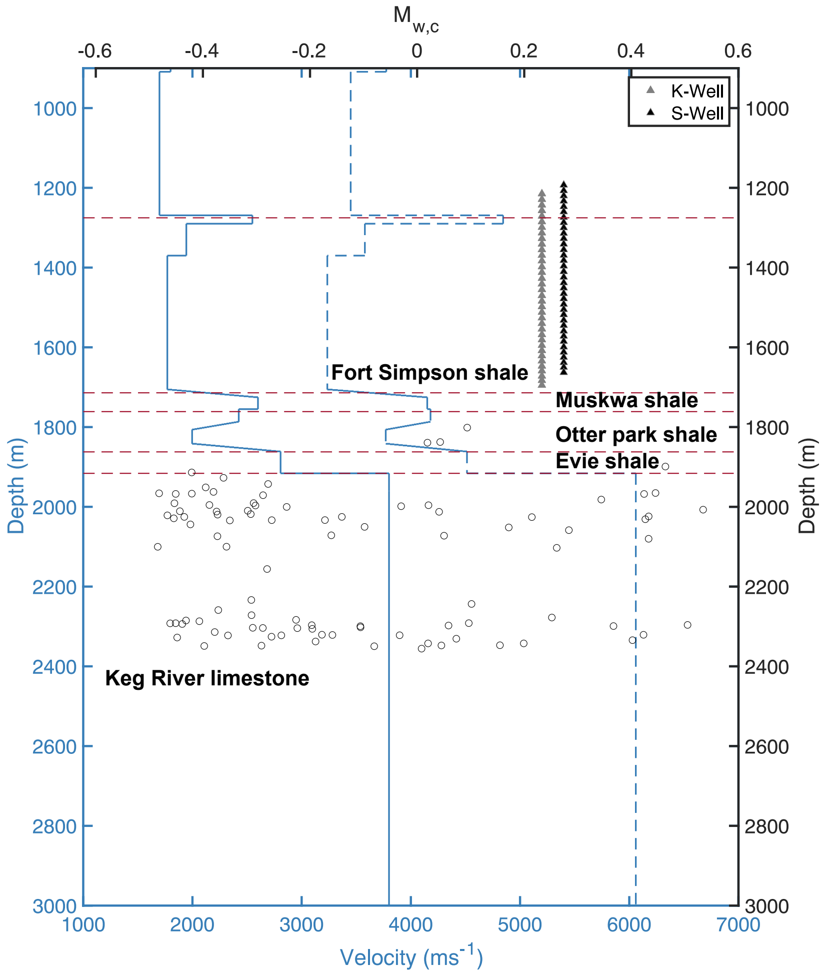

Figure 2.3: Tapered velocity model with geological formations. Black circles denote depths and moment magnitudes of events calculated by the contractor ($M_{w,c}$) that meet processing criteria. Grey and black triangles indicate geophones in the K- and S-well, respectively. Solid blue and dashed blue lines show S- and P-wave velocity profiles, respectively.

2.3 Processing

The contractor provided us with ~ 9 hours of raw SEG-D data from the period of operation separated into 20 minute files. Baird et al. (2017) then separated out the continuous data into event separated SAC files using times from the catalogue, and also rotated stations into NEZ orientation. Over 90,000 detected events were provided by the contractor, though individual phase picks for each station were not provided. We pick the data using an STA/LTA method

(Allen, 1978) and require accurate phase arrival picks across all stations - a condition only met by high SNR events. From visual inspection, we find that an STA/LTA = 15 is required for the P-phase and an STA/LTA = 30 for the S-phase. The higher threshold for the S-phase is due to the higher pre-phase arrival noise (the P-wave coda). To improve the pick accuracy we also apply a 4-pole, 2 pass Butterworth filter between 15 Hz (natural frequency) and 200 Hz.

As the instrument response is 1.1 volts per inch per second, we correct for this by: dividing the time-series by 1.1, unit converting from inches to metres, and integrating to displacement. We then find the polarization angle of the radial component for each event by calculating the co-variance matrix of the 3 components on the primary arrival using a 0.1 s time window that captures the full phase and some coda. We then rotate the vertical component to the vector which corresponds to the maximum eigenvalue. For the SH and SV components, the co-variance matrix is calculated from the second phase arrival. We then rotate the North and East components using the eigenvalue that maximises transverse particle motion.

2.3.1 Multi-taper transformation

We use the multi-taper method to transform from the displacement-time series to a displacement-frequency spectrum in line with many other source studies (e.g., Allmann and Shearer, 2009; Harrington et al., 2015; Wu and Chapman, 2017; Holmgren et al., 2019). The multi-taper method reduces the amount of sidelobe leakage from lower frequencies (Gubbins, 2005), which increases the accuracy of transformation compared to a standard Fourier transform. We use the following equation:

$$S(f) = \frac{1}{k}\sum_{k=1}^{k} |\sum_{t=0}^{n-1} x(t)a_k(t)e^{-2\pi i f t}|^2 \tag{2.1}$$

where *S(f)* is the average power spectral density function, $a_k(t)$ is a series of weights, *x(t)* is the signal, f is frequency, and t is time, n is the number of data points in a time-series. The user is required to assign the time-bandwidth product (TBW) and the number of tapers (k). The TBW is the averaging bandwidth for each spectral point estimation. k refers to the Slepian sequence of orthogonal, prolate tapers used to weight the time series (Prieto et al., 2007). It is still uncertain what the optimal choices for these parameters are. From visual inspection of the spectra we find that TBW = 4 and k = 7 generates spectra that are sufficiently smoothed but do not bias spectral amplitudes for the frequency range analysed.

From a displacement time series, the units of the power spectrum are in m^2/Hz. Therefore, to convert to displacement amplitude we use

$$A(f) = \sqrt{S(f) * T}, \tag{2.2}$$

where *A(f)* is the displacement amplitude spectrum and T is the time window used to capture the phase arrival. This leaves us with units of meter seconds.

2.3.2 Resolution

In this section, we consider the limitations that the instruments and data place on our ability to resolve corner frequencies. It is crucial to delineate the boundaries of the accessible frequency range as this affects the interpretation of results. This was exemplified by Ide and Beroza (2001), who showed that the underestimation of radiated energy in various studies can lead to erroneous interpretations.

To determine the range of resolvable corner frequencies, we first calculate theoretical seismic moment values using

$$M_o = 10^{\frac{3}{2}M_w + 9.1}, \tag{2.3}$$

from Hanks and Kanamori (1979), where M_o is seismic moment and M_w is moment magnitude. Using these seismic moment values, we then determine hypothetical measurements of corner frequency assuming constant stress drops for the purpose of this section only using Brune (1970):

$$\Delta\sigma = \frac{7}{16} M_o \Big(\frac{f_c}{\kappa\beta}\Big)^3, \tag{2.4}$$

where corner frequency is f_c, κ is a constant related to the model used and β is shear wave velocity. We assume κ = 0.32 (see section 2.4) and β = 3800 ms^{-1}.

For a range of hypothetical M_o values, we calculate the corresponding f_c for 4 different stress drops (Figure 2.4). We determine the lowest $M_{w,c}$ event for which a corner frequency can theoretically be recorded with a 1 MPa stress drop by plotting a vertical line, intersecting at $M_{w,c}$ = -2.7 (Figure 2.4). The lower frequency detection limit is plotted at 15 Hz (the natural frequency) and the upper limit at 2000 Hz (the Nyquist frequency).

To avoid introducing artefacts in empirical observations between stress drop and M_w we calculate the maximum source corner frequency which captures a sufficient fraction of radiated energy using (Ide and Beroza, 2001)

$$F(f, f_c) = \frac{(-f/f_c)}{(1 + \frac{f}{f_c})^2} + \tan^{-1}(f/f_c), \tag{2.5}$$

where F is the fraction of radiated energy captured, a function of the sampling frequency f and the source corner frequency f_c. We set an upper limit to f_c of 500 Hz, where at least 75 % of the radiated energy is captured. 500 Hz therefore represents the maximum source corner frequency that can be accurately determined. The bandwidth limitation has a more severe effect on estimates of apparent stress, based on radiated energy, but can also affect the maximum corner frequency.

We further investigate the resolution of corner frequencies by considering the acceleration spectra. Ideally, we would expect the shape of the acceleration spectrum to show one point of curvature change, corresponding to the f_c, followed by a plateau to higher frequencies. If such an idealised spectrum is attainable, it would yield the most robust fit to a Brune model.

Within this dataset only the P-phase arrivals at the K-well show a plateau (Figure 2.5), whereas most S-phases do not. Along both wells, we also observe a systematic cut-off of the high frequency acceleration spectrum, occurring at ~ 400-500 Hz along the K-well and ~ 200-300 Hz along the S-well. Such an abrupt cut-off might be explained by f_{max} (Hanks, 1982; Anderson, 1986). Because we are unable to observe a flat plateau for S-phase acceleration spectra, it is impossible to know if we are observing the first corner frequency (i.e. f_c) or a cut-off frequency. For this reason, we exclude the S-well from determining source parameters in section 2.5.5 and only use P-phase arrivals at the K-well.

We then impose 2 additional criteria based on observations during processing. We only use events that show accurate picks on the primary arrivals across all stations using the STA/LTA picking method. The lowest $M_{w,c}$ event that meets this requirement is a $M_{w,c}$ = -1.2 event (Figure 2.4). We also require that all signals should record a SNR > 3 at 500 Hz, to ensure enough of the high frequency is sampled. We find the lowest $M_{w,c}$ event that meets this requirement is a $M_{w,c}$ = -0.8 event (Figure 2.4). This leaves us with a -0.8 < $M_{w,c}$ < 0.55 range for our spectral analysis, for which we find a total of 112 events. 38 events are recorded at both wells, 56 at the K-well only and 18 events at the S-well only (Figure 2.1).

To summarise, the criterion we impose are:

1. M_w >-2.7: The magnitude limit which corresponds to the lowest source corner frequency the geophones can resolve (assuming a 1 MPa stress drop).

2. 500 Hz: Highest source corner frequency that provides enough energy to suppress empirical artefacts between stress drop and M_w (Ide and Beroza, 2001)

3. M_w > -1.2: The magnitude limit which corresponds to criterion 1-2 combined with the additional criterion that picks are correct across all stations and wells. Accurate picks of phase arrivals are needed to calculate stress drops.

4. M_w > -0.8: The lower magnitude limit from criterion 1-3 with the additional requirement that the SNR ≥ 3 at 500 Hz. Events that do not resolve signal clearly up to at least 500 Hz are unlikely to provide robust stress drop estimates.

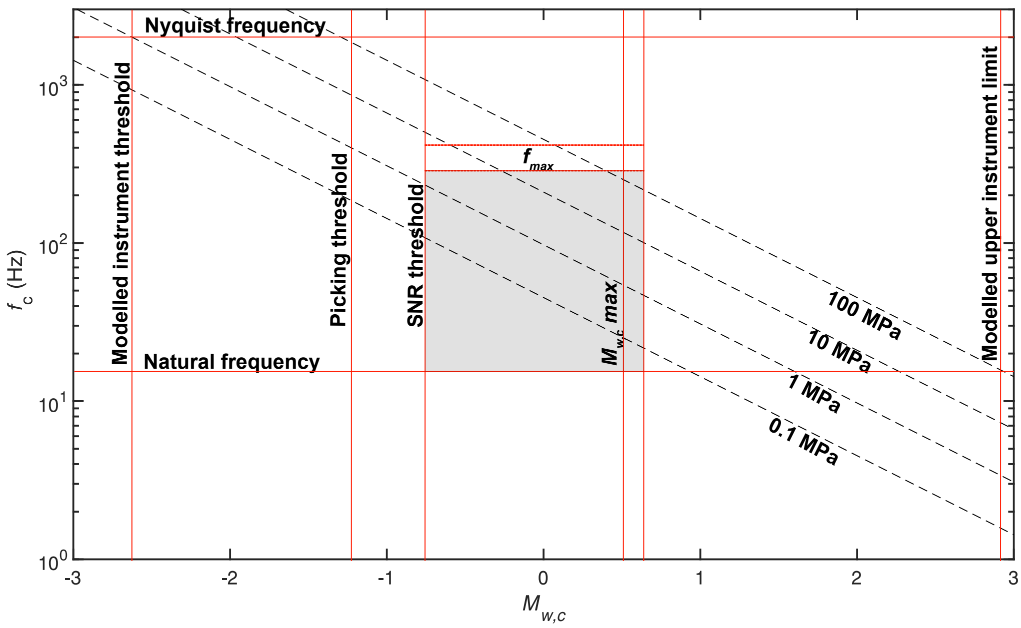

Figure 2.4: Theoretical f_c against $M_{w,c}$ with red lines showing the multiple constraints from data and instruments that limit the range of magnitudes and corner frequencies that are resolvable (grey rectangle). Dashed black lines show the scaling relationship between corner frequency and $M_{w,c}$, assuming a range of constant stress drops and self-similar scaling using a Madariaga (1976) model. To construct the stress drop lines, we assume β = 3800 ms^{-1}, from the S-wave velocity in the Keg-River formation, where most of our events are located.

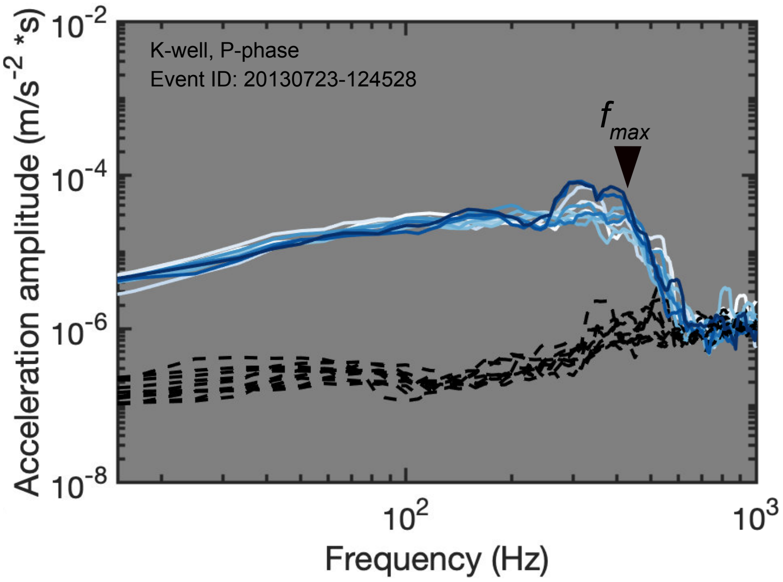

Figure 2.5: Acceleration spectra from the P-phase component of a M_w = 0.1 event recorded at the K-well. The solid lines are the observed signals using a 0.1 s time window, and are colour coded according to station depth: darker blue indicates a deeper station. The dashed black lines represent the spectra of pre-event noise.

2.4 Methods

2.4.1 Modelling individual spectra

Most studies that calculate source parameters through model fitting procedures use the Brune (1970) model. Madariaga (1976) expanded on this model by approximating a dynamic rupture where the fault plane is modelled as a circular crack. Using this analytical solution, we can determine source properties using (Brune, 1970):

$$u(f) = \frac{\Omega_o e^{\frac{-\pi f t}{Q}}}{[1 + (\frac{f}{f_c})^2]}, \tag{2.6}$$

where u is the far-field displacement spectrum, Ω_o denotes the amplitude of the low-frequency plateau, t is the travel time of the dominant phase arrival, f is frequency and f_c is corner frequency. There is also an attenuation term, Q, where $1/Q$ represents the loss of energy per cycle.

We must estimate 4 unknowns: Q, t, f_c and Ω_o. When determining source parameters in section 2.5.5, we fix Q and Ω_o to constants. We determine Ω_o from the low frequency amplitude and Q using the whole path attenuation, as explained in sections 2.4.3 and 2.5.4. Travel time t is also constrained, as explained in section 2.2. We then optimize the fit of equation (2.6) to single station displacement spectra using @fminsearchbnd (D'Errico, 2012) to obtain corner frequencies. @fminsearchbnd uses non-linear least squares optimisation of the cost function (y-axis difference between the modelled and actual far-field spectrum squared, in log 10 space) through a simplex algorithm (Lagarias et al., 1998).

To determine f_c uncertainty, we bootstrap the residuals between the model fit and observed data. We calculate the residuals at each frequency point in log space and then resample 30 times and add these residuals to the original spectrum to create 30 new synthetic spectra. We then invert each of these synthetic spectra to calculate 30 new f_c estimates that provide a measure of the variance of each station estimate.

The initial f_c estimates must lie within the range of f_c's from inversion of the synthetic spectra and must not saturate at the bounds (15-2000 Hz). We also calculate the root mean square (RMS) at each station and inspect which stations show the best fits based on the RMS.

Once the corner frequency is determined, it can be related to the rupture radius, using (Madariaga, 1976):

$$r = \frac{\kappa \beta}{f_c}, \tag{2.7}$$

where f_c is the corner frequency, κ is a constant related to the radiation pattern, β is shear wave velocity and r is source radius. Madariaga (1976) showed that we expect the f_c to vary with azimuth around the focal sphere relative to the nodal plane of an event by as much as a factor of ~ 1.7 for P waves and up to ~ 2.5 for S-waves. κ averages this effect out by assigning κ as 0.32 for

P waves and 0.21 for S-waves. In the Brune model κ is derived from a simpler kinematic method and is around a factor of 2 larger than in the Madariaga model (Madariaga, 1976).

Using corner frequency estimates obtained by model fitting, we can use the Eshelby (1957) equation for calculating stress drops from a circular fault in an elastic half space using:

$$\Delta\sigma = \frac{7M_o}{16r^3}, \tag{2.8}$$

where M_o is the seismic moment that we estimate in section 2.4.2 and r is the fault radius from equation (2.7).

To calculate stress drops, we first determine the mean corner frequency of each event by averaging the initial f_c estimates over all stations, for a given event; therefore the mean f_c captures the station-station variability. The f_c uncertainty is then calculated by taking 1 standard deviation of the bootstrapped and initial estimates over all stations for a given event. We then calculate the stress drop using equation (2.4), and calculate the uncertainty for each measurement using standard error propagation (e.g., Fornasini, 2008) of the corner frequency. We only use estimates of stress drop where the standard deviation is less than the stress drop value. To calculate the uncertainty of the average stress drop for all events we combine the standard error from the stress drop distribution and the uncertainty from individual stress drop measurements.

2.4.2 M_w calculation

To verify contractor provided M_w estimates, we re-calculate M_w and compare estimates from this study to the contractor's. We calculate seismic moment using (Brune, 1970):

$$M_o = \frac{\Omega_o 4\pi\rho v^3 r}{R_o} \tag{2.9}$$

where Ω_o is the low frequency displacement-amplitude plateau, which is determined empirically by taking the mean signal of the displacement amplitude spectra between 20 and 40 Hz. ρ is density, r is the station to event geometric distance, R_o is the average radiation coefficient (0.52 for P-phases and 0.63 for S-phases) and v is the seismic velocity of the source rock. We use ρ = 2500 kgm^{-3} for the Keg-River limestone and a density of ρ = 2600 kgm^{-3} for the overlying shale formation, which are determined from sonic logs (Sayers et al., 2015).

For each seismic event, we calculate individual station magnitude estimates using P- and S-phases by re-arranging equation (2.3). Then we average the station M_w estimates to get the event estimate. We measure the uncertainty in this estimate using the standard deviation across station estimates to measure the M_w uncertainty for a given event.

2.4.3 Modelling attenuation

To constrain an attenuation model we assume that intrinsic attenuation is the dominant mechanism (e.g., Abercrombie, 1998). In doing so, we reduce the number of free parameters in equation (2.6) by determining Q, decreasing the non-uniqueness of f_c estimations. To model intrinsic attenuation we use (Abercrombie, 1997; Bethmann et al., 2012)

$$A(f) = A_o(f)e^{\frac{-\pi f t}{Q(f)}}, \tag{2.10}$$

where *A(f)* is the displacement amplitude spectrum at a station some distance from the source, A_o is the displacement amplitude at the source, or some distance closer to A, f is frequency and t is travel time between the locations where A_o and A are measured. Q as a function of frequency can be expressed as

$$Q(f) = \frac{-\pi f(t_1 - t_2)}{\ln(\frac{A_1(f)}{A_2(f)})}. \tag{2.11}$$

where $A_1(f)$ corresponds to the amplitude spectra at the top five stations, $A_2(f)$ corresponds to the amplitude at the bottom five stations and t_1 - t_2 is the travel time difference between a station pair. If the right hand side of equation (2.11) is a constant, this implies that Q*(f)* = Q and frequency independent Q is a reasonable approximation.

We use two methods to determine Q. In the first method, we calculate the attenuation of the wave field in the rock volume between the top five and bottom five stations. For each event, we calculate spectral ratios between five station pairs that are separated by the maximum possible distance (i.e., stations 1 and 30, 2 and 31, etc.). For each event we stack the signal obtained from all the station pairs to obtain an empirical path term. We then calculate Q*(f)* using equation (2.11). This method provides an estimate of the attenuation within the layer in which the geophones are situated (e.g., Abercrombie, 1998; Bethmann et al., 2012) but does not necessarily characterise the crustal attenuation of the underlying lithological units along the ray path.

To address this, we also estimate a whole path Q using idealised source spectra over 3 stress drops (1, 10 and 100 MPa), which represent the empirical range across stress drop studies (Abercrombie, 1995, 2021). Similar methods have been used to validate Q estimates by Ide et al. (2003) and Imanishi et al. (2004). To calculate idealised source spectra we determine corner frequencies which correspond to 1, 10 and 100 MPa stress drops. We calculate our own estimates of seismic moment in section 2.5.1. Then we use equation (2.6) to calculate the expected source spectra. To ensure the signal from the source model is larger than the observed spectrum, we fix the low frequency plateau of the idealised source spectra to 1.1 times the observed Ω_o. When using this method there are unexpected and unrealistic effects on *Q(f)* below 100 Hz, which are most likely caused by a slow hump in the spectral amplitude observed between 30-100 Hz (see Figure 2.13). Therefore to avoid potential artefacts in *Q(f)* we limit our analysis to frequencies above 100 Hz.

For each station we deconvolve the observed instrument corrected spectrum with the corresponding source model to obtain source corrected spectra (i.e., the path/site term) using 1, 10 and 100 MPa stress drops. We then stack spectral ratios across events at each station. This leaves us with 35 spectral ratios corresponding to each station along the borehole geophone array. Then we determine Q*(f)* at each station using equation 2.11.

2.5 Results

2.5.1 M_w calculation

In this section we calculate M_w to provide a comparison to contractor estimates. Where possible, we include seismic data from both wells, and use information from P- and S- phases. On average, we use 94 phase arrivals for each M_w estimate, across both wells. We calculate individual station M_w estimates and event estimates. Below $M_{w,c}$ = 0, most of our estimates lie within one standard deviation of contractor estimates apart from 5 outliers (Figure 2.6a). Above $M_{w,c}$ = 0, we find more discrepancy. 16 estimates of our M_w's are more than one standard deviation different to contractor estimates (Figure 2.6a).

To investigate the discrepancy in M_w estimates, we analyze the displacement amplitude spectra (Figure 2.6b) from the M_w = 0.2 outlier event, which shows the largest underestimate by the contractor and the M_w = 0.45 event, corresponding to the largest overestimate by the contractor (Figure 2.6a). The largest contractor underestimate is shown in Figure 2.6b. Assuming the contractor uses the same values of r, V_p and ρ, contractor estimates of Ω_o appear to correspond to the S-well spectra only (Figure 2.6b). The S-well shows lower spectral amplitudes than the K-well across the frequency range for many events, which is most likely caused by the greater distances that the seismic wavefield has travelled compared to the K-well.

To match the largest contractor underestimate of 0.6 M_w units (i.e., 8 times more seismic moment in our estimate), either r or ρ need to be a factor of 8 smaller. As we consider the shortest possible path from event to station it is not possible for r to decrease. If ρ is a factor of 8 smaller, it would be unrealistically small (i.e., ρ = 310 kgm^{-3}) compared to a density of $\sim$ 2500 kgm^{-3} expected from the Keg-River limestone (Sayers et al., 2015).

For contractor overestimates, the largest discrepancy is 0.9 M_w units (i.e., a factor of 22 times more seismic moment in contractor estimates). It is likely that r is slightly larger because we assume a straight line path from source to receiver. However, because density between layers is similar (Sayers et al., 2015), it is unlikely that ray paths will be significantly longer than a straight path. If density changes, it would also need to increase by an unreasonably high value (i.e., 55,000 kgm^{-3}) to explain the difference.

Thus, single parameter changes do not explain the M_w outliers from this study compared to the contractor. Methodological differences may explain the discrepancy between our estimates and contractor estimates but the contractor's methods are not provided. For the purpose of this study we use our own estimates of M_w.

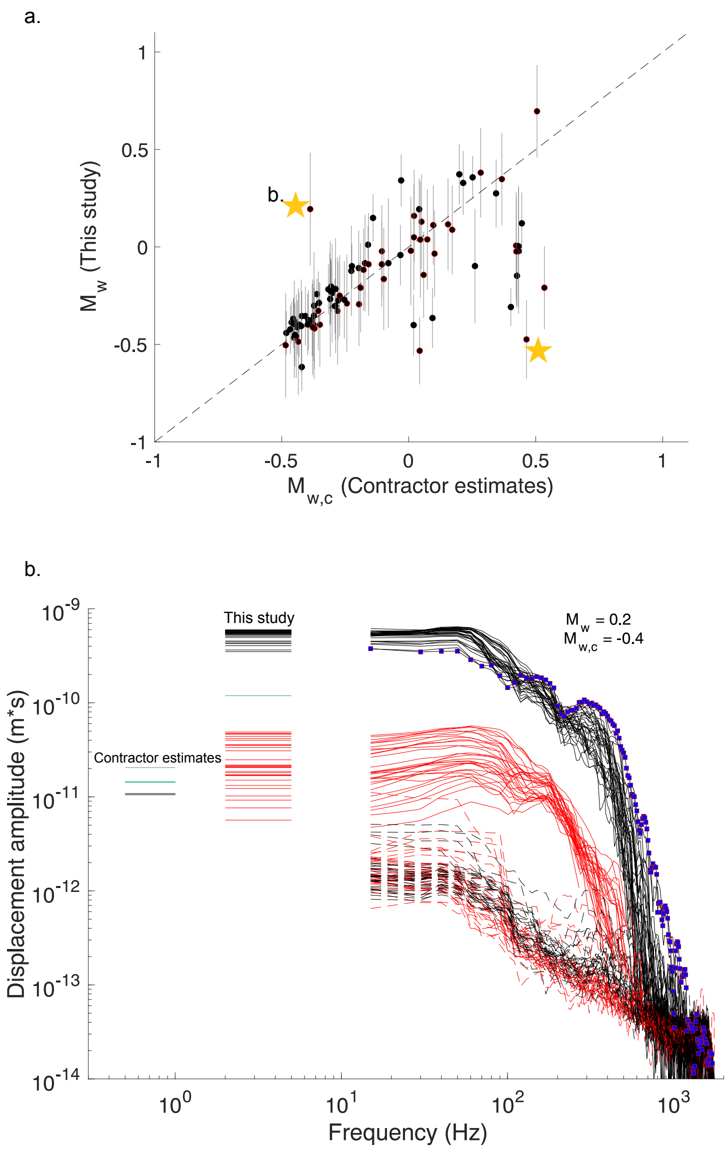

Figure 2.6: Comparison of our moment magnitudes with those of the contractor. (a) Event and station M_w estimates of 94 events considered for source parameter estimation in section 2.5.5 using P- and S-phases. (a) Average magnitudes (circles) with $\pm$ 1σ standard deviation (grey error bars) for events recorded by one borehole array (black circles) and both borehole arrays (black circles with red edge colour). Yellow stars highlight the largest deviations (b) Displacement amplitude spectra (P-phase) of signal and noise from all stations for an outlier event, demonstrating an underestimate of contractor estimates compared to estimates in this study. Thin red and black solid lines are spectra from the S- and K-well, respectively. Dashed red and black lines are the pre-event noise spectra from the S- and K-well, respectively. Thick horizontal lines indicate Ω_o estimates of spectra with the same colour. Blue squares show frequency sampling space (10 Hz). Grey horizontal lines show implied contractor Ω_o's. Green horizontal lines show median Ω_o estimates.

2.5.2 Spectral features of noise

In this section, we analyse features of the noise spectra to better understand the instrument response, as are summarised in Table 2.1. We start by analysing spectograms of seismic events in NEZ orientation and then analyse the pre-event noise along both wells. At most stations we observe unexpected peaks in the noise spectra that are continuous.

We select ~ 4 minutes of seismic data from consecutive event-separated SAC files in stitched events and identify systematic features in the spectograms. Along both wells, peaks are strongest in the Z-component, though observable across all components. At the K-well, the shallowest stations (i.e., stations 1-10) shows a peak at ~ 400-600 Hz (Figure 2.7a). Towards deeper stations, the peak migrates to a lower frequency band at ~ 250-400 Hz (Figure 2.7b). At the S-well, all stations show a clear peak at 50-80 Hz (Figure 2.7c and d). At the shallowest station, we observe peaks at ~ 300-400 Hz (Figure 2.7c). Towards the deeper stations, we observe a faint higher frequency band peak at ~ 500-700 Hz (Figure 2.7d).

Next, we analyse the pre-event noise from the far-field displacement of all 112 events on NEZ components using a 0.1 second time window (Figure 2.8). Most stations show amplification features that usually appear as notches. Along the K-well the pre-event noise shows high frequency noise amplifications that are strongest on the Z and N components. The two clearest resonance features are highlighted in Figures 2.8a, c and e at ~ 450-600 Hz (Noise Feature 1) and ~ 250-400 Hz (Noise Feature 2). Noise Feature 1 (NF1) appears to be systematically stronger at shallower stations (i.e, stations 1-10) whilst Noise Feature 2 (NF2) appears to be systematically stronger at deeper stations (i.e., stations 27-35). However, there is still variation from station to station (e.g., station 35 does not show a particularly strong level of NF2).

Along the S-well the clearest feature is a notch at ~ 550-650 Hz which appears strongest at the deeper stations (i.e., 20-35). We also observe a clear sharp increase in the spectra below 100 Hz, which may correspond to the strong peak seen in the stitched event spectograms at 50-80 Hz (Figure 2.7).

Feature	Frequency (Hz)	K-well stns	S-Well stns	CMP
NF1	450-600	1-10	-	N/Z
NF2	250-400	27-35	var	n/a
NF3	550-650	-	20-35	n/a
NF4	50-80	-	All	n/a

Table 2.1: Noise features. The K- and S-well columns show which stations show the feature strongest. The CMP lists the components where the feature is strongest. A dash indicates the feature is not seen. var indicates that the feature is not clearly systematic to certain stations and n/a means that the strongest component is not obvious.

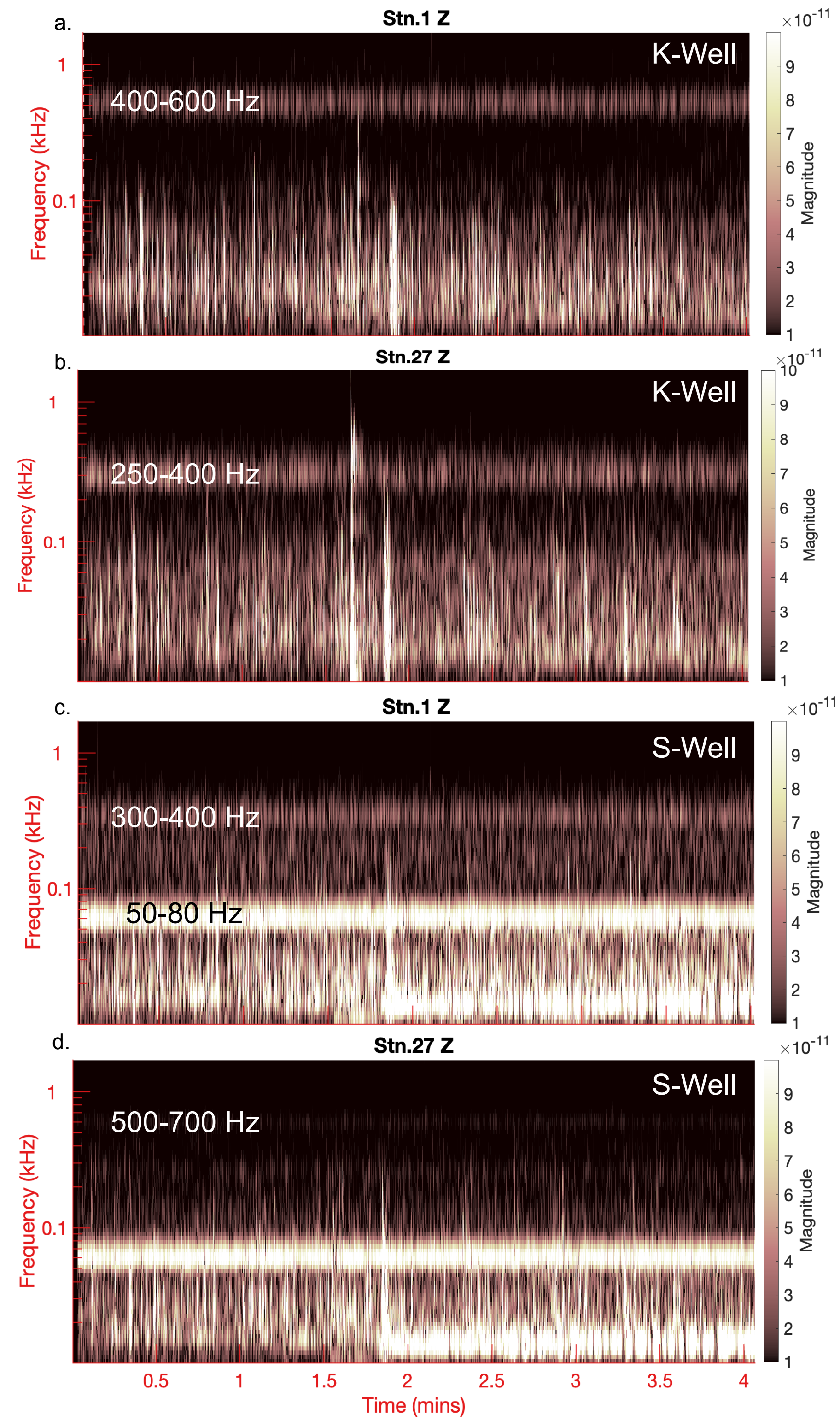

Figure 2.7: Continuous wavelet transforms of ~ 4 minutes of stitched seismic events, showcasing salient noise peaks in the Z-component at (a) K-well, station 1, (b) K-well, station 27, (c) S-well, station 1, (d) S-well, station 27.

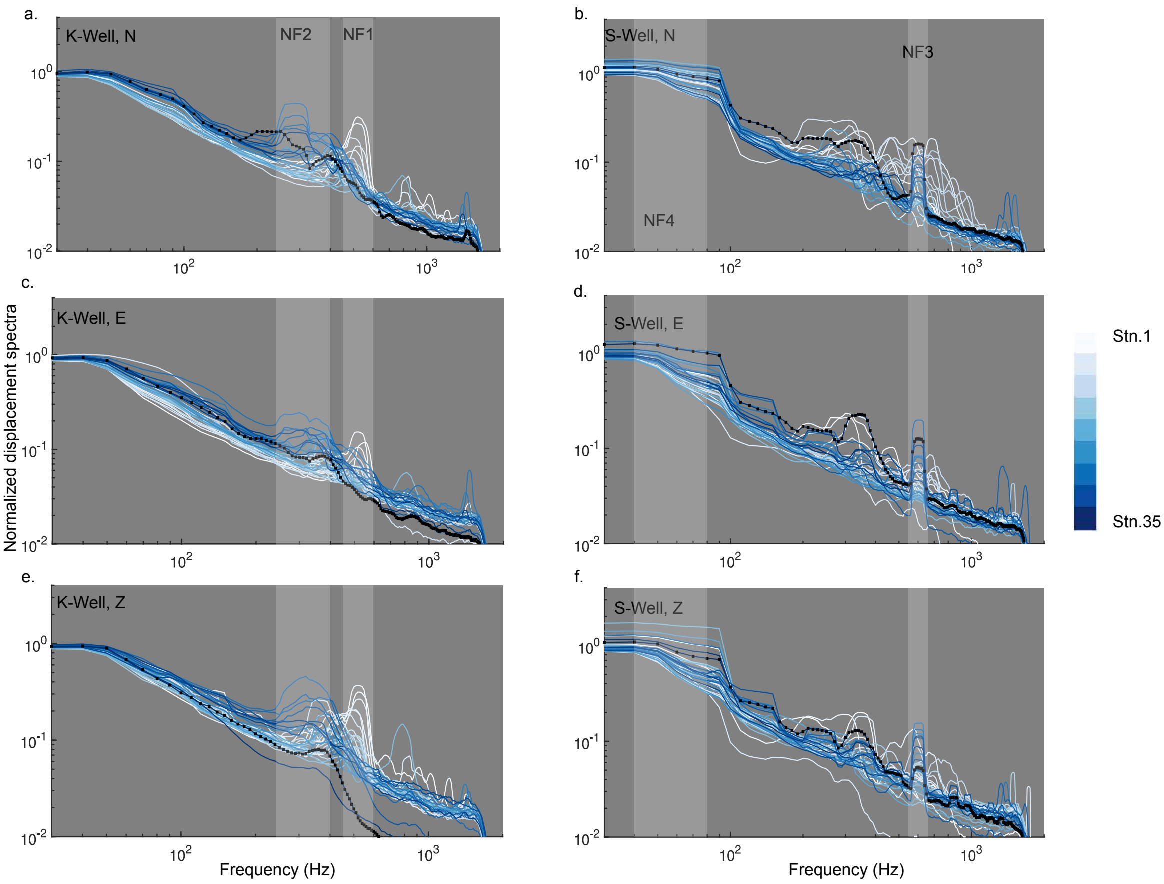

Figure 2.8: Systematic resonances in pre-event noise using 112 events from the (a, c and e) K- and (b, d and f) S-well. Each line represents the stacked pre-event noise spectra across events and are colour coded according to station depth where darker blue indicates a deeper station along the borehole array. Noise Features (NF) are highlighted with patches and are annotated according to Table 2.1. Black squares show frequency sampling points for the deepest station (i.e., station 35).

2.5.3 Station limitations

Next we investigate the limitations on retrieving source parameters based on station position in the borehole geophone array. While getting closer to the seismic source should enable us to retrieve high frequency information, and better constrain earthquake source models, we find that deeper stations are systematically more compromised in retrieving high frequency information along both borehole geophone arrays.

To visualise the issue, we normalise P and SH spectra to the first Fourier coefficient of the signal using the shallowest (i.e., station 1) and deepest station (i.e., station 35). We then also normalize the noise to the first Fourier coefficient of the signal such that the point of intersection between signal and noise corresponds to SNR = 1 in Figure 2.9.

To guide the eye we determine theoretical model curves using Q = 170, and determine travel times to stations by fixing the S-wave speed to 3800 ms^{-1} and adjust the distance travelled to the best visual fit. The aim here is not to provide constraints on the attenuation model but rather to display the shape of the expected spectrum against the observations at stations 1 and 35.

At station 35, the P-phase clearly shows a severe loss of high frequencies above approximately 400 Hz, which is likely associated with f_{max} (Figure 2.9a). As a result, high frequencies deviate significantly from the expected Brune spectral shape, preventing an acceptable model fit to the data. We find that a κ modified model (Ktenidou et al., 2014) does not visually improve the fit. The theoretical curve for Station 1 shows a significantly better explanation of data between around 100 - 500 Hz, but underestimates the low frequencies (i.e., 30 -100 Hz).

From observing the SH-phase spectra in Figure 2.9b, the P-wave coda causes resonances in the SH phase arrival, which is especially noticeable in the deepest stations. The shallower stations on the shear wave components show the cleanest spectra, but have a relatively small bandwidth of good SNR. For this reason we exclude shear waves from further analysis and only consider P-phase arrivals at the K-well when determining source parameters in section 2.5.5. As we exclude the S-well, we are now left with 94 events.

We further constrain which stations and phase arrival we can use for estimating stress drops. The deepest stations (i.e., stations 15-35) along both wells have a high frequency fall-off that is severely affected by f_{max}. This is demonstrated for station 35 in Figure 2.9a, as annotated. Therefore we also limit our analysis to stations 1-15 when determining source parameters in section 2.5.5.

To further investigate the nature of the resonances we select a cluster of seismic events co-located within 100 m of a reference event (i.e., target event) and highly cross correlated between 60-300 Hz with the chosen target event. If two co-located events are highly cross correlated (i.e, CC > 0.9), we should be able to assume that the path and site effects recorded at a single station should be approximately the same, and that any variation should come from the source term. Figure 2.10 shows significant variation in the expression of resonances from a cluster of seismic

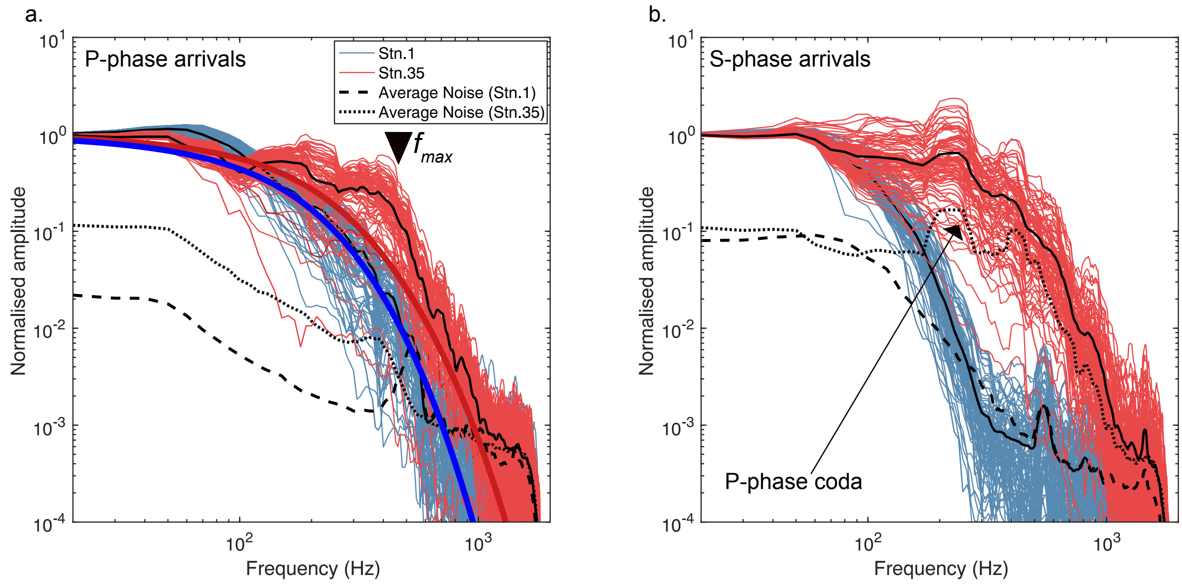

Figure 2.9: Normalized spectral amplitude of station 1 and 35 across all events along the K-well, with annotations pointing out limiting effects on deeper stations. Solid black lines represent the mean signal for station 1. Thick red and blue curves in (a) represent theoretical source models for P-phase arrivals at station 35 and station 1, respectively. (b) Lines correspond to same description as (a) for the SH-phase arrival.

events co-located and highly cross-correlated with a target event, when spectra are normalised to the lower frequency plateau (15-40 Hz). In some cases there is a factor of ~ 10 difference in the relative amplitude between events. These resonances are unlikely to result from source term variations. Instead, they suggest a sensitivity to small differences in path or variable site effects. This sensitivity will persist into spectral ratios and may thus compromise the validity of the approach. Stacking the EGFs may improve the stability of the spectral ratios and is likely a better approach, but resonances may still not be completely removed.

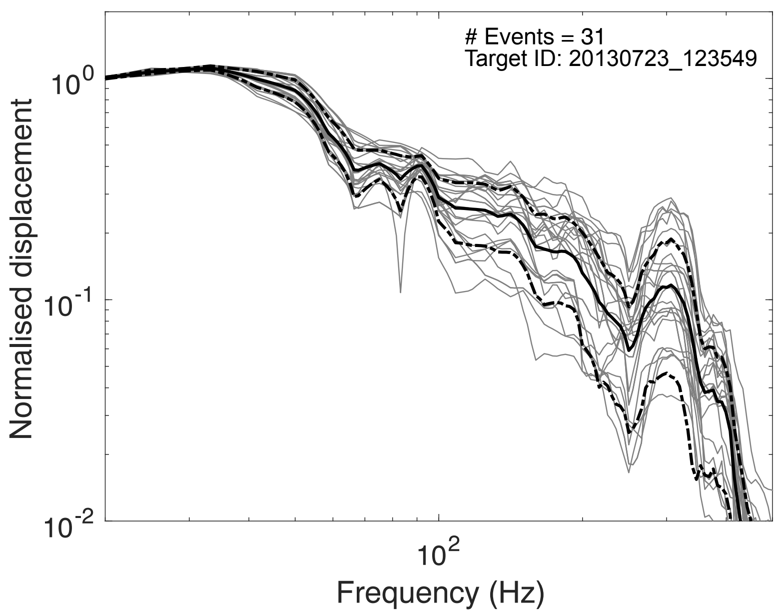

Figure 2.10: Normalized displacement-amplitude spectra of the P-phase arrival from a cluster of co-located microseismic events recorded at station 9. Grey solid lines show normalized displacement amplitude spectra. Black solid line shows average signal and dashed lines show $\pm 1\sigma$ at each frequency point. We found 31 nearly co-located events within 100 m and high cross correlation (i.e. CC > 0.9) with the target event.

2.5.4 Modelling crustal attenuation (Q)

We consider two methods of determining Q from P-phase arrivals using events recorded at the K-well. For both methods we consider the possibility of frequency independent and frequency dependent attenuation. Our analysis suggests that a frequency independent model provides agreement with observed data. For the purposes of calculating Q using Method 1 we restrict our analysis to events that occur below the shale formation such that spectral ratios between stations correspond to a clear difference in travel time (86 out of the 94 events); for Method 2 we use all 94 events.

2.5.4.1 Method 1

Our ability to resolve attenuation using Method 1 is limited by the maximum distance between stations along the borehole array. The low frequency amplitudes of the deepest stations are smaller than the shallowest stations at the K-well, which might be caused by a radiation pattern effect. Alternatively, the differences in amplitude might be due to crustal amplification as a result of impedance contrasts or a temperature gradient effect in the borehole. Relatively high frequencies are enriched at deeper stations because the effect of attenuation dominates. As a result, the deepest station only shows a clearly larger amplitude at or above ~ 180 Hz (Figure 2.11a). Therefore, we restrict our analysis to 26 out of the 86 events where the spectral ratio between the deep and shallow stations is > 1 at 180 Hz (Figure 2.11a). By limiting our frequency range to above 180 Hz we are using spectral information above the apparent corner frequencies observed at most stations, but it is our best lower frequency limit, as shown in Figure 2.11b. On average, above 180 Hz, we obtain a Q estimate of 160 ± 50 using Method 1. The large uncertainty (± 50 using 1σ) reflects the bumps in the spectra.

2.5.4.2 Method 2

To avoid the effect of resonances, we limit our analysis to the top five stations of the K-well array for Method 2. Between 100 -280 Hz, the stacked spectral ratios from stations 1-5 show a relatively straight line in log-linear space (i.e., constant Q), as shown in Figure 2.12. Above 280 Hz, resonances introduce scatter into Q measurements, which is especially noticeable at station 3 (Figure 2.12b, d and f). Q uncertainty increases towards lower stress drops because resonances are relatively larger when the spectral ratio is calculated in the high frequency decay portion of the source spectrum relative to the low frequency plateau for higher stress drops. We also observe a systematically higher Q for lower stress drops because less attenuation is needed to explain the reduction in amplitude. For each stress drop model, we calculate an average Q across all stations as Q = 180 ± 40, Q = 120 ± 20 and Q = 110 ± 20 for a 1 MPa, 10 MPa and 100 MPa source model, respectively.

2.5.4.3 Comparison of Q methods

Both methods show that a frequency independent attenuation model is broadly consistent with observed data above 180 Hz for Method 1 and 100 Hz for Method 2. The larger uncertainty associated with Method 1 means that Q is not statistically different relative to any of the Q estimates using Method 2. For this reason, we only consider the 3 estimates from Method 2.

To assess how well the Q values explain the observed spectra, we apply Q corrections to 1, 10 and 100 MPa source models (Figure 2.13). Between 30 - 80 Hz, modelled spectra are smaller than the data. From 100 - 400 Hz the models explain the data relatively well. Above 400 Hz, we see bumps in the spectra, which causes an underestimate by the model. For determining corner frequencies in section 2.5.5, we consider all 3 values of Q from Method 2.

Whilst a frequency independent Q appears to provide a decent explanation of the data, the resonances might mask a frequency dependence which may be more obvious at deeper stations. However, the deeper stations are compromised by stronger resonances, and are therefore not included in the Q calculation.

Importantly, corner frequency visually appears to be relatively stable across the range of 1.1 magnitude units (Figure 2.13), although quantitative estimates are needed in case the differences emerge given different distances of the path. Nonetheless, because of the relatively small M_w range we are unlikely to resolve significant differences in apparent corner frequency. Additionally, the percentage of energy removed becomes exponentially larger at higher frequencies, which also causes a relatively stable apparent corner frequency.

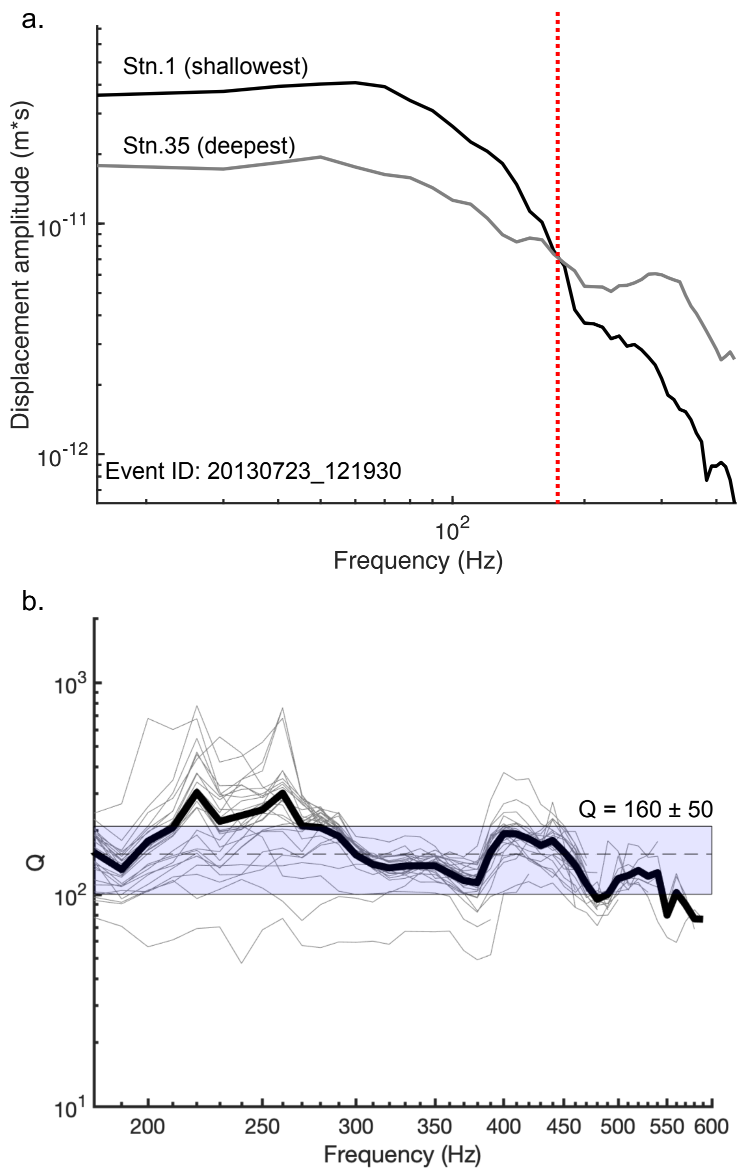

Figure 2.11: Determination of frequency independent Q using station pairs along the geophone array (Method 1) at the K-well. (a) An example of a station pair showing displacement amplitude spectra of P-phase arrivals. Dotted red line is the limit above which signal from the deeper station is larger than shallower station. (b) Q against frequency for all 26 events we consider for Q estimation using Method 1. Each grey line represents the stacked signal across five station pairs. The thick black line shows the average signal over all the stacks for all events. Dashed black line shows average Q estimate and blue patch shows uncertainty corresponding to $\pm 1\sigma$ standard deviation.

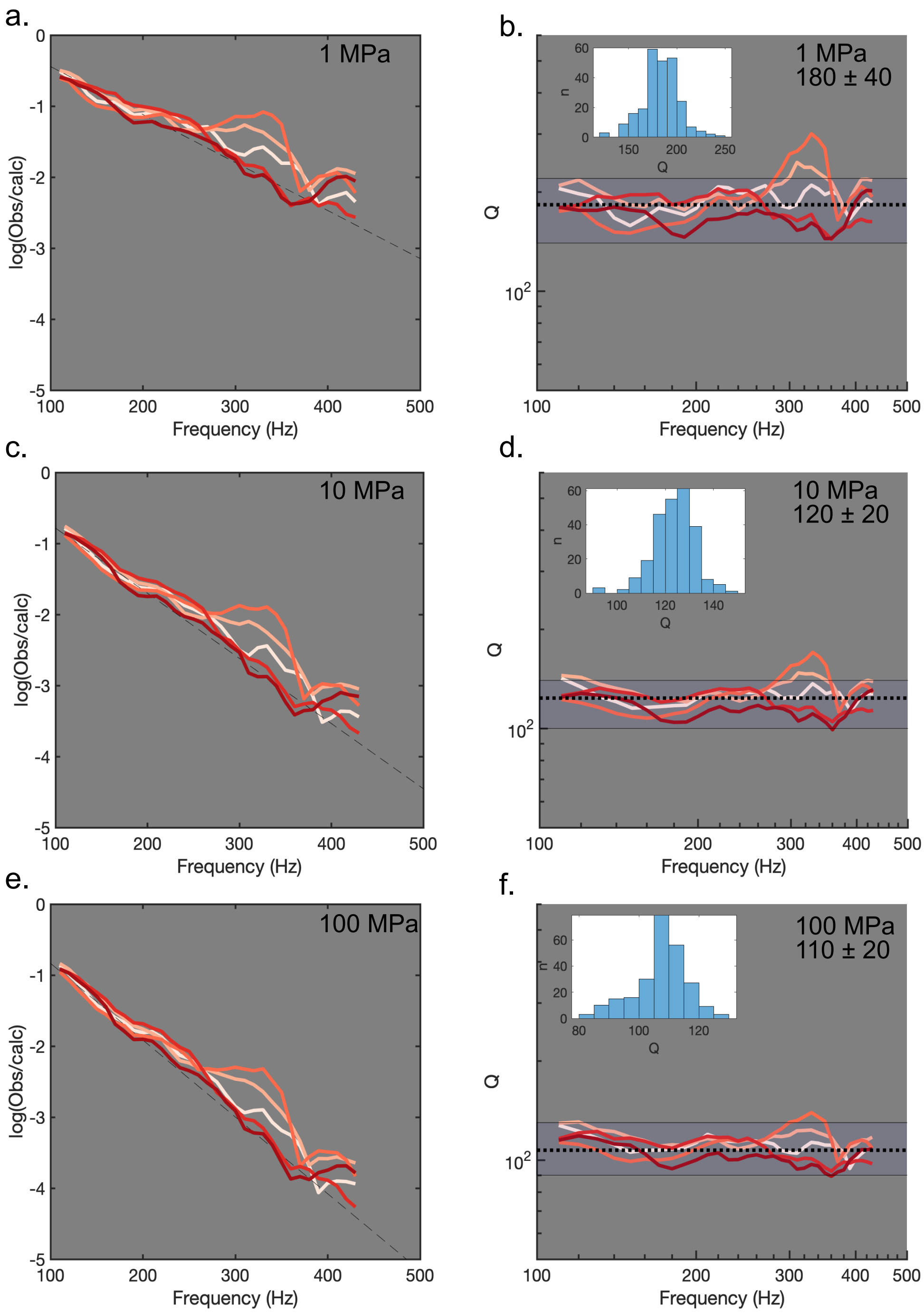

Figure 2.12: Empirical determination of whole path Q using idealised source spectra assuming 1 MPa, 10 MPa and 100 MPa stress drops from 94 events at the K-well (stations 1-5). (a, c and e) coloured solid lines show the stacked spectral ratios between the instrument corrected amplitude and the idealised source spectra against frequency. Black dashed lines shows a linear fit to the deepest station. (b, d and f) Q calculated directly from the spectral ratios as a function of frequency for (b) 1 MPa (d) 10 MPa and (f) 100 MPa source models. Black dotted lines show the average Q with $\pm$ 1σ range as a light blue shaded area. Darker red denotes a deeper station in the borehole array. Inset plot shows histograms of Q estimates across different frequencies and stations.

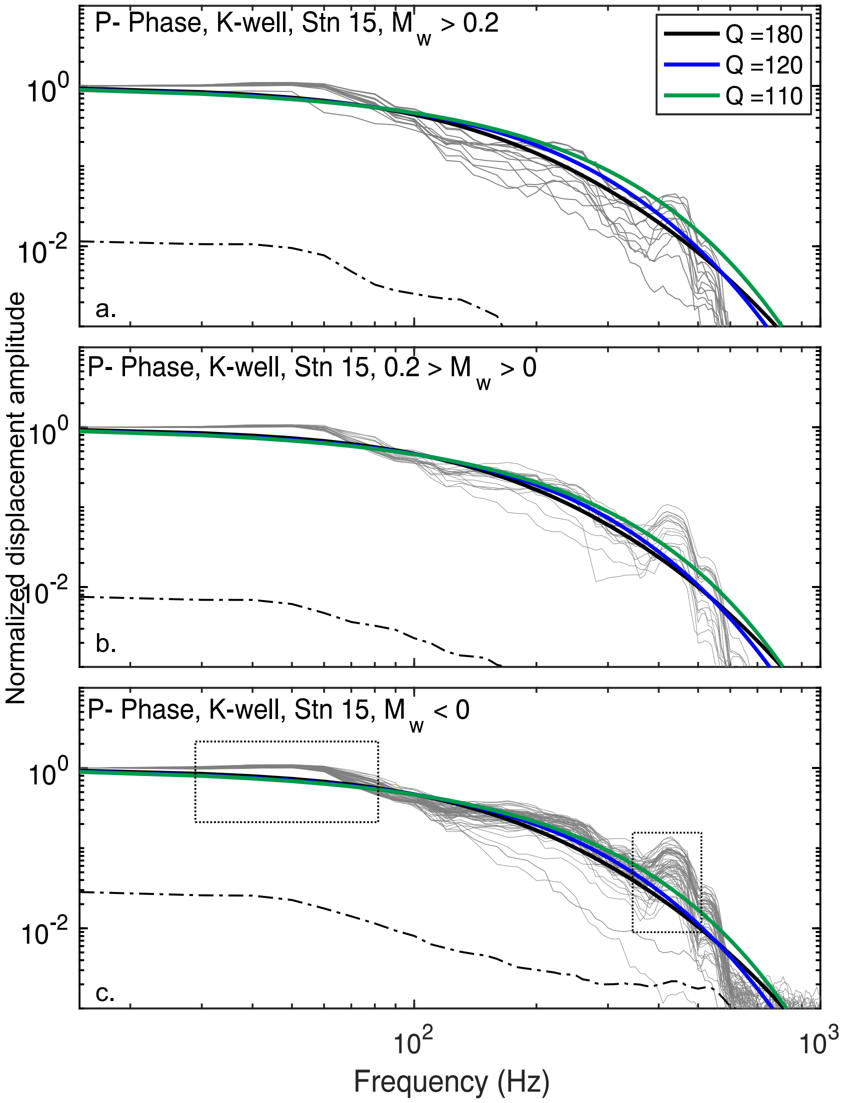

Figure 2.13: Forward modelled far-field spectra using three candidate models for crustal attenuation compared to observed data based on results from Method 2 of measuring attenuation. Grey thin lines show normalized displacement spectra of the P-phase arrival at station 15 from 94 events at the K-well. Spectra are separated into 3 magnitude bins. (a) $M_w > 0.2$. (b) $0.2 > M_w > 0$. (c) $M_w < 0$. Dashed black boxes highlight deviations from the expected spectral shape. Each curve shows the theoretical model using the average Q estimates from Method 2. Black dot-dashed lines shows average pre-event noise.

2.5.5 Corner frequency and stress drop estimation

As discussed in sections 2.3.2, 2.5.2, and 2.5.3 the bandwidth limitations, f_{max} effects and high frequency resonances compromise the robustness of source parameter estimates. Notwithstanding these limitations, we carefully attempt corner frequency and stress drop estimations. We determine f_c for each station using the method outlined in section 2.4 for three different Q estimates, as explained in section 2.5.4. Then we calculate event estimates of f_c to compute stress drops. To test the hypothesis that injection pressure affects stress drop, we select events at a period where we might identify a trend from the injection point to the bottom of the fracture zone. Therefore we limit our analysis to events associated with injection of stage A14 (i.e., 90 out of the 94 events at the K-well).

By analysing the distribution of stress drops from three crustal attenuation models, we disqualify models that provide unrealistic stress drop values (e.g., > 400 MPa) and those that generate a broad range (e.g., > 100 MPa), as shown in Figure A.1. Based on these criteria, Q = 110 and Q = 120 provide stress drop estimates that are physically unrealistic (i.e., > 500 MPa). Such high estimates are unlikely for strike-slip faults in the upper crust, given that shear strength is not expected to exceed ~ 20 MPa (Streit, 1997). Q = 180 provides the most physically reasonable estimates of stress drop between 0.1-9 MPa. For this reason, we only consider the Q = 180 model further. This Q value falls within the uncertainty of Q = 226 ± ~ 70 calculated by Yu et al. (2020) for seismic events recorded in the crystalline basement at a hydraulic fracturing pad 240 km away from this study, which adds further credibility to our estimate.

Considering that there are some systematic differences between source and model, as mentioned in section 2.5.4, we only use the most robust fits to calculate first order estimates of f_c. From visual inspection, stations with a root mean square (RMS) < 4 show the most robust fits, which we use as an additional criterion. Using all the fitting criterion, fits are decent, as showcased in Figure A.2.

Results of corner frequency and stress drop estimates are shown in Figure 2.14. We do not know whether the contractor used a Brune or Madariaga model, therefore we show contractor values as a range spanning both. Corner frequency estimates calculated in this study are on average larger than estimates made by the contractor and lie mostly between the 1-10 MPa theoretical stress drop lines (Figure 2.14a). Along the borehole array, corner frequencies do not systematically depend on geophone depth (inset Figure 2.14a). We find a mean corner frequency of 210 Hz ± 30, using the standard deviation across our estimates (± 1σ).

Based on observations of a systematic f_{max} at 400-500 Hz along the K-well, corner frequencies are likely underestimated, especially for smaller events, which may explain the shallower gradient of $f_c \propto M_w^{-0.35}$ from the line of best fit compared to what we expect from self-similar scaling ($f_c \propto M_w^{-0.5}$). Note that we use here the moment magnitude instead of seismic moment as the self-similar scaling variable. Therefore our mean corner frequency and stress drops are probably rough estimates of possibly larger values. Corner frequencies below f_{max}

should be actual corner frequencies, even if uncertain. Values above f_{max} may represent f_{max} rather than f_c. The lack of estimates near ~ 100 Hz is likely a source effect caused by the largest size of seismic events we use, which places a lower limit on the corner frequencies available to analyse. The upper limit of f_{max} can be seen as the cut-off in Figure 2.14a and scaling in Figure 2.14b.

We calculate an average stress drop of a 1.6 MPa ± 1.2 using the geometric mean of the stress drop. Our results are broadly in the expected range of 0.1 - 100 MPa observed from earthquakes (Abercrombie, 1995) assuming self-similarity (Figure 2.14b). The scaling of stress drop with M_w that we report in this dataset is also seen in the other datasets (Figure 2.14b). In our case, the scaling is more likely related to an upper limit of corner frequency resolution than a source effect.

Spatially, there are two populations of events. The shallower population spans the bottom of the stimulated rock volume into the underlying limestone; the deeper population is a few hundred metres deeper in the limestone. Stress drops do not clearly vary systematically between these populations with depth or distance from point of injection (Figure 2.15). We also observe no clear differences between events that occur in the stimulated rock volume and the underlying limestone.

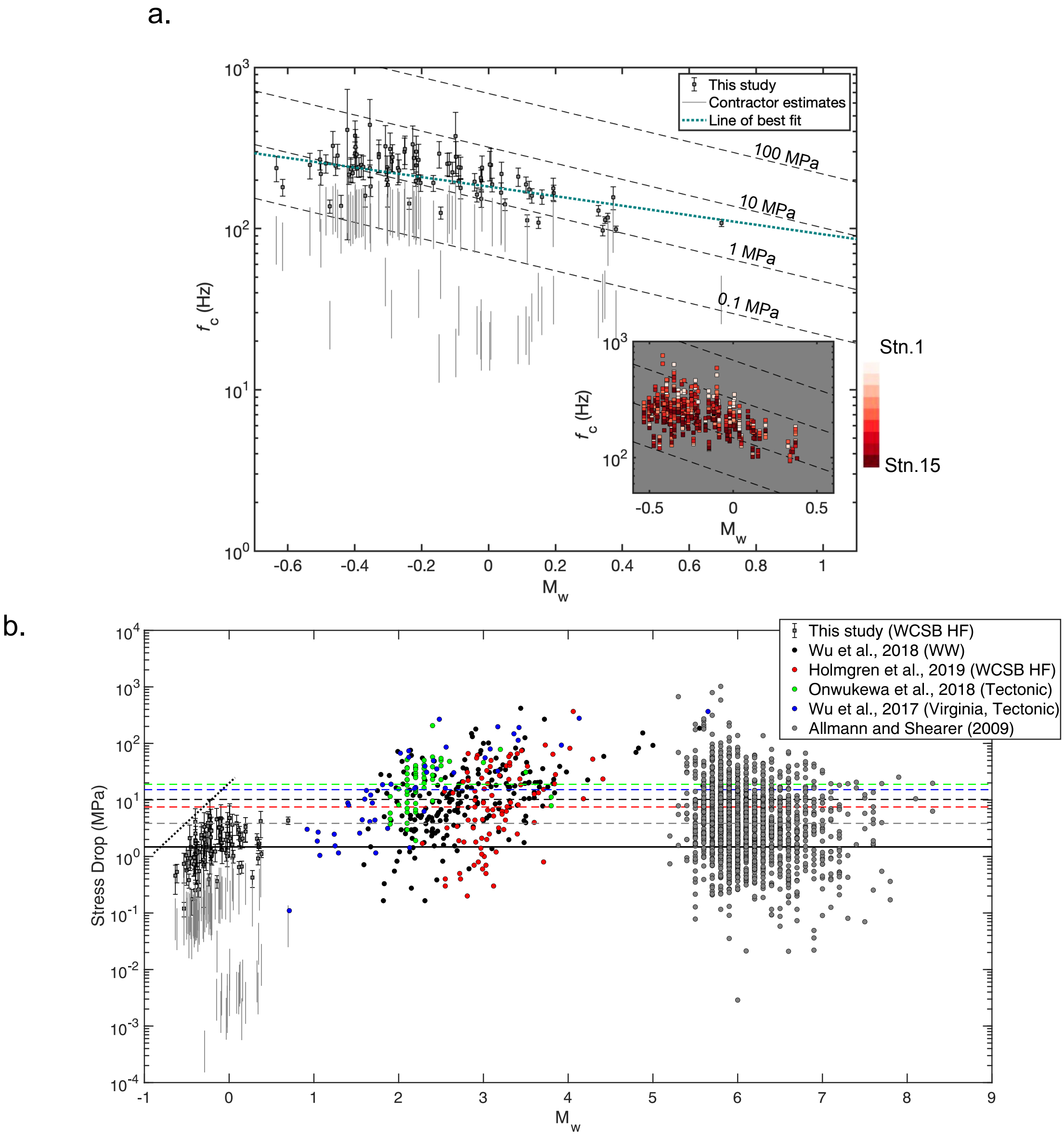

Figure 2.14: Best available source parameter estimates compared to contractor estimates and source parameter studies from the literature. (a) P-phase corner frequency against M_w. Black squares show results from this study and grey vertical lines show contractor estimates over the range corresponding to a Brune and Madariaga source model. Inset shows individual station estimates of corner frequency at the K-well; darker red squares indicate deeper stations. On main and inset plot, theoretical lines of corner frequency against magnitude assume an S-wave velocity of 3800 ms^{-1} and a Madariaga (1976) crack model. (b) Stress drop vs M_w compared to contractor estimates, one hydraulic fracturing (HF) dataset, three tectonic datasets, a waste water (WW) induced dataset and a global study by Allmann and Shearer (2009). The black horizontal solid line shows the mean estimate of stress drop from this study.

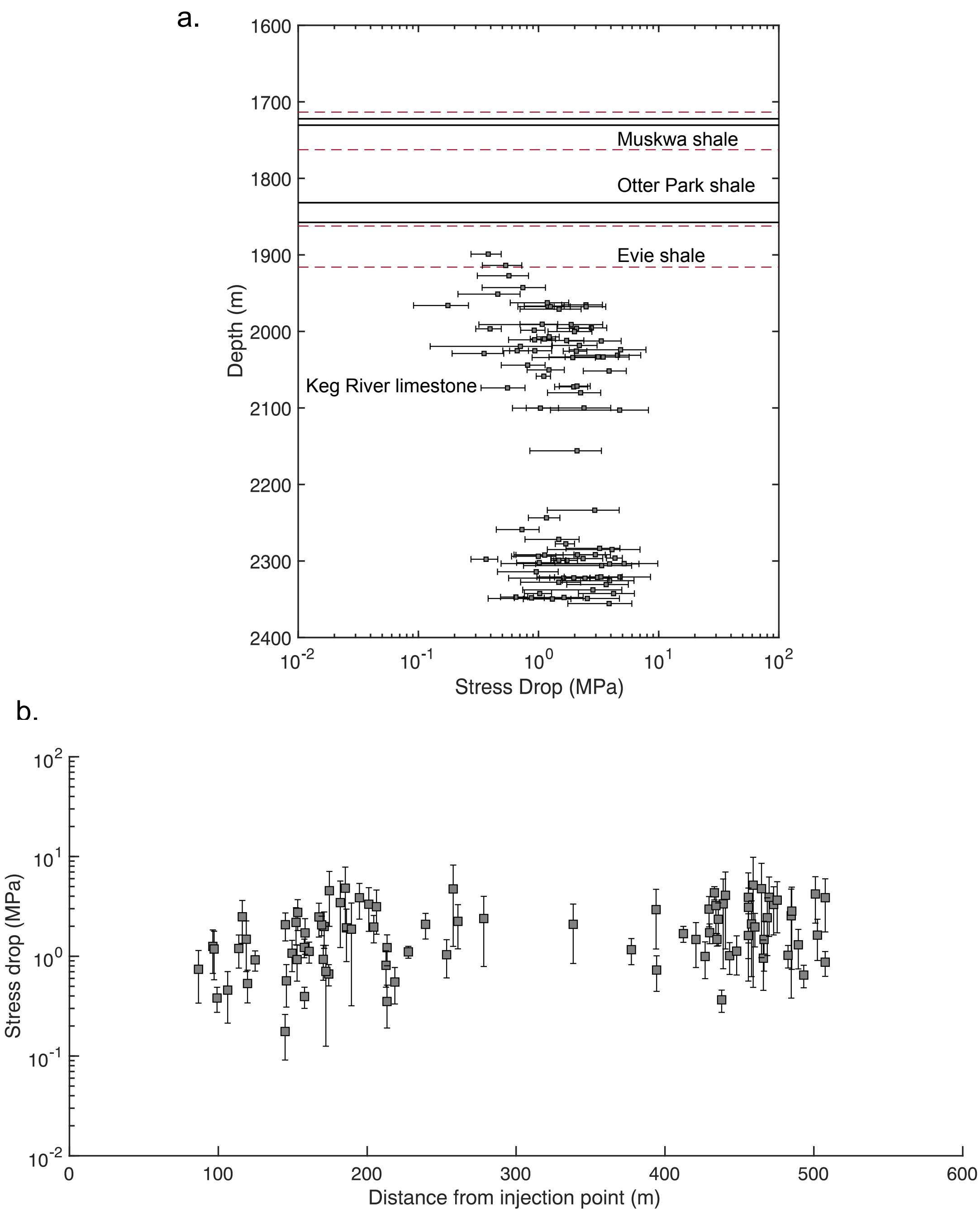

Figure 2.15: (a) Stress drop against depth and (b) distance from seismic event to injection point.

2.6 Discussion

2.6.1 Origin of the observed amplifications

We observe unexpected high frequency amplifications along the two borehole arrays considered in this study. Resonances are typical in borehole geophone arrays (e.g., Tary et al., 2014; Vaezi and Van der Baan, 2014; Zhang et al., 2018; Yaskevich et al., 2019) and must be carefully analysed to determine which stations are appropriate for source parameter estimation. Here, we attempt to qualitatively identify the clear systematic features across both wells, although there is variation from station to station and between events. Understanding the provenance of the resonances may also help advise operators on how to better deploy the geophones.

2.6.1.1 Noise features (NF1-3)

We identify three high frequency systematic noise features (NF1-3) across both the borehole arrays from ~ 4 minutes of stitched seismic event data. NF1 are resonances at ~ 450-600 Hz, NF2 are resonances at ~ 250-400 Hz and NF3 is a notch at ~ 550-650 Hz. These features are unlikely to be explained by source effects, which are low frequency and not continuous. Tary et al. (2014) show that fluid-filled fractures from the opening of perforations (~ 0.01 m), interconnected fractures and larger cracks (> 5 m), resonate between 17-31 Hz, which is significantly below the frequency content of NF1-3.

Resonances due to spurious frequencies and self noise are a more plausible explanation of NF1-3, as they can explain both the high frequency nature and the continuous appearance over seismic events. Geophones are prone to off-axis excitation above the spurious frequency limit of 365 Hz and NF1-3 are close to or above the spurious frequency limit. In some cases individual stations show resonances that are below the spurious limit, which is surprising given the instrument specification provided limit of 365 Hz. Spurious frequencies have been recognised as a major challenge for recording accurate phase arrivals (Sleefe et al., 1993, 1995; Faber and Maxwell, 1997).

The clamping system that locks the geophone in place is another potential source of resonances (Sleefe et al., 1993), which is likely to be a continuous feature. The challenge is usually that there are only 2 points of contact between the geophone sonde and the borehole, which can give rise to resonances (Gaiser et al., 1988). For this dataset, we are not provided with cement bond logs so we must infer how good coupling is from the data. Clamping issues are observed by Gaiser et al. (1988), who attribute 130-140 Hz resonances to the coupling of the geophones. A more recent study by Zhang et al. (2018) attributes two modes at 120 and 320 Hz to coupling issues. This could explain the presence of NF1-3, even though the resonances in this study are at higher frequencies. It is possible that with more advanced and better instrument setup, resonances are pushed to higher frequencies.

2.6.1.2 Noise feature 4 (NF4)

This feature has a lower frequency content of ~ 50-80 Hz and appears relatively strong in spectograms, but does not appear in the pre-event spectra. The electrical noise is a likely candidate for the cause, which is expected at around 60 Hz (Tary et al., 2014), falling within the range observed. The pumping of fluids may also cause relatively low frequency resonances, however, we are unable to verify this because there is no seismic data before pumping starts.

2.6.2 Implications of resonances

Most source parameter studies rely on the assumption that the path and site effects of co-located events can be considered the same for analysis at a single station. In this study we find that highly cross correlated, co-located phase arrivals (CC > 0.9) between 60-300 Hz show significant variation in the strength of high frequency resonances. This observation can be explained by slight variations in the source, path or site that generate different resonance strengths, which may compromise the spectral ratio approach as resonances are not removed. Stacking the EGFs might provide a more stable signal but may not completely remove resonances.

Resonances introduce significant scatter into empirical measurements of intrinsic attenuation and therefore limit our ability to resolve robust stress drop estimates. When using either method for determining Q, the uncertainty in Q is large (± 20-50). Other studies that have measured Q using similar techniques to this study (e.g., Abercrombie, 1998) find significantly less uncertainty in Q, although the frequency range of interest is lower (i.e., 1 - 100 Hz), and resonances are likely less severe.

2.6.3 Source parameters

2.6.3.1 Corner Frequencies

Despite the limitations in retrieving faithful representations of the source spectra, it is still useful to determine corner frequency and stress drops and compare to other regional and global estimates. We calculate 743 initial estimates of P-phase Madariaga corner frequencies and 22,380 estimates in total (including synthetic spectra from bootstrapping) with a range of 90-750 Hz and a mean of 210 Hz ± 30 (± 1σ). We first discuss the uncertainties in determining f_c and then interpret our results.

One important observation from the spectra is that the apparent corner frequency appears relatively constant over a 1.1 M_w range. This observation can be explained by disproportionately larger attenuation at high frequencies (i.e., > 100 Hz) of the dominant signals we are analysing (Deichmann, 2017). Other studies have also highlighted the severe reduction of energy at high frequencies (Eaton et al., 2014; Butcher, 2018).

Corner frequency resolution is limited by a clear cut-off frequency at ~ 400-500 Hz for P-phase arrivals the K-well. The cause of the cut-off could be related to f_{max}. Although f_{max} was initially understood as a local site effect from shallow crustal attenuation (Hanks, 1982; Anderson and Hough, 1984), f_{max} could still apply to borehole geophones. Whilst one might expect clean signals from borehole geophones, local site effects should not be ruled out (e.g., Ide et al., 2003). We should have the bandwidth to measure lower corner frequencies, therefore the lower f_c limit of ~ 100 Hz is likely a source effect.

It is likely that a low SNR limit and bandwidth limitations are contributing to energy loss and a relatively constant corner frequency. Even though we estimate that at least 75 % of the seismic energy is captured, the absence of 25 % of high frequencies could contribute to the saturation of f_c in the dataset. For microseismic source parameter studies, the underestimation of radiated energy is a commonly observed feature (e.g., McGarr, 1999; Ide and Beroza, 2001; Ide et al., 2003).

Compared to the global study by Allmann and Shearer (2009) of P-phase spectra from global tectonic seismicity, f_c estimates in this study lie in the expected range for negative magnitude earthquakes, assuming a constant S-wave velocity of 3800 ms^{-1} and a Madariaga (1976) circular crack model. This supports the invariance of stress drop with respect to earthquake size over the large scale. Other studies of microseismic source parameters have also supported self-similarity into negative magnitudes (Hiramatsu et al., 2002; Baig et al., 2012).

2.6.3.2 Stress drops

We determine Madariaga stress drop estimates from 86 out of the 90 events with a smaller standard deviation than the stress drop estimate itself. The range of event stress drops is 0.2-5 MPa with a geometric mean of 1.6 MPa ± 1.2. It is important to keep in mind that the resonances and high frequency cut-offs we observe could be causing some of the trends we observe in regard to stress drop with depth, M_w, and distance from point of injection because high frequencies are preferentially removed. To address this we only calculate results from the shallowest stations (i.e., stations 1-15), where the effects of resonances and high frequency cut-offs are reduced.

Our absolute estimates of stress drop are very similar to the closest and most similar study (at a pad ~240 km from the pad in this study) by Yu et al. (2020). Compared with our estimated mean of 1.6 ± 1.2 MPa, Yu et al. (2020) calculate an average stress drop of ~1 MPa from their best results of proximal seismic events using the spectral ratio method. Proximal events are mostly confined to the sedimentary layer in Yu et al. (2020), whereas most events in this study occur in the underlying crystalline formation. The similarity of stress drops (both using a Madariaga constant) between our study and Yu et al. (2020) at similar depths and both induced by hydraulic fracturing strongly suggests that the rupture slip to length-scale ratio of seismic events in these two datasets is similar.

We use borehole geophones in comparison to the surface array used by Yu et al. (2020). Using a relatively simple fitting procedure we are able to obtain similar stress drops to the values obtained by Yu et al. (2020). While it is certainly likely that our absolute estimates are smaller than actual values, because of the effects of high frequency attenuation, it is encouraging to see that a borehole array can produce similar results to the closest study, which uses a more sophisticated spectral ratio method. The spectral ratio method practically takes more time compared to directly fitting source models. Thus, this study shows that once a crustal attenuation model is constrained, directly fitting source models from a borehole geophone array may provide decent first order estimates.

Although stress drop estimates in this study are within the expected tectonic range, the average stress drop is below the global average of 4 MPa and lower than the average of 7.5 MPa calculated by Holmgren et al. (2019) from an induced seismicity dataset in the WCSB. Our average stress drop is also lower than the stress drops between ~2-200 MPa, calculated for a tectonic dataset that Onwuemeka et al. (2018) calculated in the Eastern Canadian seismic zone. In both these studies some stress drop estimates are greater than 100 MPa, considerably larger than any of the estimates in this study.

Our lower mean stress drop can be explained by several physical causes. Firstly, a lower effective stress may reduce the stress drop (Allmann et al., 2011). Secondly, the shallower depth of our events compared to Holmgren et al. (2019) and Onwuemeka et al. (2018) will result in a lower crustal shear strength which could result in lower stress drops.

The lowest stress drops we might expect for seismic events at the average depth in this study (2.2 km) can be calculated if we assume a relatively simple, but realistic (Moos and Zoback, 1990) 2D Mohr Coulomb representation of the fault plane, where seismic events are hosted on a strike-slip fault. A strike slip mechanism is expected according to stress gradients recorded from borehole breakouts measurements in the region (Bell, 2015) and the world stress map (Heidbach et al., 2007). Focal mechanisms studies have also found a dominantly strike-slip mechanism in the region (Wang et al., 2018). If we assume the co-efficient of friction along the fault plane is 0.6 and that the fault is critically stressed, we can estimate the shear strength using (Huang et al., 2017)

$$S_{ss} = 0.7(\sigma_v - P), \tag{2.12}$$

where S_{ss} is crustal shear strength, σ_v is vertical stress and P is pore pressure. Assuming a hydrostatic pore pressure of 27 ± 7 MPa and a vertical stress of 66 ± 6 MPa (Kettlety et al., 2019), using stress measurements at depth by Bell (2015), we calculate an available crustal shear strength of 39 MPa ± 9. Based on empirical observations of stress drops from faults in the north and central United States by Huang et al. (2017), we expect a minimum of ~5% of the shear stress to be released (Huang et al., 2017), which results in a minimum stress drop of 1.4 MPa ± 0.5. Therefore the average stress drop (1.6 ± 1.2 MPa) we determine at the depth of the fault zone falls within the expected range for optimally aligned fractures for strike-slip faults. The lower crustal shear strength results in less available shear stress which could explain why our stress drop estimates are lower compared to Onwuemeka et al. (2018), who measure stress drops in the range of ~2-200 MPa for seismic events as deep as the boundary of the seismogenic zone, and Holmgren et al. (2019), who measure an average stress drop of 7.5 MPa at ~4 km depth. If the fault plane is not aligned favourably with regional stresses then our average stress drop estimate may be too small to be explained by crustal shear strength alone and will need additional pore-fluid pressure, which can decrease effective stresses (Zoback, 2009), and therefore decrease available crustal shear strength.

Some studies that analyse seismic datasets where additional pore-fluid is injected into the subsurface report a growing stress drop with distance (e.g., Allmann et al., 2011; Kwiatek et al., 2014) from the injection point or a lower stress drop proximal to the injection point compared to events farther away (Pearson, 1981; Lengliné et al., 2014; Yu et al., 2020), although others (e.g., Clerc et al., 2016; Sumy et al., 2017) could not confirm such trends. Most of our events are between 100-600 m from their points of injection. Within a distance of 10-300 m from the point of injection, Allmann et al. (2011) observe a factor of 5 stress drop increase and Kwiatek et al. (2014) observe an increase from ~1 to ~60 MPa over a distance of ~ 100-500 m. Therefore, given our dataset shows seismicity over similar distance ranges we would expect to see a signal of increasing stress drop with distance. However, we observe no such trend.

When hydraulic fluid is pumped into the subsurface, the rock intactness and permeability will determine how quickly fluid migrates into the rock matrix. The diffusion rate will determine the rate at which the pore pressure front moves away from the injection point, and therefore whether we see a change in crustal shear strength, which some studies show is expressed as an increasing stress drop with distance from the injection point (e.g., Allmann et al., 2011; Kwiatek et al., 2014). One key difference to the Allmann et al. (2011) study is that seismic events analysed here occur within a few hours of each other and are mostly associated with the same stage of injection, compared to a more gradual occurrence of seismicity over several days steadily away from the injection point (Allmann et al., 2011).

Kwiatek et al. (2014) observe an increasing stress drop with distance from the point of injection in seismicity on a reactivated fault. The main difference in this study is that seismicity occurs over the entire distance range in a few hours compared to days. The observation of a growing stress drop with time and distance can be explained by the weaker crustal shear strength proximal to the point of injection relative to stronger crust that is farther away, where the pore pressure is lower. However, in this study, the observation of a constant stress drop over a fault zone hundreds of metres deep in a short time span requires a more abrupt physical mechanism. One explanation could be a better fault connectivity and/or larger permeability along the fault plane (e.g., a more dilated fault), such that fluid can migrate quickly along the fault plane. This makes our observations consistent with this hypothesis of the dependency between stress drop and crustal shear strength when additional pore fluid is added to the subsurface. The physical mechanism of a direct hydraulic connection is supported by Kettlety et al. (2019).

A similar study in both spatial and temporal character to seismicity observed here is the geothermal test carried out by Pearson (1981). They observe an increase in stress drop with distance from the injection point over ~600m and a 6 hour injection time period. Here, the events span a ~7 hour time period, although most events occur in a 3 hour window. Given the similar spatio-temporal character of data in this dataset to Pearson (1981) we expect stress drops to increase with distance from the injection point in this dataset. One reason why we may not observe a stress drop increase could be the permeability difference: the granite at Fenton Hill has low permeability (Pearson, 1981), whereas the Keg-River formation is reported as highly permeable (Adams and Eccles, 2002) and the fractures are likely to extend to the nearest perforation in the overlying shale (Kettlety et al., 2019). Conceptually, the pore-pressure front could have developed quickly over a large distance along the fault in this study, which explains why the initial seismicity which expresses a planar structure just below the shale play and hundreds of metres deeper in the limestone formation, occurs simultaneously (Figure A.3). Once the entire fault has experienced an increase in pore pressure, seismic events happening later will not have a significantly different crustal shear strength, therefore we will not observe a stress drop difference over time or space. Similar observations are made by Sumy et al. (2017) in the case of wastewater injection, where fault planes required relatively little additional stress to fail because of previous injection which had lowered the effective stresses.

2.7 Conclusions

In this study we first highlight the challenges associated with retrieving robust high frequency estimates of source parameters from 112 -0.6 < M_w < 0.7 microseismic events recorded by borehole geophone arrays at a pad within the Horn River basin, British Columbia. Of these events we calculate first order estimates of stress drop from 90 events. Our results show that borehole geophones are prone to high frequency resonances above 250 Hz, which are most likely caused by receiver side instrument effects. Bandwidth limitations, resonances and severe attenuation limit the ability to faithfully retrieve high frequency information and estimate attenuation models. Deeper stations along both borehole arrays are particularly prone to resonances and the effects of high frequency cut-offs.

From our best estimates of P-phase spectra recorded at one of the wells (the K-well), we determine Q_p using two different empirical methods. Q_p = 180 ± 40 appears to provide the most realistic stress drop estimates. We calculate a mean stress drop of 1.6 ± 1.2 MPa, which broadly supports self-similar scaling down to M_w = -0.6. However, our estimates are smaller than other regional induced and tectonic studies, which can be explained by lower effective stresses and/or lower crustal shear strength. It is likely that our estimates represent a lower bound of what are larger estimates because the retrieved corner frequencies may be biased downwards due to high frequency challenges. Finally, we find no statistically significant correlations between stress drop and depth or distance from injection, which could be explained by hydraulic fluid communicating relatively quickly along fractured rock compared to slower diffusion in more intact rock.

CHAPTER 3

TESTING HYPOTHESES OF STRESS DROP VARIATIONS USING SPECTRAL RATIOS

The next chapter builds on results from Chapter 2 using a more sophisticated, spectral ratio approach for calculating stress drops using the same microseismic dataset. The results confirm some inferences of stress drops from Chapter 2 and delve into more intricate observations of stress drop and attenuation. I conducted the analysis, produced all figures and wrote the manuscript. Maximilian Werner and Joanna Holmgren provided edits.

Analyzing high frequency observations within seismic signals (e.g., stress drops) may reveal important information about how faults respond to pore pressure perturbations during subsurface geo-energy operations. Some researchers have linked stress drop to the in-situ stress and pore pressure conditions on a fault - higher pore pressure correlates with lower stress drops; and stress drop should decrease with decreasing differential stress due to repeated failures. However, these observations remain controversial. Here we analyse the spatio-temporal variation of 31 stress drop measurements for seismic events in the -0.55 < M_w < 0.4 range linked to fault reactivation in the Horn River basin, British Columbia. Firstly, we calculate an average stress drop of 4 MPa ± 2 from estimates based on the spectral ratio method, which is twice as large as the average from directly fitting source models. The discrepancy between estimates is likely caused by better treatment of attenuation using spectral ratios. Secondly, corner frequencies (155-352 Hz) are relatively close to a high frequency cut-off (f_{max}) at ~400 Hz which may cause spurious scaling of stress drop with magnitude, even when more sophisticated approaches (i.e., spectral ratios) are used. Thirdly, we do not observe a systematic anti-correlation between stress drop and distance, nor do we observe systematic an anti-correlation of stress drop with time on roughly co-located and highly similar clusters of seismic events. One interpretation for these observations is non-linear pore fluid diffusion along a fault structure which lowers effective stresses over a relatively large scale, but with some variation between individual patches.

3.1 Introduction

During subsurface geo-energy operations fault structures can pose a significant hazard and cause catastrophic human and economic costs (e.g., Ellsworth et al., 2019). To de-risk this hazard there are methods that can be used in real-time, namely the Traffic Light Schemes (TLSs), which can inform which mitigation strategy should be implemented (i.e., when flow should be stopped or reduced), on the basis of threshold breaking magnitudes (Kao et al., 2018; Kim et al., 2018; Ader et al., 2020; Verdon and Bommer, 2021). In the case that event magnitudes steadily increase with increasing additional fluid volume (Kwiatek et al., 2019), TLSs are a useful method, however, in some cases large magnitude jumps may appear suddenly (Kim et al., 2018; Clarke et al., 2019), which make it more difficult to assign a magnitude threshold. Other strategies include simulating earthquake catalogues using Epistemic Type Aftershock Sequences (ETAS) to estimate seismic rates (e.g., Mancini et al., 2021), which can help assess the hazard, on the basis of which mitigation actions can be taken. Whilst ETAS and TLSs are useful ways of informing what mitigation tactic should be used, they do not reveal much information about how the fluid interacts with faults, where stress changes are occurring and the mechanism of failure on faults.

Stress drop (the ratio of slip to rupture area) enables us to better understand the potential link between geomechanics and rupture mechanics (e.g., Pearson, 1981; Allmann et al., 2011; Lengliné et al., 2014). To calculate stress drops we can directly fit attenuation-corrected models of the source spectral shape to the far-field P- and S- spectra. However, directly fitting source models can suffer from the assumption of a modelled attenuation term which has been shown to underestimate source parameters (Ide et al., 2003; Yu et al., 2020). The spectral ratio method (e.g., Mueller, 1985; Ide et al., 2003; Kwiatek et al., 2014; Lengliné et al., 2014; Holmgren et al., 2019; Shearer et al., 2019; Yu et al., 2020) exploits the similarity of smaller earthquakes within a large enough catalogue to empirically remove the effect of attenuation on phase arrival spectra from larger earthquakes. The relatively smaller earthquakes that are both highly cross-correlated and co-located with larger earthquakes can approximate a delta function (Mueller, 1985). The larger earthquake spectrum is divided by the smaller earthquake spectrum (i.e., deconvolution) and models of the earthquake rupture (Brune, 1970; Madariaga, 1976) can then be fitted to the empirically corrected spectra to calculate source radii and stress drops.

The spectral ratio method has proved to be useful, especially for small earthquakes (Abercrombie, 2021). However, for microseismic asperities, the bandwidth limitations placed on signals can become severe (Deichmann, 2017) and it is particularly difficult to obtain high quality recordings of the smaller earthquakes (i.e., $M_w < 0$). High frequency corrections can be applied to spectra (e.g., Butcher et al., 2020) but the physical nature of high frequency cut-offs remains unclear (Ktenidou et al., 2014).

Many studies have used spectral ratios and direct fitting of source models to calculate stress drops (e.g., Abercrombie, 1995; Ide et al., 2003; Allmann et al., 2011; Yu et al., 2020; Klinger and Werner, 2022). Some studies have observed an empirical increase of stress drop with distance from the point of injection which is interpreted to result from smaller differential stresses (i.e., smaller confining pressure) nearer to the point of injection (e.g., Pearson, 1981; Allmann et al., 2011). The proposed conceptual model is that if additional pore fluid is injected into the rock mass, effective normal stresses are reduced towards Mohr Coloumb frictional failure - at which point shear stress drops and differential stress decreases. If pore pressures again subsequently reduce effective normal stresses to failure then the lower shear strength of the fracture interface could correspond to a signal of lower stress drops nearer to the point of injection relative to more distal stress drop measurements (Zoback, 2009).

Stress drop measurements, and therefore further inferences about geomechanics, are sensitive to perturbances to waveforms which arise along the ray path and around the site (i.e., geological conditions near or at the geophone, and potential resonances inside the geophone (Klinger and Werner, 2022). The combined effects of path and site can be described using spectra corrected for the source (i.e., source corrected spectra). The spectral ratio method better accounts for path and site effects and tends to result in higher stress drop estimates compared to directly fitting source models (Ide et al., 2003; Viegas et al., 2010; Yu et al., 2020).

Many factors can affect the stress drop on a fault patch. Aside from the parameters implicit in source models such as that proposed by Brune (1970) (i.e., seismic moment, rupture velocity and type of crack model), other factors which have shown to empirically correlate with stress drop include depth (e.g., Goebel et al., 2015; Trugman, 2020), frictional strength (e.g., Yoshida et al., 2017), faulting style (e.g., Huang et al., 2017) and fault zone damage (e.g., Moyer et al., 2018). Within smaller scale geological environments stress drop variations have been linked to the addition of pore fluids (e.g., Allmann et al., 2011; Lengliné et al., 2014).

In this study we use the spectral ratio method to determine stress drops of seismic events linked to reactivation of a fault zone during hydraulic fracturing operations. We build on the study by Klinger and Werner (2022), who used direct fits to calculate stress drops with the same dataset and many of the same events used here. Our new, higher quality stress drops are larger than those calculated by Klinger and Werner (2022) and we explore the reason for this difference. We then test hypotheses about how pore pressure might impact stress drops from the point of injection and within approximately co-located events.

3.2 Data

3.2.1 Horn River basin dataset

We use data collected during hydraulic fracturing treatment in the Horn River basin

(Canada), which targeted three organic-rich shale gas units. The dataset is described by Baird et al. (2017), Verdon and Budge (2018), Kettlety et al. (2019) and Klinger and Werner (2022). The contractor provided us with seismic data recorded between July-August 2013 from three downhole borehole geophone arrays. From the arrays that provide recordings (K-well and S-well), there are 36 15-Hz geophones sampling at 4000 Hz. The catalogue of more than 90,000 $-3 < M_w < 0.5$ seismic events (Figure 3.1a) also contains stress drops, moment tensor inversions and fault radii for 35 % of the events (e.g., Baird et al., 2017; Kettlety et al., 2019). We are also provided with drilling data which includes bottom hole pressures, down hole pressures and sand concentrations. For details about velocity model and locations see Klinger and Werner (2022).

Most of the induced seismicity occurs in the shale play, which appears as a diffuse cloud (Figure 3.1a). Beneath the shale play the crystalline basement rock also hosts seismic events where two fault planes are identified by Kettlety et al. (2019). We analyse seismicity linked to one of these fault planes which shows the clearest structure (Figure 3.1a). The requirements of the spectral ratio method limits the events we can consider as candidate targets. Of the events, we select a subset as final target events that pass (Section 3.3.4). Most target events occur along the fault plane, which is reactivated following injection at stage A14 (Figure 3.1b), underlying the shale play (Figure 3.1c).

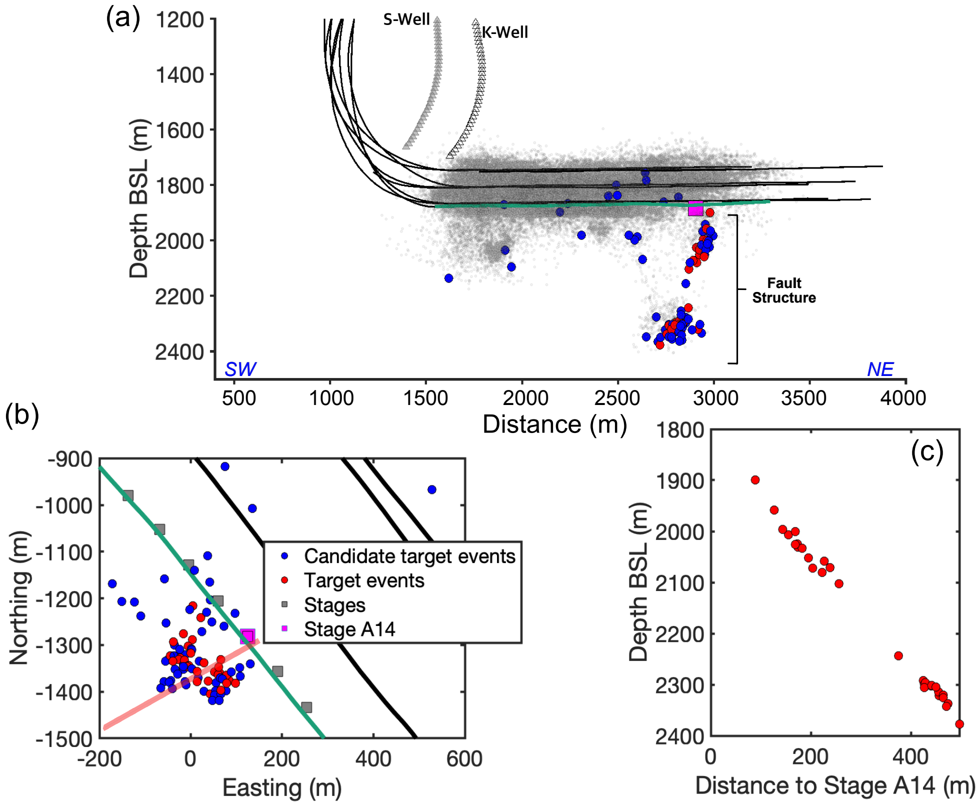

Figure 3.1: Cross sectional and map views of induced seismicity at a pad within the Horn River basin. (a) Toe-heel, multi-well hydraulic fracturing operation showing the cloud of 90,000+ induced seismic events (Baird et al., 2017). Candidate target events denoted by blue circles (103 events) and final target events shown as red circles (32 events). Triangles show the borehole geophone arrays. (b) Map view of candidate and final target events. Stages shown as grey squares. Most target events occur during stimulation of stage A14, shown as a magenta square. The red thick line shows the line used for the cross section in (a). (c) Depth against distance to stage A14 of final target events.

3.3 Methods

3.3.1 Spectral ratio method

To estimate stress drop we calculate the source spectrum of a seismic event using a phase arrival spectrum. The instrument-corrected spectrum can be expressed as a combination of path, receiver and source effects by (Shearer, 2009):

$$U(f) = S(f) \times A(f) \times R(f), \tag{3.1}$$

where U is the instrument-corrected signal, S is the source, A is path and R is the receiver term as a function of frequency (f).

Often we are interested in recovering S to calculate source parameters such as stress drop and corner frequency. Several authors have analytically determined an expression for the source term (e.g., Sato and Hirasawa, 1973; Madariaga, 1976; Kaneko and Shearer, 2014). One of the most widely used models is that of Brune (1970), which models the rupture as a circular dislocation, causing shear wave propagation. Here we model the far-field spectra from analytical solutions by Aki (1967) and Brune (1970):

$$U(f) = \frac{\Omega_o e^{\frac{-\pi f t}{Q}}}{[(1+\frac{f}{f_c})^{n\gamma}]^{\frac{1}{\gamma}}}, \tag{3.2}$$

where U is the far-field displacement source spectrum, Ω_o is the low frequency plateau linked to a seismic event, t is the travel time of the dominant phase arrival, n describes the high frequency decay, γ determines the sharpness of transition from the low frequency plateau to the high frequency fall-off and f_c is the corner frequency. The quality factor (Q) describes the inverse of the loss of energy per cycle. While there is some debate about the value of n, most studies use n = 2 (e.g., Anderson and Hough, 1984; Abercrombie and Leary, 1993; Prieto et al., 2004; Kwiatek et al., 2011; Abercrombie, 2015).

When fitting equation (3.2) to data, Ω_o can usually be well constrained but Q trades off with f_c, which can result in unstable Q estimates (e.g., Ide et al., 2003). To empirically account for these effects we use the spectral ratio method whereby highly similar and co-located events that are recorded by the same station will share common features and similar focal mechanisms. We can assume that these small events approximate delta functions, and use them to remove the effect of the path and site using division in the frequency domain. The larger event is the target event and the smaller event is the empirical Green's function (EGF). The spectral ratio of the target and EGF is

$$\frac{U_T(f)}{U_{EGF}(f)} = \frac{\Omega_{o,T}}{\Omega_{o,EGF}} \frac{[(1+\frac{f}{f_{c,EGF}})^4]^{\frac{1}{2}}}{[(1+\frac{f}{f_{c,T}})^4]^{\frac{1}{2}}}, \tag{3.3}$$

where subscript T and EGF correspond to the target earthquake and the EGF, respectively. We then directly fit equation (3.3) to the observed spectral ratio. We use a Boatwright model (Boatwright, 1978) as it appears to provide a better visual fit and fix $f_c,_{EGF}$ (Abercrombie, 2015; Shearer et al., 2019). This leaves $\Omega_o,_T/\Omega_{o,EGF}$ and $f_c,_T$ as the only free parameters, which we find by optimising the fit of equation (3.3) to the spectral ratios using @fminsrchbnd in MATLAB.

3.3.2 Calculating empirical path and site terms

By comparing Q estimates derived from empirically corrected spectra here with Q estimates from direct fits (Klinger and Werner, 2022), we can better understand differences in source parameter estimates between the two methods. To retrieve the path and site terms and provide estimates of Q, we denconvolve *U(f)* with the source spectrum, *S(f)*, leaving the source corrected spectrum *SC(f)*. We apply this correction for all stations that pass the criterion used for spectral ratios, which contain the combined path and site terms, via

$$SC(f) = \frac{U(f)}{S(f)}. \tag{3.4}$$

Each *SC(f)* is normalised to the first frequency point to look at relative variations in the frequency spectrum rather than comparing them in an absolute manner.

We then calculate the anelastic attenuation constant Q. We assume frequency independent, intrinsic attenuation is the dominant mechanism of amplitude reduction (e.g., Abercrombie, 1998) and find the best fitting Q using

$$A(f) = A_o(f)e^{\frac{-\pi f t}{Q(f)}}, \tag{3.5}$$

where *A(f)* is the displacement amplitude spectrum some distance from the source. A_o is the amplitude at the source, or at a position closer to the source than where *A(f)* is measured, f is frequency and t is travel time between the positions where A and A_o are measured. If we assume $SC(f) = A(f)/A_o(f)$ we can estimate Q that best explains the data. For details about travel time calculation we refer the reader to Klinger and Werner (2022).

3.3.3 M_w calculation

For the stress drops we report in Section 3.4.1, 26 events were previously analysed by Klinger and Werner (2022). We use their moment and M_w estimates. For the other 6 events, we calculate estimates using the same method. Klinger and Werner (2022) discuss differences between their and the contractor's M_w estimates. We use contractor magnitude estimates when determining the initial candidate target events in section 3.3.4. After the processing stage we recalculate all target magnitudes and moments using our own estimates. From here on contractor magnitudes are denoted as $M_{w,c}$ and our magnitudes are M_w.

3.3.4 EGF method processing and stress drop calculation

We consider 103 candidate target events > $M_{w,c}$ -0.3. Any event that is at least 0.3 M_w units smaller than the target M_w (Clerc et al., 2016) and within 100 m of the target is considered a potential EGF. To pick potential EGFs, we cross-correlate each target phase arrival with each potential EGF, along all stations of the K-well and S-well. We experiment with a range of window sizes and find that a shorter window size (i.e., 0.06 s) that captures just the first phase arrival of the target event is optimal for finding a good EGF pick. Hereafter, we only use phase arrivals that are highly cross-correlated (i.e., CC > 0.8). To control the quality of picks, we additionally require the standard deviation of the arrival times of one event at all stations to be less than 0.1 because this implies consistent picks across these closely spaced stations which are separated by 15 m. At the K-well, 43 of the initial 103 candidate target events record coherent picks for at least one potential EGF. The S-well recorded 42 target events with at least one EGF with robust picks across all stations.

We filter each target event between 60-300 Hz using a 2-pole, 2-pass Butterworth filter during picking and cross correlation. This removes high frequency noise and makes the dominant signal for events in this magnitude range clearer than using the full bandwidth, thereby improving pick quality. After picks are established, we revert to the raw unfiltered signal for further analysis. We rotate the time-series into the rayframe that maximises particle motion in the radial direction for the P-phase, and the transverse direction for S-phases. For each target time-series we select a 0.06 s window around both phase arrivals and apply a cosine taper to the data, which we use as a template for picking potential EGFs.

Once picks for the target and potential EGFs are established, we calculate the displacement-amplitude spectra of both phase arrivals and pre-event noise using the multi-taper method (Prieto et al., 2007) with a 0.12 s time window (Figure 3.2a and b). We use a longer time window here to ensure the full phase arrival is captured considering the S-P times, and to increase frequency resolution. The displacement amplitude spectra show bumps at low frequency (i.e., between 15-40 Hz), which we interpret as instrument effects (Klinger and Werner, 2022). For this reason we restrict the spectral ratios to frequencies > 40 Hz up to the signal-to-noise ratio (SNR) limit (Figure 3.2c).

Next, we compare the waveform similarity of the full EGF phase arrival to the target event. We use a threshold of CC > 0.8, as recommended as a lower limit by Abercrombie (2015), and used in other induced seismicity studies (e.g., Holmgren et al., 2019). We then calculate the spectra of the target, EGF and their respective pre-event noise in log-space. Using these spectra we establish the frequency range over which the SNR is > 3 in the target and EGF, and only consider target-EGF pairs where there is a minimum bandwidth of 30 Hz that meets this criterion, as shown in Figure 3.2b. For comparison, Holmgren et al. (2019) require a minimum bandwidth of 10 Hz. Using target-EGF spectral pairs we then calculate the spectral ratio (Figure 3.2c) and check the M_w difference. We require a 0.5 M_w difference, which corresponds to a factor of 5.6 in seismic moment. To ensure good spectral shape we also require that the ratio between the low and high frequency part of each spectral ratio has a ratio of greater than three (Ruhl et al., 2017).

We constrain the EGF corner frequency, as this can reduce biases in the target corner frequency (Shearer et al., 2019). The average $M_{w,c}$ as calculated by the contractor for all EGFs across all targets is $M_{w,c}$ = -0.7 ± 0.2 (± 1σ standard error). Using the following equation by Hanks and Kanamori (1979)

$$M_w = \frac{2}{3}(\log_{10} M_o - 9.1), \tag{3.6}$$

we calculate the corresponding average seismic moment and the corner frequency for a 1 MPa and 10 MPa stress drop using equations (3.8) and (3.9) below, which are 300 and 700 Hz, respectively. From visual inspection of single station fits, 700 Hz appears to explain the spectral ratio data better, which we use to constrain the EGF corner frequency.

We optimize the fit of equation (3.3) to find $f_{c,T}$ and $\Omega_{o,T}/\Omega_{o,EGF}$ which best explains the data using @fminsearchbnd in MATLAB. A Boatwright model appears to provide a better visual fit to the data compared to a Brune model as the onset to the high frequency decay is sharper than what the Brune model estimates. Other studies in the Western Canadian Sedimentary basin that analyse induced seismicity (e.g., Holmgren et al., 2019) also prefer a Boatwright model.

Once $f_{c,T}$ is calculated we can determine the uncertainty in $f_{c,T}$ using the method by Viegas et al. (2010). We perform a search over ± 0.5 $f_{c,T}$ with $\Omega_{o,T}/\Omega_{o,EGF}$ as the only free parameter. For each iteration of $f_{c,T}$ we calculate the sum of residuals squared between data and model. Then we normalize each value to the sum of residuals from the initial $f_{c,T}$. For individual spectral ratios, if the normalized variance at $f_{c,T} \pm 0.5 f_{c,T}$ is more than or equal to 1.05 (Figure 3.2d) (e.g., Holmgren et al., 2019), we pass the target-EGF pair, as this suggest the variance is constrained within an acceptable narrow range of values; if the normalised variance does not exceed 1.05 at $\pm\, 0.5 f_{c,T}$ the range of values is much larger.

Despite these tests, some spectral ratios that qualify still show poor spectral shapes (i.e., bumps), which might be caused by the low SNR of relatively small M_w events, as also observed by Klinger and Werner (2022), and/or path terms that are not exactly the same for the EGF and target. Therefore, as a last test, we determine how closely the signal resembles equation (3.3) by calculating the sum of residuals squared at each frequency point in log 10 space (i.e., L2 norm in log-space). This test disqualifies spectral ratios with significant bumps. From visual inspection we impose L2 < 0.15.

We then stack all spectral ratios for each target event (Figure 3.3). We first normalize the signal to $\Omega_{o,T}/\Omega_{o,EGF}$. In doing so, the signals of many individual spectral ratios appears more stable. Then, for each target we calculate the geometrical mean of the normalized spectral ratio at each frequency point over all spectral ratios for a given target event. To ensure that the mean signal is stable, we require that at least five spectral ratios are recorded for a given frequency point. Using the stacked signal, we then recalculate the target corner frequency and the uncertainty using the same method as for individual spectral ratios but to reflect realistic stress drop uncertainties we use ± 30% rather than ± 5% of the normalized cost function as the uncertainty (inset of Figure 3.3). Stress drop uncertainty is then determined using standard error propagation (Fornasini, 2008) of the corner frequency in equation (3.7).

The stacked target corner frequency is sensitive to the chosen EGF corner frequency. A 700 Hz EGF corner frequency on an example event (event ID: 20130723122808) results in a stacked target corner frequency of 160 Hz but if we choose 600-800 Hz as the EGF corner frequency range, the corresponding stacked target corner frequency has a sensitivity of 10 Hz. As the stacked target corner frequency is cubed in equation (3.9), a 10 Hz increase corresponds to a stress drop that is a factor of 1.2 larger. Considering the implicitly large uncertainties of stress drop, an 100 Hz sensitivity of EGF corner frequency is unlikely to introduce significant uncertainty into stress drops.

Once $f_{c,T}$ is determined from the stacked signal we calculate the rupture radius using

$$r = \frac{k\beta}{f_c}, \tag{3.7}$$

where f_c is the corner frequency, k is a constant relating f_c to the rupture dimensions assuming a specific source model, β is shear wave velocity at the seismic source and r is source radius. For P-phase arrivals, k = 0.32 using a Madariaga model. The Brune model constants are ~ 2 larger which results in stress drop estimates that are ~ 5.5 smaller. By relating the corner frequency of each target spectrum to rupture radius, we can now calculate the stress drop (Eshelby, 1957)

$$\Delta\sigma = \frac{7M_o}{16r^3}, \tag{3.8}$$

where M_0 is the seismic moment, or we can combine equations (3.7) and (3.8) to obtain

$$\Delta\sigma = \frac{7M_0}{16}\left(\frac{f_c}{\kappa\beta}\right)^3. \tag{3.9}$$

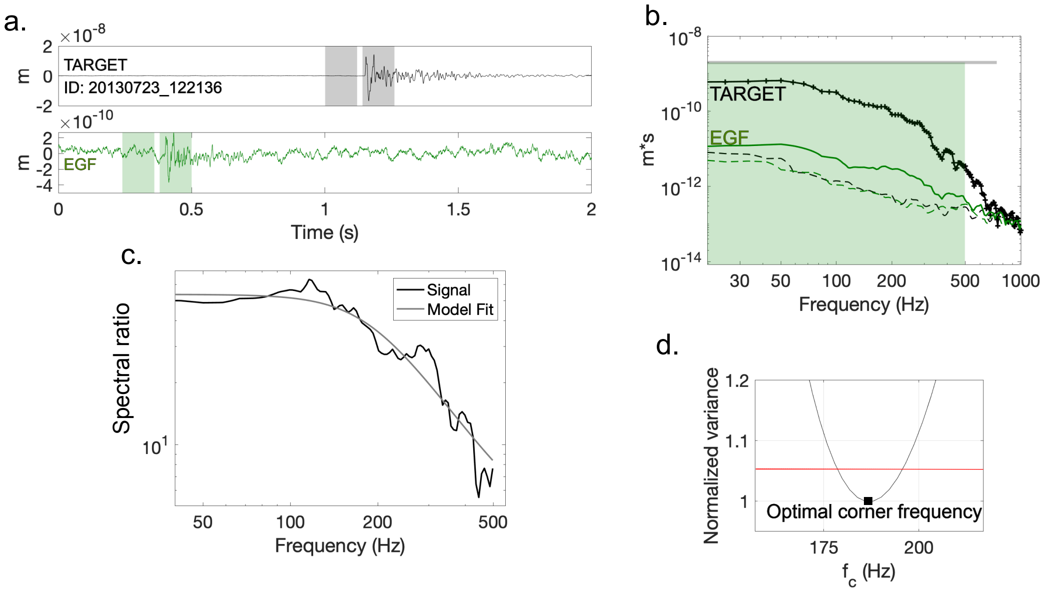

Figure 3.2: Processing steps outlined for a target-EGF pair that passes qualifying criteria. (a) Displacement time-series from the radial component of the target (black line) and the EGF (green line). Black and green shaded areas show the windows used for the phase arrival/noise of the target and EGF, respectively. (b) Displacement spectra of the target (black solid line), empirical Green's function (green solid line), target pre-event noise (black dashed line), EGF pre-event noise (green dashed line). Green shaded area shows EGF SNR > 3; grey bar shows target SNR > 3 . (c) Spectral ratio with a Boatwright model fit (grey solid line). (d) Cost function between model and data normalized to cost function value using $f_{c,T}$. The corner frequency converges towards a minimum in an appropriately narrow bandwidth below the normalized variance limit, shown by the red line.

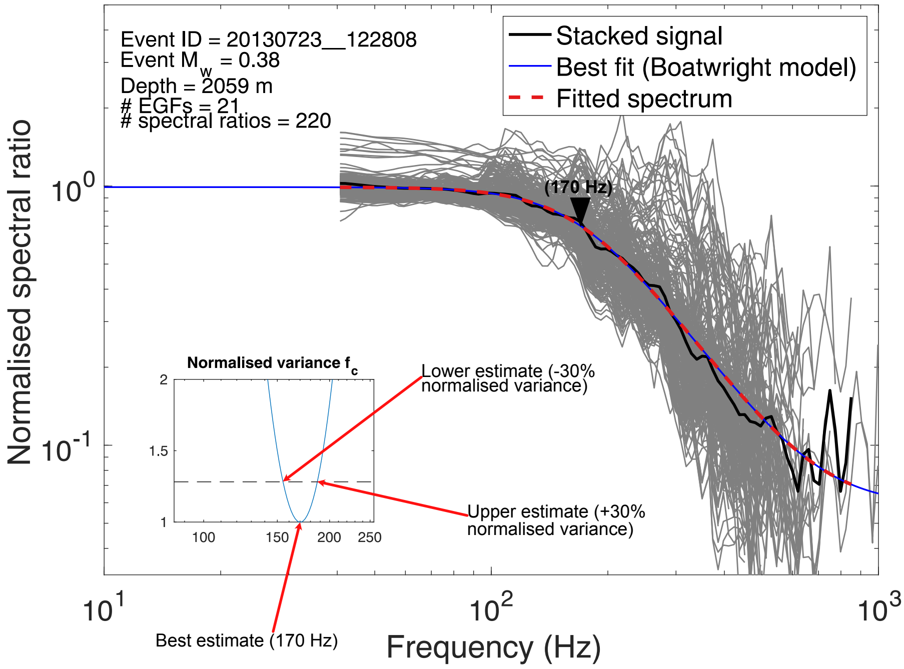

Figure 3.3: An example of normalised spectral ratios and the model fit for an event which passes all processing criteria. Grey lines denote individual normalised spectral ratios. The black thick line shows the stacked signal using all spectral ratios. Blue solid line denotes a Boatwright model fit. Red dashed line shows fit within the recorded frequency range. Black triangle shows the best fitting corner frequency. Inset plot shows normalised variance of a stacked corner frequency with labels indicating the maximum and minimum values used for the uncertainty.

3.3.5 Cross-correlation

We can test hypotheses about how we expect stress drop to vary on fault patches that repeatedly slip by identifying highly cross-correlated events in the same location and classifying events into families of similar waveform characteristics. However, it is difficult to faithfully monitor exactly the same asperity within the M_w range we are analysing. The largest rupture we might expect for a M_w 0, 1 MPa stress drop event is ~8 m. Given that these ruptures are significantly smaller than the relative location uncertainty of ± 50 m (Kettlety et al., 2019) we can only call seismic events which fit the cross-correlation criterion as approximately co-located events (ACEs).

For each of the 43 events that show robust picks we first average the velocity-time waveform from the two transverse components using a 0.3 s time window around the S-phases (S-phases allow us to use longer time windows compared to P-phases because the coda is not contaminated by a different phase). Then we taper the signal and filter the velocity-time series between 20-1000 Hz.

We cross correlate all events with each other to obtain a cross-correlation matrix. For an event to qualify as part of a family of highly cross-correlated events, it must display a cross-correlation coefficient > 0.8 with at least 10 other events. Visually, we then group the events which highlight the same highly cross-correlated matrix cells (a family of events). To identify ACEs we combine the cross correlation matrix and an inter-event distance matrix (d_{ij}). We prescribe a minimum threshold of CC > 0.8 (e.g., Nadeau and McEvitty, 2004) and an inter-event distance of < 50 m.

3.4 Results

3.4.1 Source parameters

We obtain corner frequencies and stress drops of 32 target events with the Boatwright model. For stress drop estimates we only use events with a standard deviation that is smaller than the stress drop estimate itself, leaving 31 events. Most seismic events lie between the 1 and 10 MPa stress drop lines assuming a constant rupture velocity corresponding to the Keg-River limestone formation of 3800 ms^{-1} (Figure 3.4a). The geometrical mean corner frequency across events is 250 Hz ± 20 (where ± 20 denotes the geometrical standard deviation), which corresponds to a rupture radius of 5 m ± 1 m assuming a Madariaga source model. These rupture radii are slightly smaller than 6 m ± 2 m from direct fits (Klinger and Werner, 2021), although within the uncertainty (Figure 3.4a).

We calculate an average stress drop of 4 MPa ± 2 MPa, which is identical to the global average of 4 MPa calculated by Allmann and Shearer (2009). Across the M_w range stress drop increases with a gradient of 0.6 ± 0.1 (Figure 3.4b). To estimate the uncertainty in the line of best fit we generate a random sample of 1000 stress drop measurements corresponding to the Gaussian distribution using the 1σ uncertainty for each event. Then we bootstrap from the distribution of each event to create 1000 synthetic stress drop sub-catalogues and calculate the line of best fit in each case.

We next assess if stress drop increases from the injection point (e.g., Allmann et al., 2011) but find no convincing evidence of such a trend. Spatially, there are two clusters of seismicity linked to the fault structure (Figure 3.1a), and both show similar stress drop estimates. Visually, one might argue for an increase in stress drop from the closest event within the patch of seismicity between 100-300 m from the point of injection (Figure 3.4c). However, we observe significant variability in stress drop estimates. Additionally, the closest event is the second smallest M_w event (Figure 3.4b) and the scaling of stress drops with M_w causes a lower than expected stress drop. Stress drops do not vary with distance from the point of injection as the line of best fit gradient is ~0, (Figure 3.4c), which agrees with observations using direct fits by Klinger and

Werner (2022).

Compared to direct estimates of stress drop, all but two spectral ratio estimates show larger stress drops (Figure 3.5). Direct estimates of the same events have an average stress drop of 2 MPa, which is 50 % smaller than spectral ratio estimates when taking the ratios of the geometrical mean between spectral ratio and direct estimates. 14 estimates using the spectral ratio method show clearly larger stress drops, 7 estimates are larger than direct fits but within the uncertainties and 2 spectral ratio estimates are smaller than direct estimates but within the uncertainties (Figure 3.5).

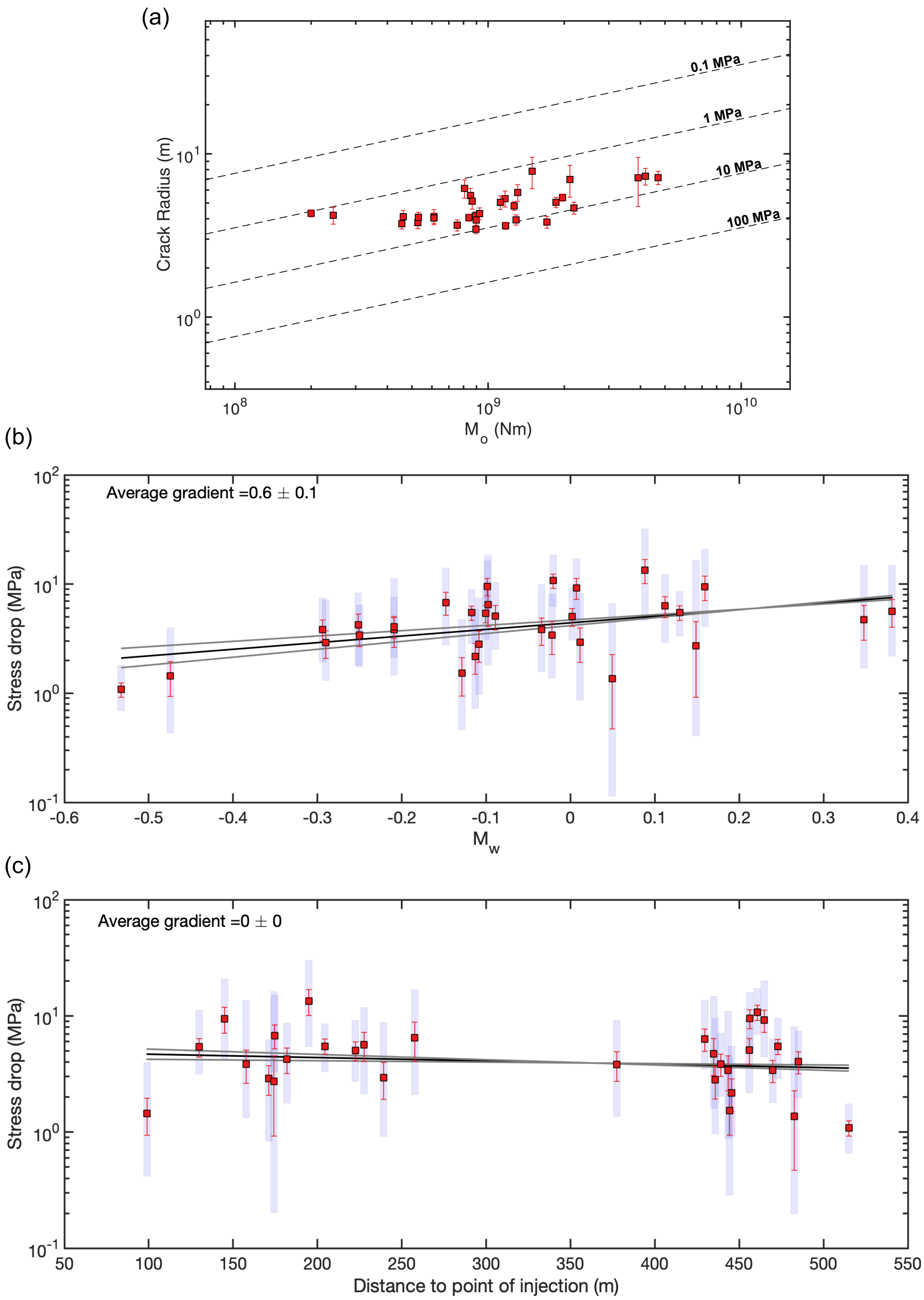

Figure 3.4: (a and b) Scaling of source parameters and (c) how these change with distance from injection point. (a) Crack radius vs seismic moment estimates from 32 target events that pass processing criteria, assuming a Madariaga source model. (b) Stress drop against M_w and (c) stress drop against distance to injection point. Red error bars represent 1σ uncertainty and blue bars show Gaussian distribution of stress drops. In (b) and (c) the black line shows the average line of best fit. The two grey lines show the 2σ uncertainty.

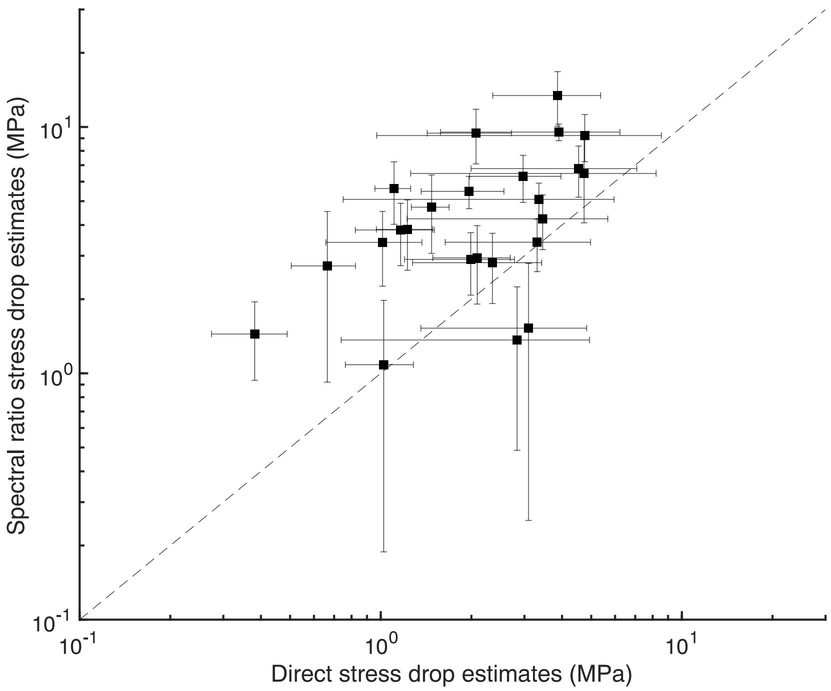

Figure 3.5: Comparison of stress drop estimates from the spectral ratio method with direct spectral fits fitting results by Klinger and Werner (2022). Dashed line denotes a 1:1 line.

3.4.2 Attenuation analysis

We bin *SC(f)* by distance between event and station because there are systematic differences in source corrected spectra along the stations. Deeper stations (corresponding to closer distance bins) are enriched in high frequency energy (i.e., >250 Hz) compared to shallower stations (Figure 3.6). We also limit fitting of Q up to 400 Hz because of high frequency cut-offs. Direct fit estimates of Q are only available from observations at the K-well (Klinger and Werner, 2022), therefore for comparison we limit this attenuation analysis to the K-well.

The source corrected spectra reveal information about the path (Figure 3.6). A frequency independent model appears to explain the data well up to ~250 Hz (Figure 3.6). Above ~250 Hz, the model systematically underestimates the data in the 1000-1325 m distance bins. There is also a clear transition to a steep fall-off in spectral energy at ~400 Hz for all distance bins, but the change is most severe in the closest distance bins (i.e., deepest stations closer to the seismic events). This steep fall off is a high frequency cut-off (i.e., f_{max}) which is most likely because of the high frequency filters that apply to microseismicity in this frequency range (Deichmann, 2017). The spectral ratio method appears to account for this cut-off as spectral energy is larger above 400 Hz using spectral ratios (blue dashed line in Figure 3.7) compared to the direct fits (black and grey solid lines in Figure 3.7). In the more distant 1325-1450 m bins (i.e., shallower stations), the frequency-independent attenuation model provides a better visual fit to the data (Figure 3.6).

The Q estimates we calculate here are lower than the estimate provided by Klinger and Werner (2022). Compared to the constant Q = 180 used by (Klinger and Werner, 2022) for direct estimates of stress drops, a lower average Q in the range of Q = 94-121 is more consistent with spectral ratios. This is exemplified in Figure 3.7 where we show that Q = 180 (black line) underestimates the spectral ratio (blue dashed line) compared to using Q = 94 and Q = 121 (grey solid lines). The effect of a lower Q is that corner frequency and stress drop estimates for spectral ratios are larger than direct estimates (Figure 3.7), which explains the discrepancies that lie above the 1:1 line in Figure 3.5.

The reason for the discrepancy of Q between Chapters 2 and 3 may be because empirical determination of the path term accounts for all forms of attenuation (including site effects and geometrical spreading), whereas, in Chapter 2, we assume intrinsic attenuation is the dominant mechanism of attenuation. As shown in Figure 3.6, a high frequency cut-off (most likely a site effect) clearly affects the spectra which is not modelled for in Chapter 2.

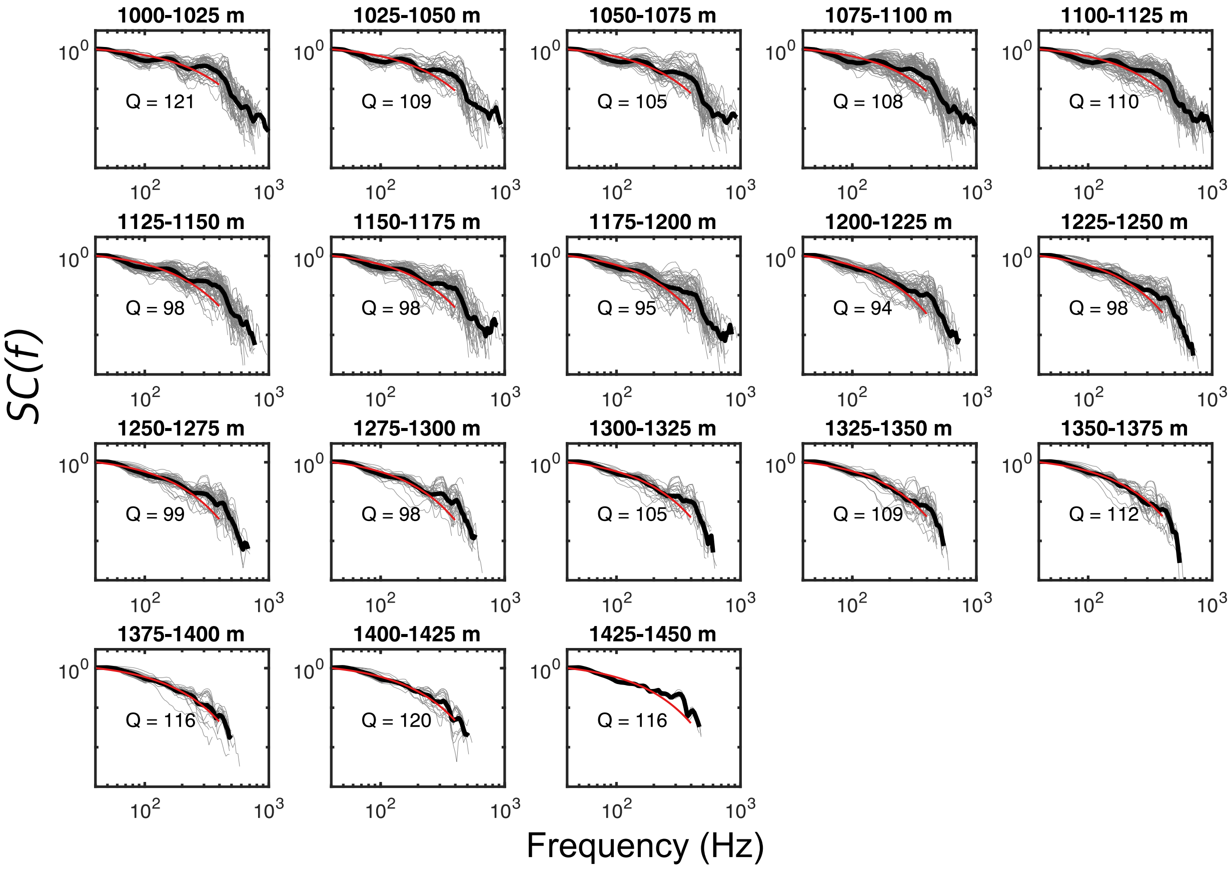

Figure 3.6: Source corrected spectra binned by distance from event to station at the K-well. Lower distances correspond to deeper stations which are closer to the seismic events (Figure 4.1). Each grey line shows a path corrected spectrum and the thick black line shows the stacked signal. Red line denotes the best fitting Q, as labelled.

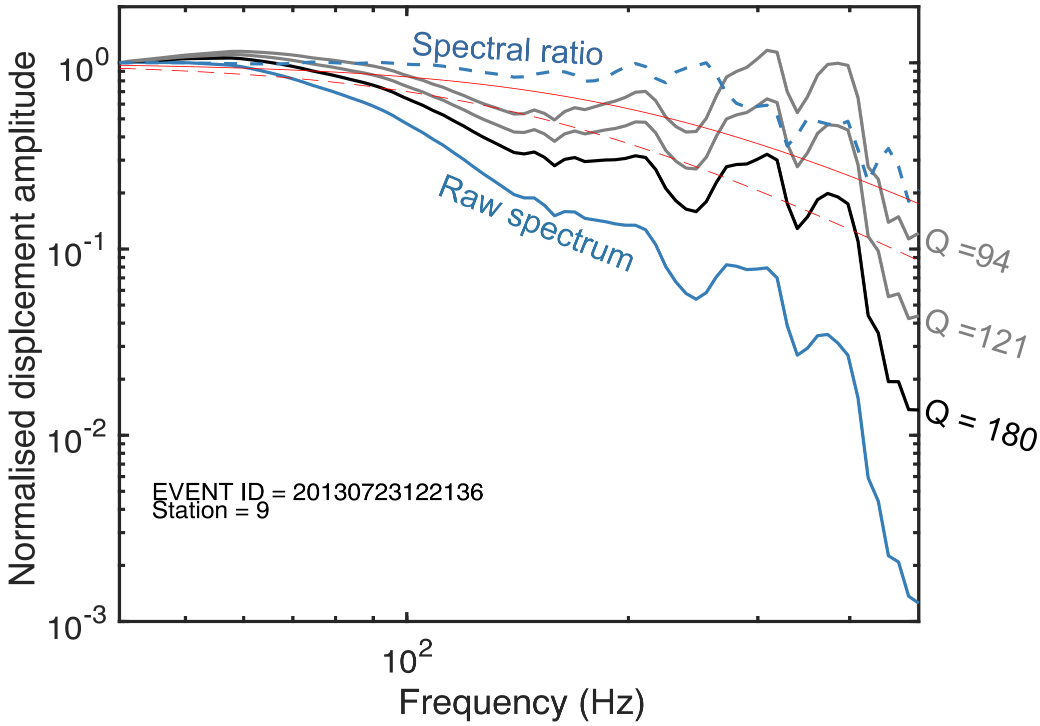

Figure 3.7: Normalised displacement spectra with different path corrections for an event recorded at the K-Well. The black line is a path-corrected (i.e., corrected for path effects) spectrum for Q=180, as established from direct fits (Klinger and Werner, 2022). Grey lines are path-corrected spectra using Q = 94 and 121 in this study. The blue line is the normalised single spectral ratio. The red dashed line shows a source model fit using Q=180 and the solid red line denotes a source model fit to the spectral ratio, where attenuation is empirically accounted for.

3.4.3 Cross-correlation matrix analysis

We identify two families of events (Figure 3.8). The first 10 events are highly cross-correlated with each other, and there are a further 10 events that also show high similarity with these 10 events (Figure 3.8a). We classify these 20 events as Family 1 (Figure 3.8b). Another group of events are highly cross correlated with each other, which we classify as Family 2 (Figure 3.8b). Contrary to expectation, these families are not spatially distinct and therefore do not delineate two different fault patches (Figure 3.9a). The reason for the difference in waveform similarity between the two families is unclear but might be related to changes in the reservoir. Family 2 emerges when bottom hole pressure increases, and around 40 minutes before the well is shut in and proppant concentration increases to prevent a screen out. Changes in the overlying reservoir pressures might then be reflected in the waveforms emanating from asperities in the Keg-River formation.

Within these families we identify clusters of events which are both co-located and closely spaced (ACEs) by combining the CC matrix and the (d_{ij}) matrix. We identify three clusters of ACEs (Figure 3.9b). The first cluster consists of events from Family 2 only (Figure 3.9) and the second and third clusters contain events from Family 1 only (Figure 3.9). Within each cluster we observe significant stress drop variations that are larger than the associated uncertainties. Cluster 1 (i.e., C1) contains three events and shows a significant stress drop increase in ~20 minutes from 5 MPa to 13 MPa. Then around 10 minutes later the stress drop decreases to 5 MPa (Figure 3.10). Cluster 2 (i.e., C2) contains 3 events. The first event has a stress drop of 4 MPa, and then 30 minutes later stress drop is ~9 MPa. Finally, Cluster 3 (i.e., C3) shows an increasing stress drop from ~2 MPa to ~9 MPa within the first hour. Then ~2 hours later 4 more events are recorded, showing a significant stress drop decrease of ~11 MPa to 3 MPa (Figure 3.10a).

We need to take into account the possibility of M_w scaling on stress drop results to see if the large variation in stress drops can be explained by it. We control for the magnitude effect by adjusting stress drops according to the observed magnitude scaling. Corrected stress drops are calculated using the line of best fit from Figure 3.4b (i.e., scaled stress drops). If the largest stress drops within each cluster lie on a 1:1 line between observed and expected stress drops due to scaling, then magnitude scaling is the most likely cause for the observed variation. However, if there is a discrepancy this suggests that another explanation is needed. For C1 the stress drop variation of ~10 MPa cannot be explained by magnitude scaling because the largest stress drop (labelled 1 in Figure 3.10b) lies below the 1:1 line (i.e., this large stress drop cannot be explained by scaling alone). For cluster 2, the largest stress drop (labelled 2 in Figure 3.10b) also lies below the 1:1 line of expected stress drops due to scaling. Lastly for cluster 3, the largest stress drop is also significantly larger than that expected from the line of best fit. Thus, the observation of significantly large stress drop variation within clusters of co-located and highly similar events cannot be explained by the scaling of M_w and stress drop alone and requires an additional explanation.

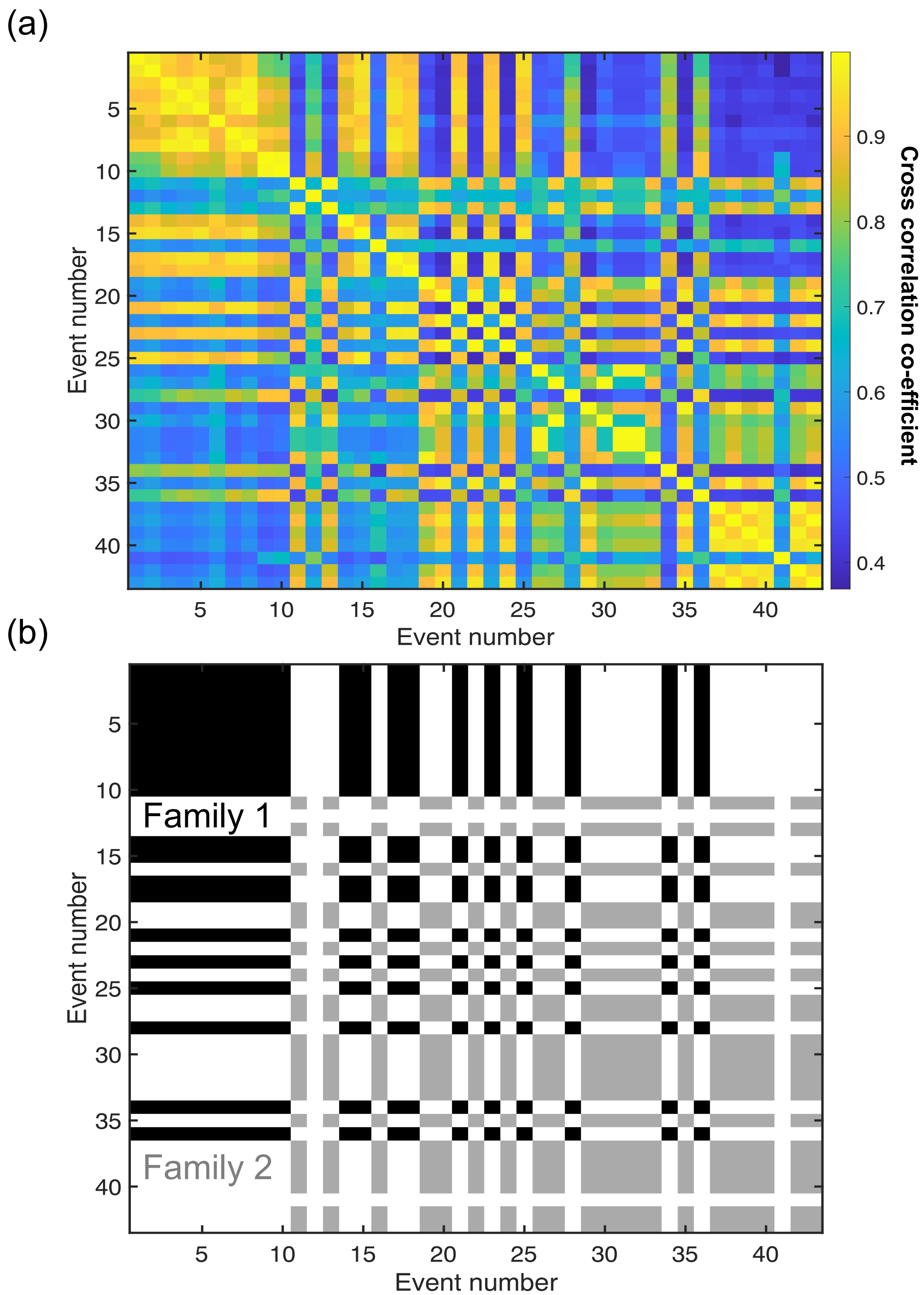

Figure 3.8: Classification of similar events using a cross-correlation matrix. (a) Cross-correlation matrix of the 43 events considered. (b) The two families of events. Black shows Family 1 and grey shows Family 2 Rows/columns that have no colours do not qualify to be part of a family of events.

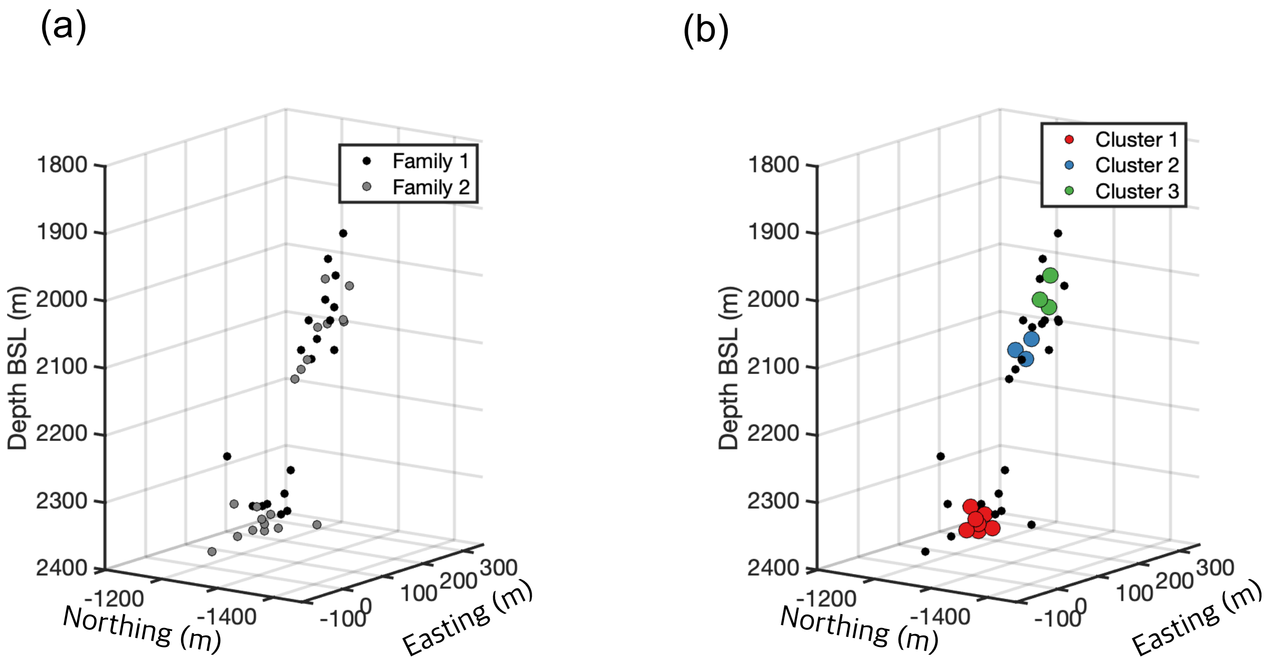

Figure 3.9: (a) Locations of target events corresponding to Family 1 and Family 2. (b) Locations of highly similar clusters. Three clusters of approximately co-located fault patches are shown by larger coloured circles. Smaller black circles show other events which do not fulfill the criteria for ACEs. Events within an ACE correspond to single families.

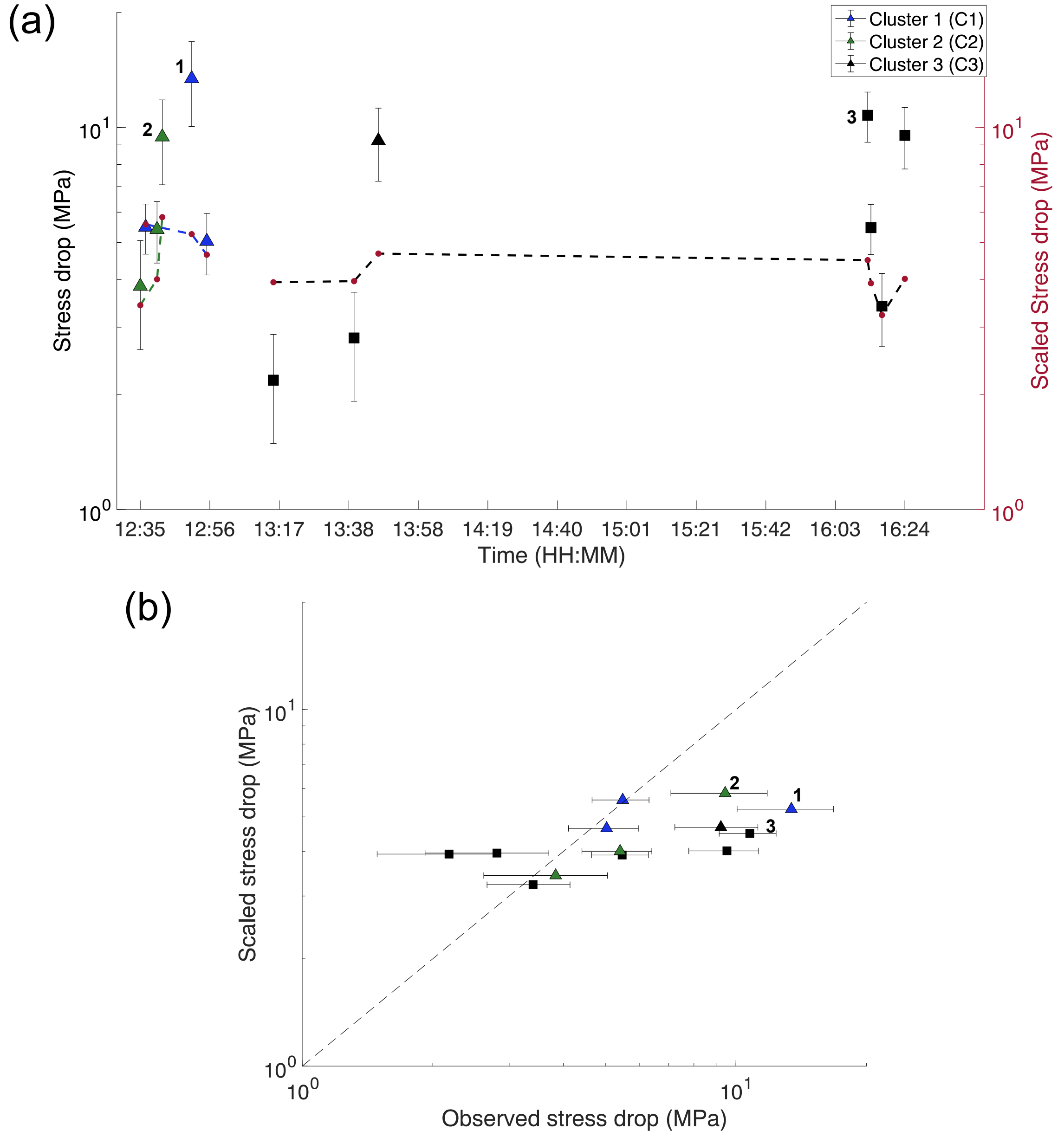

Figure 3.10: Stress drop variation in three clusters of approximately co-located events. (a) Stress drop vs time colour coded according to the three clusters. Dotted lines with red markers correspond to the scaled stress drop of each event (right y-axis). (b) Accounting for the magnitude scaling based on observed stress drops. Scaled stress drops are calculated from the average line of best fit in Figure 3.4.

3.5 Discussion

Compared to Chapter 2, we calculate a lower Q between 96-121, compared to Q = 180. Lower Q values of 110 and 120 are ruled in Chapter 2 because they result in unrealistically high stress drop estimates. In Chapter 2 we assume that intrinsic attenuation is the dominant attenuation mechanism when calculating Q, and other forms (i.e., scattering and geometrical attenuation) are not considered, whereas, here no mechanism is assumed (i.e., the attenuation function is generated empirically). Thus, the consideration of all forms of attenuation using the empirical based approach here could explain the differences in the Q values obtained.

We have used a systematically changing Q to describe the changes in the path spectra in Figure 3.6, however, a two parameter search may provide a better treatment of attenuation. Future studies may benefit from calculating a single Q and high frequency cut-off ($f_{\max}$) that best explain the empirical path data. These values could then be used to re-calculate the stress drops in Chapter 2.

The observation of stress drop scaling with M_w is unexpected according to the generally accepted geometric scaling of slip with rupture size (see Allmann and Shearer (2009) and references therein). We cannot rule out a physical reason for the scaling but the observation of a positively scaling stress drop more likely reflects limits in the spectral ratio method when applied to microseismicity. Although the spectral ratio accounts for attenuation, the method still relies on a measurable difference in the apparent corner frequencies - if both target and EGF apparent corner frequencies are close to the corner frequency limit (i.e., little measurable difference) it is a reasonable explanation for the observed scaling. Abercrombie (2015) show that if the high frequency instrument bandwidth limit is within a factor of 3 of corner frequency estimates then corner frequencies may be underestimated. Here, the Nyquist frequency (2000 Hz) is significantly above the range of corner frequencies (155-352 Hz). However, the high frequency cut-off at ~400 Hz still acts as a limit and may lead to underestimates of stress drops for smaller events. A high frequency filter which disproportionately attenuates more energy than lower frequencies (Deichmann, 2017) or fractures, analogous to the site effects which Hanks (1982) report could explain the high frequency cut-off. Thus although high frequency geophones enable us to retrieve higher frequencies, high frequency cut-offs could act as a limiting effect and lead to saturation of corner frequencies using spectral ratios.

The trade-off between event magnitude and where high frequency limiting effects arise likely influences the efficacy of spectral ratios. Analogous studies by Ide et al. (2003) and Yu et al. (2020) obtain corner frequencies in the range of 15-281 Hz and 12-41 Hz, respectively, because the magnitudes analyzed are in the range of $-1 < M_w < 3$ (larger than this study). In these cases there may still be high frequency cut-offs and both studies acknowledge the presence of site effects. However, these studies may be more likely to obtain separability of apparent corner frequencies between a target and EGF because corner frequencies are lower and therefore are not affected by high frequency cut-offs. Extending to much smaller magnitudes, such as the picoseismic events analysed by Kwiatek et al. (2011), self-similarity is still observed. In this case the recording environment is much more controlled with acoustic emission sensors. In our study a correction for high frequency filters that arise somewhere along the path between source and receiver might curb the apparent scaling observed here, however, it is still unclear what the physical explanation for high frequency cut-offs is for a given dataset as most studies rely on an empirical correction (Ktenidou et al., 2014).

In line with other studies, we also observe a systematic discrepancy between stress drops estimated using spectral ratios and direct fits (Ide et al., 2003; Yu et al., 2020). In this study spectral ratio stress drop estimates are on average twice as large compared to direct fits. The main reason for the difference is that here we calculate Q = 94-122 from K-well observations, which suggests stronger attenuation than the frequency-independent crustal attenuation of Q = 180 calculated using direct fits (Klinger and Werner, 2022). The differences in estimates shows that epistemic uncertainty in stress drop estimates can be significant depending on the method chosen to treat attenuation. Our results support trends from other studies which show that higher quality methods tend to lead to larger estimates of stress drop (Ide et al., 2003; Viegas et al., 2010; Yu et al., 2020).

From observations of stress drop along the reactivated structure, we do not observe a systematic anti-correlation between stress drop and distance from the point of injection. A closer analysis of co-located clusters shows that ACEs do not show the anti-correlation of stress drop with time. One possible explanation of these observations is that stress drops can be a proxy for pore-fluid pressure but a deviation from linear pore fluid diffusion means we do not observe a systematic anti correlation with space or time. In this case, pore fluid may reduce normal stresses relatively quickly along the entire fault zone, which leads to a stable average stress drop with distance from the point of injection. Such an interpretation supports the sensitivity of stress drop with fault strength (Zoback, 2009), as used by Allmann et al. (2011) to explain empirical observations from the enhanced geothermal project in Basel (Häring et al., 2008).

One of the difficulties of investigating microseismic ruptures is that the location uncertainties are often larger than the Madariaga (1976) circular crack radii calculated, which means it is not clear whether ACEs express co-located seismic events which might be repeaters, or events with hypocentres up to 100 m away from each other (maximum relative location uncertainty between two events). The two scenarios are treated as end-members for geomechanical interpretation of the results. In the scenario ACEs represent co-located events (which might be indicative of the same asperity) stress drop differences are less likely to reflect fault material differences. One plausible explanation for the stress drop differences within a cluster is small scale pore pressure differences with time. Similar conclusions are reached by Lengliné et al. (2014) who suggest that the large, but non-systematic changes in stress drop (a factor 40 over 4 hours) at the geothermal experiment in Soultz-sous, France, is mostly likely due to local variations in pore pressure on the same fault patch.

In the case that ACEs do not represent the same fault patch the cause for variation is less clear. Stress drop variations may still be explained by pore pressure differences but material differences could also explain observations. For example, if a seismic event within ACEs expresses an asperity with a more heterogeneous composition than another event in the same cluster, we may expect a lower fault strength (Bedford et al., 2022), and therefore lower stress drop for the first event. Another possibility is that within a cluster one seismic event represents an asperity with more damage, which could also lead to lower stress drops (Moyer et al., 2018). To aid our understanding of stress drop differences we would benefit from a controlled lab study on the competing geomeochanical effects (i.e., roughness, pore pressure heterogeneity, etc.), and how the resulting stress drop observations on microfractures changes.

3.6 Conclusion

In this study we calculate stress drop estimates from 31 -0.55 < M_w < 0.4 seismic events induced by hydraulic fracturing operations in the Horn River basin, British Columbia. We use the spectral ratio method to calculate an average stress drop of 4 ± 2 MPa, which is twice as large as estimates determined from direct spectral fits. These greater stress drops probably result from a better treatment of attenuation and site effects. From the source corrected spectra we calculate a lower Q of 94-121 compared to the estimate from direct fits of Q =180. We observe a signal of increasing stress drops with moment which is most likely caused by high frequency limits in the form of cut-offs, even when spectral ratios are used. We do not observe a systematic anti-correlation of stress drop with distance from the point of injection, nor do we observe a systematic anti-correlation of stress drop with time within highly similar and co-located clusters. If we interpret these observations accepting that an increase in in-situ pore pressure should reflect stress drop variations, then one plausible explanation is that we are observing a relatively rapid diffusion of pore fluid along a fault structure which lowers effective stresses, and therefore stress drops over a large spatial footprint compared to observations in other datasets. Within closely spaced events, variations could result from local pore pressure differences. However, the small event sizes and difficulty in prescribing a sole explanation for stress drop variations, precludes a definitive interpretation.

Chapter 4

Sensitivity analysis on the fault stability of a major structure

The following chapter steps away from high frequency source parameters and delves into the geomechanics of the major fault structure which is reactivated during operations. Using new information from focal mechanisms and World Stress Map data, the next chapter examines the sensitivity of fault orientation and stress field azimuth on inferred fault stabilities. I conducted all analysis, produced all figures and wrote the manuscript. Maximilian Werner and Joanna Holmgren provided edits to the manuscript.

During hydraulic fracturing operations at a pad in the Horn River basin from July-August 2013, a fault structure was reactivated and caused the largest recorded seismicity (M_w = 0.5) during the operations. This dataset provides an interesting test case of the Fault Slip Potential (FSP) method, which calculates probabilistic estimates of the additional pore pressure needed to bring a fault in a 3D stress field to frictional (Mohr-Coloumb) failure. Kettlety et al. (2019) applied the FSP method to this dataset to assess fault stability and estimated pore pressure required for failure. Here, we glean new insights into the sensitivity of the estimated fault stability from new estimates of the fault orientation, slip direction and stress field orientation. Firstly, we find that the maximum horizontal stress direction (SH_{max}) inferred from the closest borehole breakout direction at the local scale differs by ~80° from the regional average, indicating a heterogeneous stress field. Secondly, the geometry and sense of slip of the fault is ambiguous. From a P and S wave compound focal mechanism we calculate a strike of 45° ± 10° whereas seismicity locations reveal a 73 ± 10° strike. Thirdly, the inferred fault stability is very sensitive to the choice of SH_{max} direction length scale, as we illustrate with different but plausible choices from the WSM. The fault structure analysed here requires 1.8 times more additional pore pressure (at 33%

chance of failure, as determined from literature) to destabilise with a nearby estimate of SH_{max} direction than with in-situ measurements of the SH_{max} direction. Our findings question the confidence in characterising a fault as safe or unsafe based on estimated inputs into FSP.

4.1 Introduction

Subsurface geo-energy development projects involving fluid injection can destabilise fault structures and lead to earthquakes (Ellsworth, 2013; Lei et al., 2017). In most cases the seismicity that results from strain release is small enough to be unnoticed (Foulger et al., 2018). However, some industrial projects are linked to damaging earthquakes, e.g., when seismicity is hosted on reactivated fault planes in the underlying basement rock in the case of hydraulic fracturing (HF) operations (Bao and Eaton, 2016; Lei et al., 2017). To mitigate the risks associated with these industrial projects, it is desirable to determine the stability of major faults that could be reactivated and the mechanism by which destabilisation could occur. If there is a direct hydraulic connection, then it is useful to know the amount of additional pore pressure that can be injected along the fault structure before failure occurs.

The Fault Slip Potential (FSP) method by Walsh et al. (2017) calculates the probability of reactivating a fault using the Mohr Coloumb failure criterion. Fault stability can be estimated using information about the principle stress magnitudes, SH_{max} direction, fault geometry, formation pore pressure and the associated uncertainties for each of these variables. These data are input into FSP, which outputs the additional pore pressures needed to cause failure. For a population of faults with a prescribed regional SH_{max} direction, several authors have claimed that unstable faults can be identified using FSP and the method is frequently used (e.g., Walsh and Zoback, 2016; Kettlety et al., 2019; Hennings et al., 2019; Nantanoi et al., 2021; Hennings et al., 2021). As a retrospective tool (i.e., after the seismicity occurred), FSP was used to show that fault segments producing the 2011 M_w 5.6 Prague earthquake and the 2016 M_w 5.8 Pawnee earthquakes were critically primed for failure (Walsh and Zoback, 2016). In the case of hydraulic fracturing induced seismicity, the roughly N-S striking fault structures linked to seismicity at Preston New Road are correctly identified as primed for failure, although these structures were only revealed after seismicity (Nantanoi et al., 2021). However, others have raised caution about how confidently we can infer fault stabilities using FSP. The triggering of structures that are identified as unfavourably aligned in the stress field for failure during waste wastewater activities is one such example (Cochran et al., 2020); whilst the mainshock is optimally orientated for failure, foreshocks and aftershocks are not, and therefore not expected to occur. It is suggested that elevated pore pressures are needed to explain foreshock and aftershock seismicity, which requires additional hydromechanical and pre-existing fault stress information when using FSP (Cochran et al., 2020).

Within a more heterogeneous stress field (i.e., more variable SH_{max} direction recordings), inferred fault stabilities may be more sensitive to the chosen SH_{max} direction length scale. The length scales at which SH_{max} direction changes have been studied (e.g., Schoenball and Davatzes, 2017) although to our knowledge little research has extended to the impact on fault slip calculations, which is the focus of this paper. Regional stresses may not be truly representative of the stresses acting along a fault structure. At the large scale (i.e., > 500 km) first order effects on stress directions are predominantly from tectonic strain (Heidbach et al., 2007). Secondary (i.e., 100-500 km) and tertiary effects (< 100 km) can cause deviations in the stress field (e.g., from active faults) (Heidbach et al., 2007). At the intermediate scale (i.e., 1 - 35 km) we may see vertical and lateral variation, particularly at the edges of sedimentary basins (Luttrell and Hardebeck, 2021). At the small scale (i.e., 1 km), fault structures can develop their own local stresses which differ from regional stresses (Gudmundsson et al., 2010). While FSP is a probabilistic method that accounts for uncertainties, no studies (to our knowledge) have assessed the sensitivity of the resulting probability distributions to SH_{max} direction and fault geometry despite potentially important decisions that might be based on the FSP method.

Often, the only way to accurately determine the orientation of principle stresses is to measure in-situ SH_{max} direction. Such measurements can be obtained via borehole breakouts (e.g., Bell, 2015) at the depth of fault structure being analysed or by observing the orientation of fracture corridors illuminated by seismicity in the context of hydraulic fracturing. In the case of tight shale exploration in the Horn River basin (Canada), the velocity-weakening nature of the shale (Allen et al., 2021) is expressed in the rich seismic catalogues induced by exploration (Baird et al., 2017). However, if the faults of interest are deeper than the borehole breakouts or depth of fracture corridors, the SH_{max} direction along these faults may differ from SH_{max} derived at the depth of borehole breakouts in basin environments. We may expect both lateral and depth variations in SH_{max} direction at length scales of <1-10 km, which are most significant at basin edges (Luttrell and Hardebeck, 2021).

For a geo-energy project we may have some idea about the geometry of major fault structures from mapped faults or 3D seismics but may not have in-situ measurements of the stress field at the specific location of a fault. In the absence of local stress data, the World Stress Map (WSM) is a natural resource to use (e.g., Carafa and Barba, 2013; Butcher, 2018; Healy and Hicks, 2021). The question that arises is how reliable can data from the WSM be at predicting the stability of known faults when integrated into FSP?

This study evaluates the sensitivity of fault stability estimates from the FSP method when using data from the WSM. We use a dataset from HF operations in Canada as a case study for this purpose (Baird et al., 2017; Verdon and Budge, 2018; Kettlety et al., 2019; Klinger and Werner, 2022). Kettlety et al. (2019) (hereafter K2019) investigated the role of elastostatic stress transfer, concluding that it is not itself enough to explain the stress changes needed to destabilise the faults that underlie the play in the Horn River basin. K2019 also used FSP to estimate the stability on the major faults structures but inferred fault geometry from seismicity, as the structure was previously not known. Here we estimate the range of additional pore pressures needed to destabilise the largest observed structure, which we approximate as a single plane. Firstly, we calculate a range of SH_{max} direction estimates from the regional to local scale on the basis of the WSM. Secondly, we constrain fault orientation using a compound focal mechanism from P and S wave arrivals of well-constrained events on the structure, and from their hypocentres. Then we calculate the range of additional pore pressures that can induce failure on the fault structure using two methods. The first method isolates uncertainties corresponding to fault strike and the maximum principle stress direction; the second method (FSP) considers all uncertainties. We use these results to examine the utility of the FSP method when data inputs are uncertain.

4.2 Data and methods

4.2.1 Horn River basin seismic dataset

We use data collected during hydraulic fracturing treatment in the Horn River basin (Canada), which targeted three organic-rich shale gas units. The contractor provided us with seismic data recorded between July-August 2013 from three downhole borehole geophone arrays. Each array consists of 36, 15-Hz geophones sampling at 4000 Hz. The catalogue of more than 90,000 $-3 < M_w < 0.5$ seismic events also contains stress drops, moment tensor inversions and fault radii for 35 % of the events (e.g., Baird et al., 2017; Verdon and Budge, 2018; Kettlety et al., 2019). We were also provided with drilling and borehole data which includes well head pressures, slurry rates and sand concentration in the formation.

The fault structure of interest is linked to stimulation at stage A14 (SA14, Figure 4.1a), which is illuminated by seismicity in the underlying limestone formation (Figure 4.1b). At most stages induced seismicity occurs in the shale play, which appears as a diffuse cloud (Figure 4.1b). The fault structure we analyse is illuminated by 6740 seismic events following injection at SA14 and hosts the largest event (M_w = 0.5) in the dataset (Figure 4.1b). Recorded seismicity within the stimulated shale is termed in-zone and along clear fault structures in the underlying limestone as below-zone.

Patch 1 is between ~1900-2100 m and patch 2 is between ~ 2200-2400 m (Figure 4.1b). For constraining fault geometry from seismicity in section 4.3 we consider all events linked to SA14. However, for the purpose of constraining fault strike using focal mechanisms in section 4.3, we limit our analysis to the first 10 events which all show clear phase arrivals. When calculating fault stability in section 4.3, we model the fault structure at 2100 m (the average depth of the 43 largest events). Considering that absolute uncertainties in location are ± 100 m (Kettlety et al., 2019), 2100 m provides a reasonable approximation of the depth below sea level at which the seismicity of interest occurs. To account for the rock mass above sea level, we add on the additional Kelly-Bushing depth of 707 m, which gives a true vertical depth of ~ 2800 m (Kettlety et al., 2019). Klinger and Werner (2022) describe further details of the velocity model and the locations.

4.2.2 World Stress Map data

To characterise the stresses acting on a fault we need the orientation and amplitude of the principle stresses on the fault geometry. Both principle stress magnitudes and SH_{max} orientations are contained in the WSM (Heidbach et al., 2016). Errors linked to SH_{max} amplitudes can be significant but the probabilistic FSP should account for these uncertainties. However, the choice of SH_{max} direction, especially in a heterogeneous stress field depends on what length scale one believes tectonic processes are affecting the analysed fault planes. Within sedimentary basins we may observe small scale variations on the scale of < 1-10 km in SH_{max} orientation, which are significantly smaller than first order tectonic effects on the order of > 500 km (Heidbach et al., 2007). WSM SH_{max} orientations are classified from A-D to indicate data quality. We only use data quality A-D. Quality A corresponds to orientations of SH_{max} that are accurate to within ± 15°, quality B are accurate to within ± 20°, C lies within ± 25° and D is within ± 40° (Heidbach et al., 2007). The uncertainties are mostly obtained through standard deviations (Heidbach et al., 2016).

4.2.3 WSM data analysis

Western Canada shows a dominantly NE-SW striking SH_{max} direction regionally (Wang et al., 2018), reflecting the tectonic strain direction from geodetic observations (Kao et al., 2018). We classify SH_{max} direction measurements based on the length scales the stress field is sensitive to (Heidbach et al., 2007). As shown in Figure 4.2, the first group, which we term regional SH_{max}, is the average of 150 SH_{max} direction recordings within 750 km of the pad which includes primary and secondary effects at the 500+ km scale. We collapse all SH_{max} measurements on a semicircle between 0-180° and then take the mean to calculate the average SH_{max} direction. The second group uses 27 measurements within 100 km from the pad (considered tertiary effects), which we call the local SH_{max}. The third group uses 7 measurements obtained within 35 km from the pad, which we term near SH_{max}. Within the near SH_{max} length scale we may observe vertical and lateral variations on the scale of sedimentary basins (Luttrell and Hardebeck, 2021). We also consider the closest borehole breakout at 12 km away, denoted closest SH_{max}.

We calculate the average for each SH_{max} length scale. Regional SH_{max} is 59° ± 40°, local SH_{max} is 86° ± 48°, near SH_{max} is 112° ± 46° and the closest SH_{max} is 131° ± 26° (Figure 4.2). We calculate the variability in SH_{max} azimuths using the standard deviation because the variation between SH_{max} azimuths is likely to include systematic variations of the mean SH_{max} direction rather than a uniform value across the studied region. For the closest data point we use the measurement uncertainty as we only have one estimate. Most of these measurements are obtained from borehole breakout data. The nearest measurements based on multiple focal mechanisms give an average SH_{max} direction of 45° (Heidbach et al., 2016), although all focal mechanisms are at least 100 km from the pad and therefore do not capture small scale local variations which show a change in average SH_{max} direction from NE-SE to ESE-WNW (Figure 4.2c-e).

K2019 calculate the SH_{max} direction as 55° ± 10°, which is supported by the orientation of wells roughly NW-SE along SH_{min} at the studied pad (Figure 4.3a) and other surrounding pads (Oil and Commission, 2012). By orienting the wells in this way, the operators aim to stimulate the largest fracture volumes, parallel to SH_{max} (Maxwell, 2014). Observed seismicity clouds strike roughly NE-SW, (Figure 4.3a), which adds further evidence to a NE-SW SH_{max} direction. We determine the SH_{max} direction within the stimulated shale from in-zone microseismicity as 50° ± 3° (Figure 4.3a) which we term fracture SH_{max}. WSM SH_{max} orientation uncertainties here have significantly larger uncertainties than K2019 because we use standard deviations from the WSM whereas K2019 use ±10°.

We use principle stresses at the average depth of seismicity (2800 m) calculated by K2019. K2019 calculate stress gradients using stress data from industry well logs, well history reports and drilling histories collected by Bell (2015). S_v was calculated as 66 MPa ± 5 MPa and uncertainties were calculated using York fits, which provides estimates of gradient uncertainty (York et al., 2004). K2019 use a mean hydrostatic pore pressure gradient of 9.8 MPa/km (i.e., 27 MPa at the depth of the fault) with an uncertainty of ± 7 MPa. K2019 calculate SH_{max} = 77 MPa ± 12 MPa and SH_{min} = 51 ± 6 MPa at the depth of the fault.

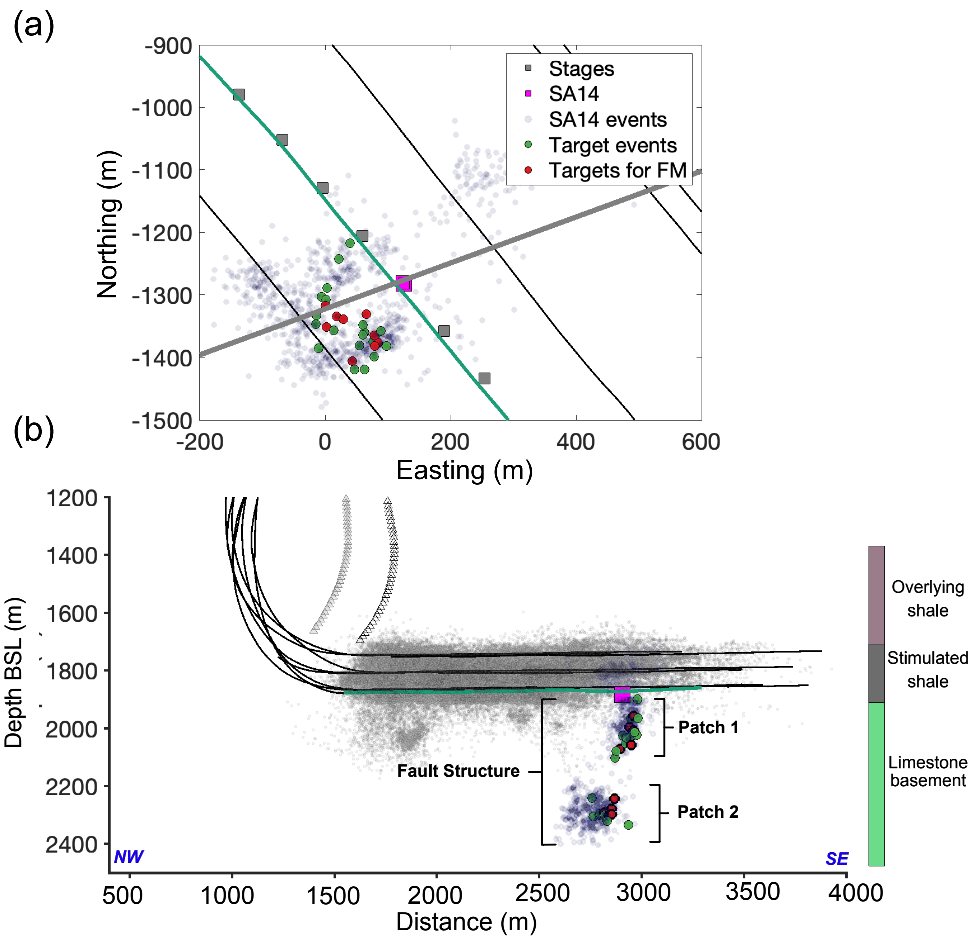

Figure 4.1: Map and cross sectional views of induced seismicity at a pad within the Horn River basin highlighting a reactivated fault structure. (a) Map view of events linked to injection at well A, stage 14 (SA14), which are denoted by blue circles. Of these, 43 events are used for analysing phase arrivals are shown by green circles (see text for selection criteria). 10 red circles show events used for constraining the compound focal mechanism in section 3.3. Wells are shown by black lines and the green line is well A. (b) Toe-heel, multi-well hydraulic fracturing operation showing the cloud of 90,000+ induced seismic events (Baird et al., 2017). Triangles show the borehole geophone arrays. Other lines and symbols are the same as in (a). Seismic events illuminate a reactivated fault structure, with two clear patches, as labelled.

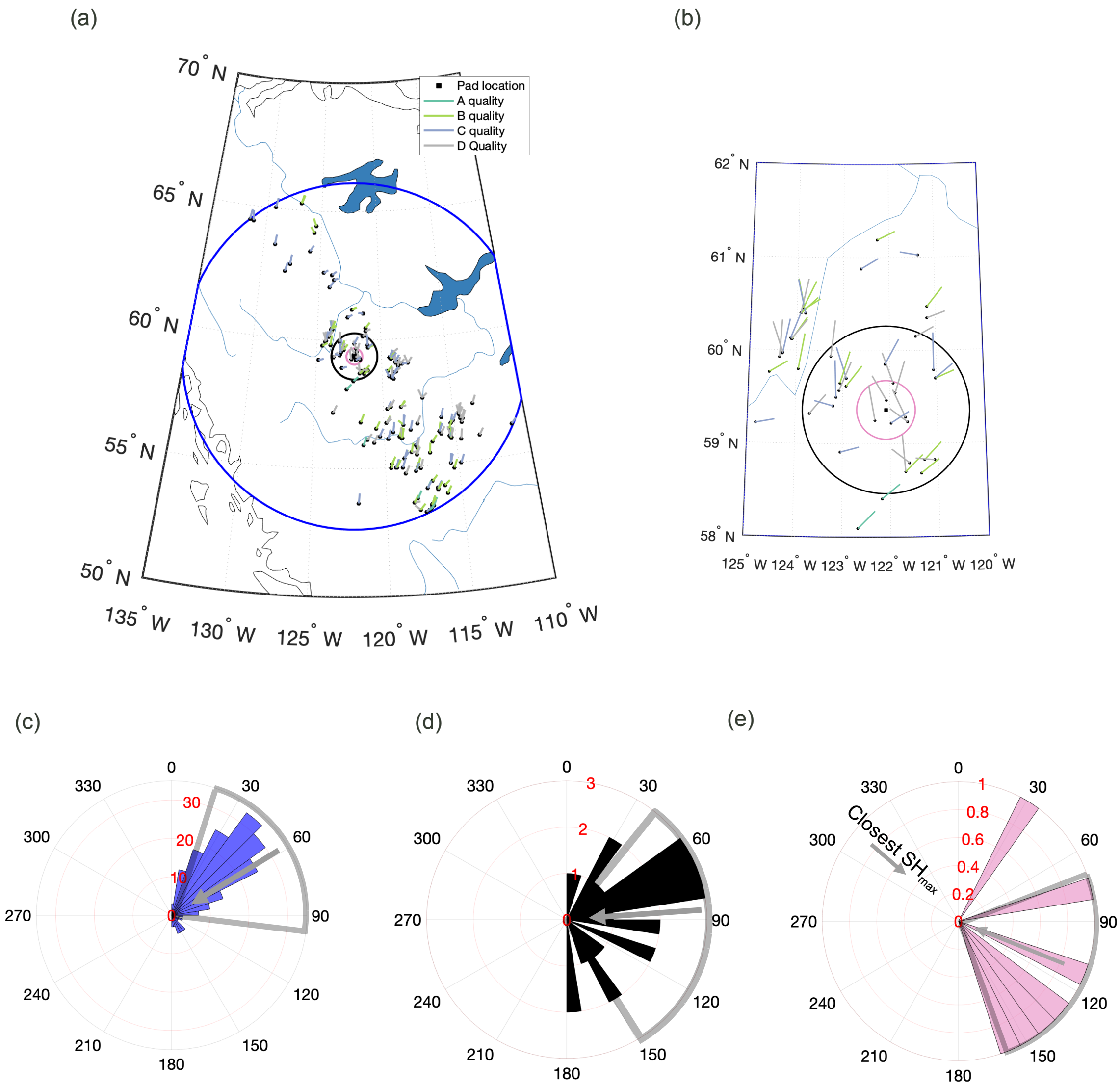

Figure 4.2: SH_{max} stress directions at different length scales from WSM data (Heidbach et al., 2016). (a) Map projection of Western Canada. The pad is shown by a black square. Black dots and short georeferenced lines denote SH_{max} direction data, respectively. Turquoise, green, purple and grey lines represent quality A, B, C and D according to the WSM, as per legend in (a). Circles represent distance bins from the pad. Data within the blue circle represent regional SH_{max} (i.e., ≤ 750 km); data within the black circle contribute to local SH_{max} (i.e., ≤ 100 km); data within the magenta circle correspond to near SH_{max} (i.e., ≤ 35 km). (b) A zoomed in map of SH_{max} direction measurements closest to the pad. (c-e) Polar histograms of SH_{max} directions from (c) regional SH_{max}, (d) local SH_{max} and (e) near SH_{max} with bold arrows showing the circular average for each SH_{max} length scale. The closest SH_{max} direction, based on the nearest point is denoted by a grey arrow in (e). Grey segmented boundaries in c-e represent the standard deviations of SH_{max} directions. Grey arrow denotes the circular average.

4.2.4 Compound focal mechanism

To obtain a compound focal mechanism we manually determine polarities from phase arrivals rotated into the rayframe, either as up, down or unclear. We repeat this process over all phases (i.e., P, SH and SV) along both the K- and S-wells for 10 events, which are representative of the shallow and deeper seismicity patches along the reactivated fault structure (Figure 4.1). We obtain 210 polarity measurements for each event, which we use to construct upper hemisphere projections using inclination and azimuth orientations determined from the 3D geometry between station and event.

Using some assumptions we constrain the focal mechanism, which would otherwise be very difficult considering the paucity of azimuthal station coverage. Multiple observations suggest the fault structure is sub-vertical with a strike slip mechanism. Firstly, other focal mechanisms in the Western Canadian sedimentary basin show dominantly strike-slip focal mechanisms (Wang et al., 2018), as well as specifically near another play within the Horn River basin (Hurd and Zoback, 2012). Secondly at any given station, the polarities are nearly identical across all events along the fault, which might not be expected if the fault had a significant dip. Thirdly, the seismicity clearly illuminates a sub-vertical structure (Figure 4.1). Lastly, according to Anderson's classification (Anderson, 1905), we expect a strike-slip mechanism because S_v is the intermediate stress estimate. Therefore we assume the seismicity can be represented by a vertical plane that undergoes failure with a strike slip mechanism.

4.2.5 Modelling fault stability

Once the fault strike and sense of slip are determined from the seismicity and compound focal mechanism, we can assess the sensitivity of inferred fault stability to SH_{max} azimuth. We approximate the fault structure as a vertical plane and use a Mohr-Coloumb diagram to evaluate the shear and normal stresses on the plane with the five different SH_{max} directions that represent the epistemic uncertainty of this input parameter (Section 3.3). Using Coloumb's law, critical shear stress τ_s can be written as

$$\tau_s = \mu_{fric}\sigma_n + C, \tag{4.1}$$

where μ_{fric} is the coefficient of friction and C is cohesion, which we assume is negligible. The failure lines correspond to the frictional coefficient $\mu_{fric} = 0.7$, calculated by Chou et al. (2011) based on measurements in the Horn River basin. Then, based on regional SH_{max}, local SH_{max}, near SH_{max}, closest SH_{max} and fracture SH_{max} directions, we calculate the shear and normal stresses acting on the fault plane for each SH_{max} length scale and construct the corresponding Mohr circles.

We use two methods for characterising fault stability. All inputs are summarised in Table 3.1. In the first method (Method 1) we isolate the SH_{max} direction and fault strike uncertainties, on which we have some constraints that change depending on the stress field length scale and strike of the reactivated structure. The second method propagates uncertainties of all input parameters (Table 3.1). By comparing Method 1 and Method 2 we can assess how significant the differences of inferred stability are based on SH_{max} length scales and geometry relative to Method 1, which isolates these uncertainties.

For a particular SH_{max} direction, fault stability estimates are made on two planes which represent the strike uncertainty (planes A and B). If the calculated fault stabilities between methods are more discrepant than stabilities calculated using different planes (but for the same method), then the chosen method is the more significant uncertainty. Similarly, if inferred stabilities using one fault strike relative to another are more variable than stabilities arising from different SH_{max} azimuth length scales, this would imply that fault strike is the major cause of uncertainty.

For Method 1, stress states for a chosen SH_{max} direction are described by an arc range on a Mohr circle. The arc range reflects the uncertainties in the strike and SH_{max} direction. For each point along the arc, we calculate the reduction in effective normal stresses needed to reach failure. The smallest value is the minimum amount of additional pore pressure required to cause failure. Method 1 does not take into account uncertainties in the principle stress magnitudes nor formation pressure and therefore does not account for the possibility of overpressure.

Method 2 uses FSP. Firstly, FSP deterministically calculates the amount of pore pressure needed to cause failure. Then, FSP runs Monte Carlo simulations over the range of values corresponding to the uncertainty of input parameters which outputs a probability function of inducing failure (Walsh et al., 2017). Thus Method 2 includes the possibility of overpressure. The input parameters are: orientation of the fault planes, stress gradients, principle stress orientations and the coefficient of friction, with the associated uncertainty of each variable.

For mitigating induced seismicity, operators benefit from knowing a minimum amount of additional pore pressure which could result in failure. FSP outputs the probability of inducing failure for a given additional pore pressure as a percentage where 100% corresponds to an additional pore pressure that is most likely to cause failure. Determining what percentage should be used depends on how conservative the operator should be when estimating fault stability. We deterministically assign the critical additional pore pressure when there is a 33% probability, as used by Walsh and Zoback (2016), to characterise critically stressed faults.

Input parameters	Magnitude	Uncertainty (±)
σ_1 (MPa)	77	12
σ_2 (MPa)	66	5
σ_3 (MPa)	51	6
P_o (MPa)	27	7
regional SH_{max} (°)	59	40
local SH_{max} (°)	86	48
near SH_{max} (°)	112	46
closest SH_{max} (°)	131	26
fracture SH_{max} (°)	50	3
Strike, Plane A (°)	73	10
Strike, Plane B (°)	45	10
Dip (°)	90°	5
μ_{fric}	0.7	0.1

Table 4.1: Input parameters into FSP to assess fault stability, with associated uncertainties. σ_1, σ_2 and σ_3 are the greatest, intermediate and smallest principal stresses. P_o is the in-situ pore fluid pressure. Plane A is determined using constraints from the seismicity and plane B uses constraints from the compound focal mechanism. The listed input parameters describe stress field (σ_{1-3} and P_o), SH_{max} length scale (regional, local, nearby, closest and fracture SH_{max}), fault geometry (strike and dip) and the frictional coefficient (μ).

4.3 Results

4.3.1 Constraining fault orientation and slip direction

Firstly, we constrain the strike of the fault structure using the below-zone microseismicity. We cluster closely spaced events into groups based on a threshold neighbourhood search radius, which we set to 50 m and a minimum number of points (we assign this as 3 points). Using this information a core point can be identified using dbscan in MATLAB (Ester et al., 1996). We identify two clusters which express two clear fault patches (Figure 4.4). For each patch we use a least squares linear fit to determine the strike. For patch 1, the strike is 70 ° ± 1° and for patch 2 the strike is 76 ° ± 2, giving an average strike of 73° ± 3°, which is very similar to the a strike of 70° ± 10° determined by K2019 with the same data. To reflect a more realistic uncertainty, we use the uncertainty determined by K2019 (± 10°). Compared to in-zone seismicity, which shows a consistent angle of 50° ± 3°, the fault structure shows a clearly different orientation (Figure 4.4), which suggests an older reactivating fault rather than an extension to depth of the hydrofracks which align with fracture SH_{max}.

The ten inspected events along the fault structure, which we use to constrain the compound focal mechanism, all have clear positive P-phase polarities (i.e., compressional) along both wells (Figure 4.3b). A strike of 20-60° or a strike of 110-150° is consistent with P-phase polarities alone (Figure 4.3b). The nodal plane ambiguity is resolved through observations of the seismicity that is NE-SW. Using SH-phase first motion polarities, a right lateral strike-slip fault with a strike of 35-55° (i.e., 45° ± 10°) is consistent with our observations (Figure 4.3c). Thus the switch in SH-phase polarity between the K- and S-well allows us to constrain the strike and rake. We construct P and SH nodal planes consistent with a 45° strike in Figure 4.3a. The S-well lies within the quadrant where we expect to see negative SH polarities, and quite close to the plane where the switch should occur (Figure 4.3a).

We explore some ways to explain the difference between the strike obtained from the compound focal mechanism (45° ± 10°) and the strike obtained from seismicity (73° ± 10°). To assess whether we can find consistency between a 73° strike and polarity observations we relax the assumptions of dip and rake from a vertical structure. Changing the dip up to 70°, whilst keeping the strike the same, produces a compound focal mechanism which is less consistent with polarity observations than using a 45° strike and assuming a vertical structure. Similarly, changing the rake between -20 to 20° from 0° also produces a compound focal mechanism which does not agree as well with polarities compared to using a 45° strike. Another possibility is the incidence angle between station and event, which assumes a straight line ray path; in reality the ray will bend towards a more vertical angle, which might cause slightly different inclinations. However, because density variations between lithological layers are relatively small (Sayers et al., 2016), polarity positions on the focal sphere are unlikely to shift significantly. Thirdly, the highly anisotropic nature of the shale may introduce a non double couple (DC) component (Boitz et al., 2018). Adding some amount of a non-DC component might provide a more consistent mechanism with a 73° strike, however, this would add additional complexity to the fault mechanism from limited observations. Given the ambiguous constraints on the fault strike, we consider both scenarios: a 73° ± 3° strike slip structure (plane A) and a 45° ± 10° slip structure, (plane B). Lastly, the 45° may represent the strike of en-echelon fractures and the 73° strike might represent the overall en-echelon structure.

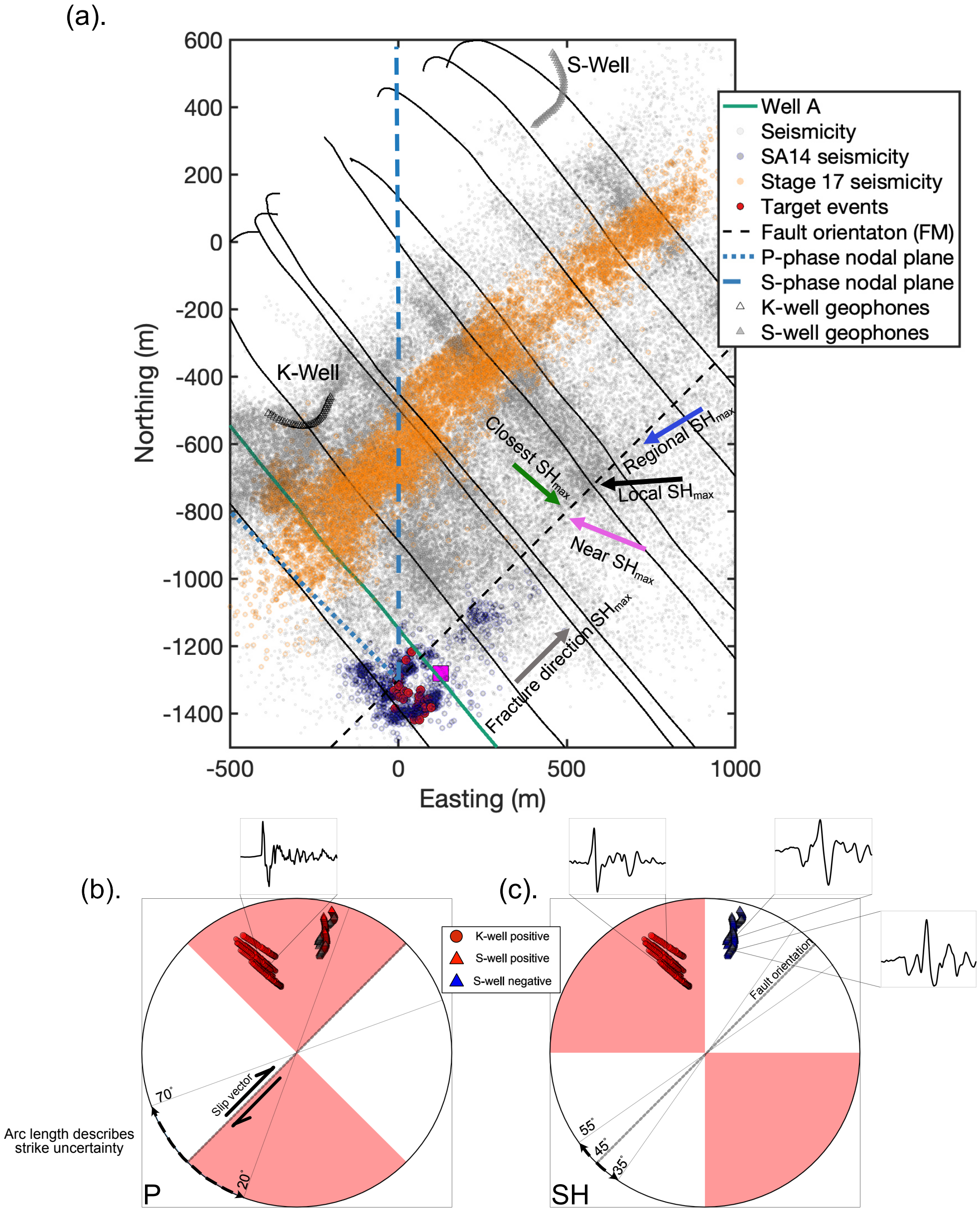

Figure 4.3: Map of seismicity with various estimates of SH_{max} direction and the best fitting nodal planes according to first motion polarity focal mechanism constraints on fault geometry (b and c). (a) Map showing induced seismicity, the fault strike determined using a first-motion compound focal mechanism (45°), and projections of P- and S-phase nodal planes. SH_{max} directions considered for fault stability analysis are shown by arrows, as labelled. Microseismicity associated with stage 17 is coloured orange. (b) and (c) compound upper-hemisphere focal mechanisms using 10 events for the best fitting strike. Markers show polarities of individual stations projected onto the focal sphere. Red indicates a positive polarity, blue markers denote negative polarities and grey markers show unclear polarity. Circles show K-well measurements and triangles represent S-well measurements. Thin grey lines show limits of strikes consistent with polarities. Range of possible strikes is shown by double headed dashed black line as annotated.

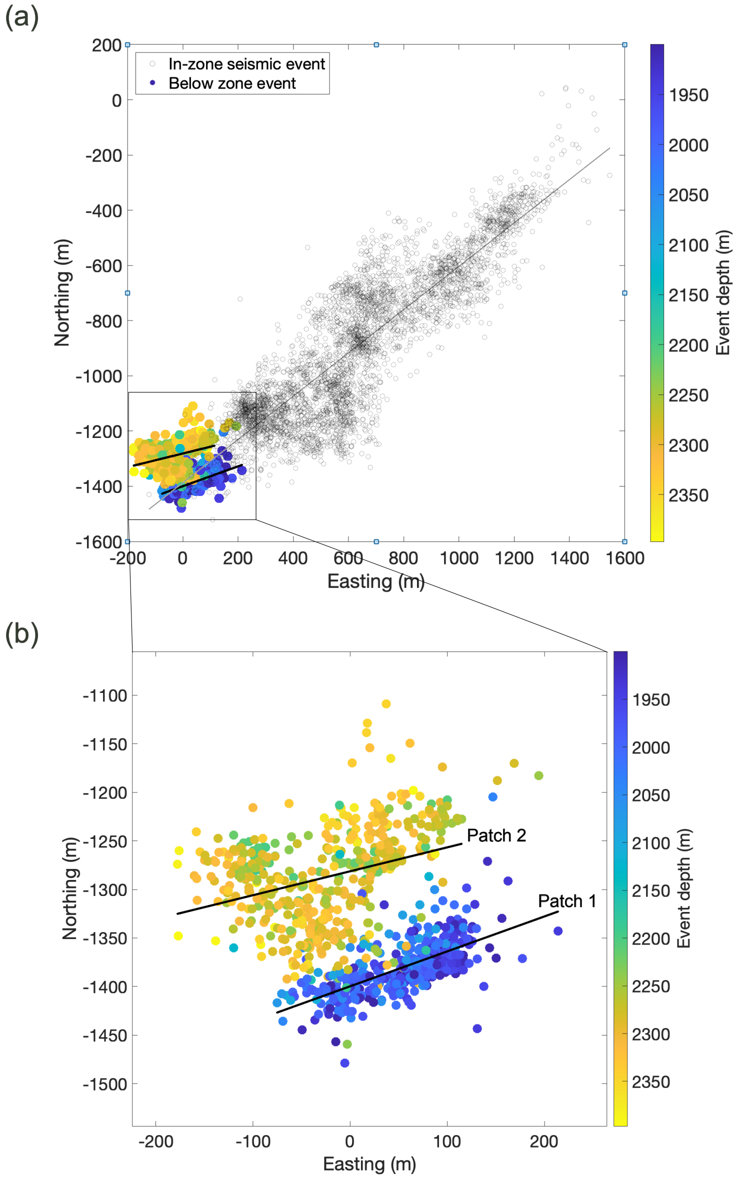

Figure 4.4: Map views of seismicity demonstrating the change in strike from in-zone to below-zone seismicity on the reactivated structure. Map of seismicity linked to SA14 showing (a) in-zone (grey circles) and below zone (larger coloured circles) seismicity with a grey line denoting line of best fit fitted to in-zone events (least squares) and black lines of best fit to below zone events (b) a zoomed in map of coloured events in (a) showing two patches linked to the fault structure (Figure 4.1). Each patch has a black line of best fit.

4.3.2 Mohr-Coloumb failure and fault slip analysis

We evaluate how stable the fault structure is using the multiple SH_{max} length scale estimates on planes A and B using both methods. To provide a deterministic threshold which an operator would benefit from knowing, we calculate the pore pressure needed to cause at least a 33% chance of failure using Method 2. For Method 1 we use the minimum amount of additional pore pressure to cause failure. Table 3.2 summarises these results.

Using Method 1, the most striking observation is the large range of possible stress states that satisfy observations and uncertainties of the chosen SH_{max} length scale and fault strike. Compared to a single point on the circumference (an idealistic scenario in which there is no uncertainty), in three cases (regional, local and near SH_{max}) more than half of the Mohr circle is covered using plane A or B (Figure 4.5a-f). Because SH_{max} direction uncertainty is so large, the corresponding range of additional pore pressures for each SH_{max} length scale is quite insensitive to any choice of SH_{max} (Figure 4.5i). For both planes fracture SH_{max} provides a smaller range of additional pore pressures because the fracture direction is much better constrained than SH_{max} orientation data from the WSM.

Using FSP, SH_{max} length scales calculated from WSM data all produce significantly larger uncertainty in the amount of additional pore fluid compared to fracture SH_{max} and the estimate by K2019 (Figure 4.6). Regional, local, near and closest SH_{max} directions could require a 19-54 MPa range of additional pore pressures to reasonably cause failure (i.e., 33%-100% probability). Considering well head pressures are up to ~ 60 MPa, and that the fault structure most likely connects up to the shale reservoir (as revealed by seismicity), the additional pore pressure estimates are reasonable on the basis that seismicity occurred at these pressures. Compared to WSM derived SH_{max} azimuths, fracture SH_{max} corresponds to a 19 MPa range of additional pore pressure that could induce failure and produces uncertainties similar to the curve by K2019 (Figure 4.6). The more uncertain FSP curves linked to WSM derived SH_{max} azimuths is because the associated uncertainties are significantly larger than fracture SH_{max}. Given the uncertainties in inputs, fault stability is quite unconstrained.

The question that follows is: does the uncertainty of WSM derived SH_{max} directions reflect measurement uncertainty or systematic changes in the stress field? Fracture SH_{max} on plane B provides the most robust FSP curve because of the consistency with the observed slip direction (Figure 4.3 with the focal mechanism) and the relatively small uncertainties from calculating in-situ SH_{max} direction compared to using WSM data. It is possible that the 45° strike corresponding to plane B represents the strike of en-echelon fractures that rupture on a larger scale en-echelon structure that strikes 73°, as determined from seismicity locations. Fracture SH_{max} is also only 9° from regional SH_{max} which is within its uncertainty. If we only had WSM data to calculate SH_{max} orientation, then regional SH_{max} on plane B provides the smallest uncertainty in additional pore pressure which is most consist with slip direction out of WSM derived data.

Differences in inferred fault stabilities from chosen SH_{max} length scale are the larger source of uncertainty compared to the chosen fault strike. The change in SH_{max} azimuth from regional to the closest measurements results in quite a large range of critical pore pressures. For example, choosing near SH_{max} compared to fracture SH_{max} using plane A with Method 2 results in a fault that is inferred to be 1.8 times more stable. In comparison, the chosen fault strike has little impact on fault stability; whether one chooses plane A or plane B, the threshold amount of additional pore pressure needed to cause failure is similar, for the same SH_{max} length scale. Therefore, in this case an ambiguity on the order of ~30° in the orientation of the fault has a relatively small impact on inferred fault stability.

Choosing Method 1 or 2 result in more significant differences in estimated fault stability than the chosen plane. For example, using Method 2 and near SH_{max} results in a fault stability 1.6 times larger compared to Method 1 whereas fault plane differences from Method 2 are more similar (Table 3.2). This discrepancy occurs because we have defined the critical pore pressure using Method 1 as the minimum pore pressure to failure within the full range of possible estimates, whereas Method 2 defines fault stability by the amount needed for a 33% chance of failure. Therefore Method 2 has mostly larger values.

Stress scenario	$\Delta P_{M1,A}$	$\Delta P_{M1,B}$	$\Delta P_{M2,A}$	$\Delta P_{M2,B}$	$\Delta P_{M2,A}/\Delta P_{M1,A}$	$\Delta P_{M2,A}/\Delta P_{M2,B}$
regional SH_{max}	13	13	15	16	1.2	0.9
local SH_{max}	13	13	15	15	1.2	1
near SH_{max}	13	13	20	15	1.6	1.3
closest SH_{max}	13	13	21	26	1.6	0.8
fracture SH_{max}	13	13	11	11	0.8	1.2

Table 4.2: Different estimates of the amount of additional pore pressure needed to cause failure from different SH_{max} azimuths and fault strikes. Each column represents a different scenario for calculating fault stability defined by the method and plane. Each row is a different SH_{max} scenario. $\Delta P_{M1,A}$ and $\Delta P_{M1,B}$ are results from Method 1 on planes A and B, respectively. $\Delta P_{M2,A}$ and $\Delta P_{M2,B}$ are the pore pressure perturbations needed for failure using Method 2 (i.e., probability of failure at 33% probability) on plane A and B, respectively. $\Delta P_{M2,A}/\Delta P_{M1,A}$ is the factor corresponding to the difference between the two methods used; $\Delta P_{M2,A}/\Delta P_{M2,B}$ is the factor difference between using the two planes and the same method. Values are all in MPa.

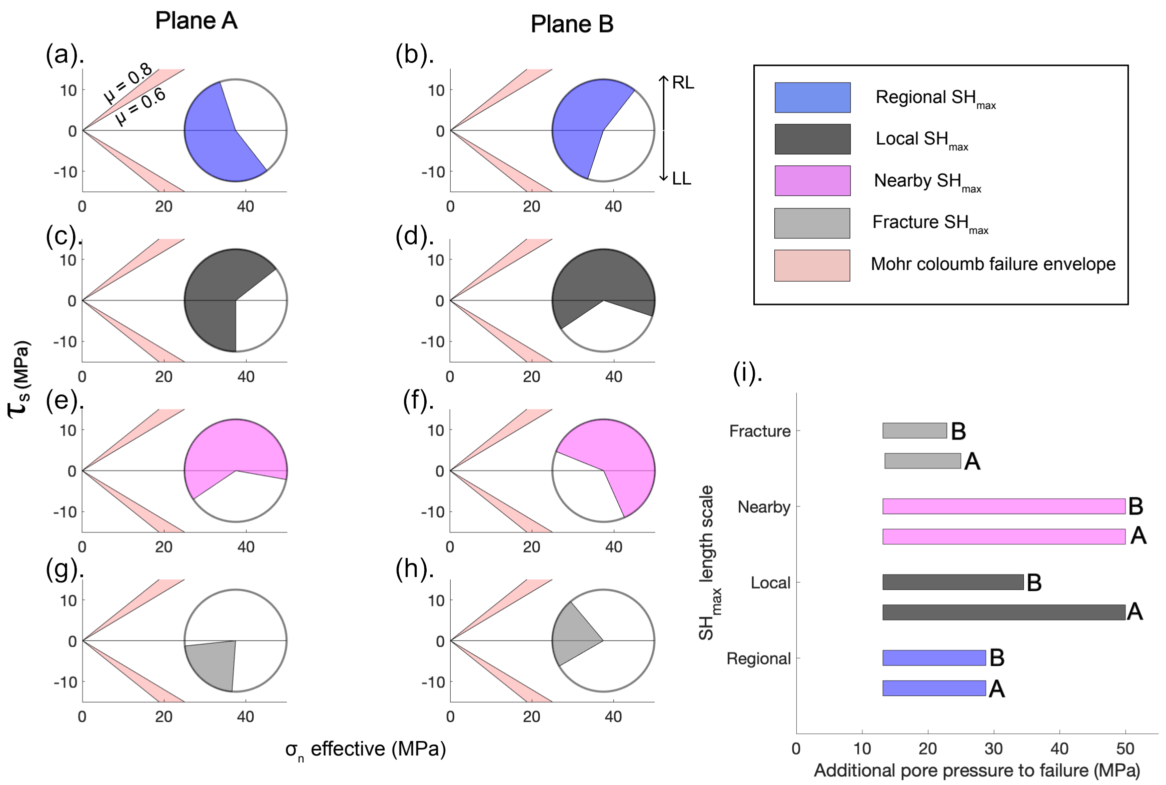

Figure 4.5: Description of 2D stress states and fault stability on plane A (73° strike) and B (45° strike) using Method 1. (a) The Mohr circles describing the range of stresses on planes with hydrostatic pore pressure. The first column corresponds to stresses on plane A and the second column represents plane B. Each coloured segment corresponds to an average SH_{max} orientation according to the length scale, as per legend. Hemisphere of right lateral slip is labelled as RL and indicated by upwards arrow. Hemisphere of left lateral slip is labelled as LL shown by downwards arrow. (b) Additional pore pressure needed to reach the failure point for each SH_{max} direction length scale. Each coloured segment corresponds to an SH_{max} length scale as per legend. Each bar is labelled according to the plane it represents.

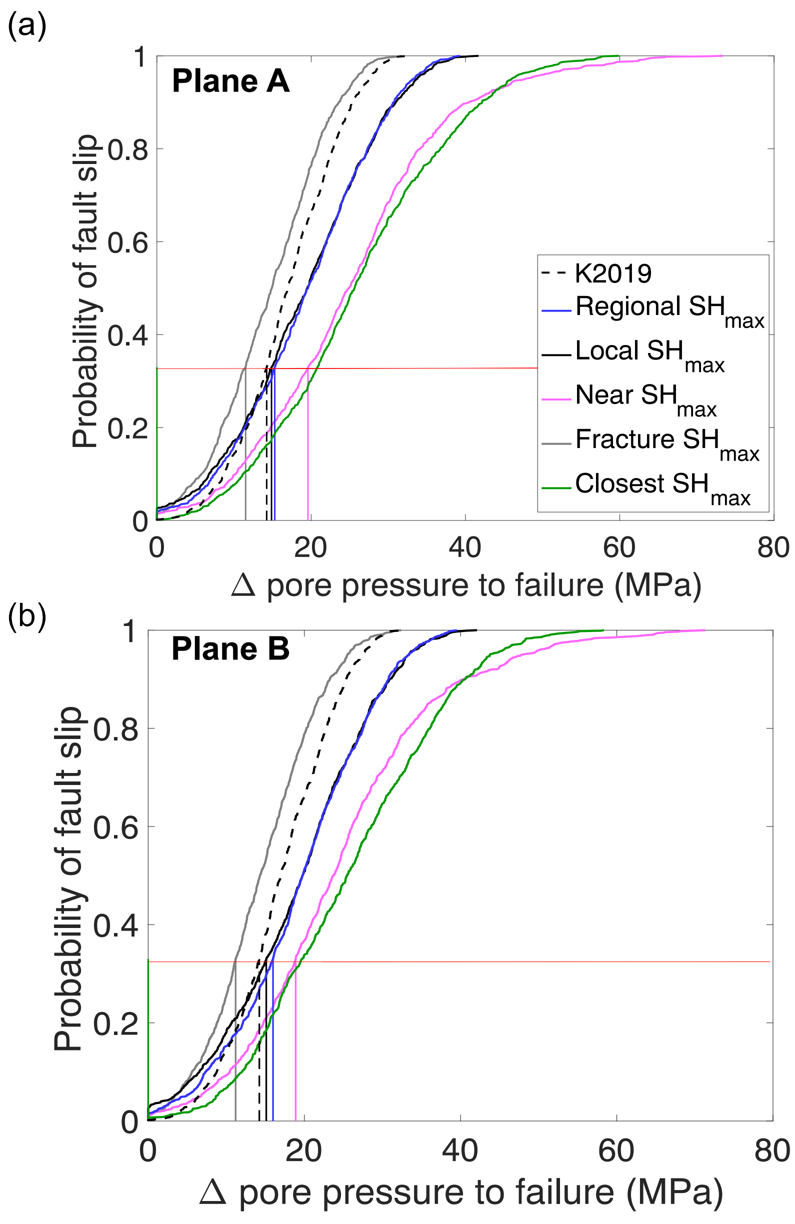

Figure 4.6: Probability of failure against additional pore pressure (FSP) for (a) plane A and (b) plane B. Each curve represents an SH_{max} direction, as per legend in (a). The curve corresponding to the same estimate by K2019 is shown as a black dashed line (70° strike and 55° SH_{max} direction). Vertical line projections onto the x-axis indicate the change in pore pressures corresponding to a 33% probability of fault slip, as used by Walsh and Zoback (2016), for each SH_{max} azimuth.

.

4.4 Discussion

When determining the stability of a fault structure, uncertainties linked to stress field orientation affect our ability to make accurate inferences. The FSP method, which has been used by some to characterise fault stability (Walsh and Zoback, 2016; Nantanoi et al., 2021; Kettlety et al., 2019; Hennings et al., 2021) suggests that critical additional pore pressure acts as an upper guiding limit for operators, below which it should be safe to perturb a reservoir. However, inferred stabilities largely depend on the SH_{max} direction length-scale one believes is acting on the analysed fault. Using near SH_{max} estimates results in pore pressures that are a factor of 1.8 more stable than if one were to choose fracture SH_{max}. The maximum critical additional pore pressure (26 MPa) from the SH_{max} length-scale azimuths (Table 3.2) is well within the range of well head pressures (up to 60 MPa) which means any of the critical thresholds are reasonable values to consider for fault reactivation. Thus, the large uncertainties of inferred fault stability means that WSM data provides poor constraints of how stable a fault is.

To assess whether fault stability estimates in another region are as sensitive to the stress field uncertainty as presented here, we calculate regional, local and nearby SH_{max}, and the associated uncertainties using the same methods for the Central U.S. This region is selected because it is used in another FSP study by Walsh and Zoback (2016). We assign the pad centre roughly on the major fault of the Pawnee sequence (Walsh and Zoback, 2016). For regional SH_{max} we obtain 74 ± 28°. For local SH_{max} we calculate an azimuth of 78± 10° and for Nearby SH_{max} we calculate an average SH_{max} direction of 81° ± 2°. The regional SH_{max} uncertainty is quite similar to the uncertainty calculated here but local SH_{max} has a significantly lower uncertainty of ± 10°, which means the large variation closer to the pad in the Horn River basin suggests a more heterogeneous stress field and/or larger measurement uncertainty compared to the stress field around the fault segment which hosted the Pawnee sequence. Thus FSP sensitivity is likely greater in the Horn River basin because of the larger heterogeneity/measurement uncertainty compared to the Central U.S., but the uncertainties in the Central U.S. are still quite large at the regional and local scale.

Our results suggest inferring fault stabilities within a region, from SH_{max} direction measurements at a specific point, may not be faithful to the uncertainty which arises from the heterogeneity within a stress field. Walsh and Zoback (2016) calculate SH_{max} orientations with a low uncertainty (i.e., 2-6°) using focal mechanism inversions and wellbore measurements compared to the regional (± 30°) and local SH_{max} uncertainty (± 22°) that we calculate using WSM data. Although the SH_{max} azimuth at the particular location of the major faults may be relatively well constrained, generalising the SH_{max} azimuth and the associated uncertainty to other faults in a larger geographical region could result in fault stabilities which are inferred as significantly more accurate than when the heterogeneity of the stress field is accounted for. As a result, uncertainty in fault stability increases.

Attempts have been made to model systematic variations of SH_{max} direction into FSP calculations for areas with a recognised stress rotation, such as the Delaware basin (Dvory and Zoback, 2021). Dvory and Zoback (2021) create a smoothed map of faults stabilities based on changing SH_{max} azimuth rather than assuming a certain value for the whole region. However, a smoothed map implies that the rotations are systematic and local irregularities are not necessarily accounted for. If the length scale of SH_{max} direction variation is smaller than the spacing between grid points used for creating a smoothed map then local irregularities will not be accounted for. Thus, smoothed stress maps might still provide significantly overconfident fault stability estimates.

In this study, the best constraints on additional pore pressure have additional uncertainties which we do not consider. Depth variations of SH_{max} orientation are especially prominent in active fault regions (e.g., Barton and Zoback, 1994). SH_{max} orientations are reported to change by 90° within very small depth spacing (i.e., <10 m) at the Cajon Pass borehole in California (Barton and Zoback, 1994). Such drastic rotations in the stress field may cause certain asperities to slip in different directions than predicted by the regional stress field. Therefore even along the same fault segment the SH_{max} orientation may change with depth, which affects inferences of fault stability on each asperity compared to the calculations which are usually assumed on a uniform plane. Another additional source of uncertainty is that sometimes the reactivated structure is not always observable in advance in 3D seismics (Kettlety and Verdon, 2021; Kettlety et al., 2021), especially if the slip mechanism is strike-slip. In this study the major reactivated structure is also not observable in 3D seismics.

In the absence of an in-situ measurement of SH_{max} direction the smaller uncertainty of regional SH_{max} on plane B provides an estimate of inferred fault stability which is both similar to fracture SH_{max} and consistent with the observed rake. By virtue of having more measurements, regional SH_{max} also has a smaller uncertainty. If the main reason for large SH_{max} azimuth uncertainties is due to measurement error then increasing the density of measurements and perhaps using standard error provides better constraints on fault stability. However, if the reason for SH_{max} azimuth variation is dominantly because of systematic local variations in the stress field (i.e., heterogeneous stress field) then the recommendation is to better establish the length scales that are causing systematic SH_{max} variation within a geographical region first. It would also be useful to have more site-specific measurements of in-situ SH_{max} azimuth at multiple depths in a reservoir, especially in the crystalline basement. Then we can better establish the length scale of heterogeneities that may exist and better constrain FSP calculations.

4.5 Conclusion

To mitigate felt seismicity during geo-energy operations it is desirable to accurately determine the stability of fault structures in advance of fluid injections that might reduce the effective stress and lead to failure. Here we use a compound focal mechanism and microseismicity, combined with WSM data to constrain the stability of a fault structure reactivated by microseismicity during hydraulic fracturing operations in the Horn River basin, Canada. By inputting these data and their uncertainty into a widely used fault slip potential model, we find that the large uncertainty in stress field orientation reduces our ability to provide useful constraints on fault stability. In-situ measurements of SH_{max} azimuth are best but in the absence of such measurements regional measurements are preferable compared to the large variance of more local measurements. Studies extrapolating stress field orientation from a particular point should be cautious about inferring stabilities of nearby faults, which could be significantly more stable or unstable than estimated. A denser sampling of SH_{max} azimuths could reduce the uncertainties in FSP calculations but a heterogeneous stress field hampers our ability to provide constraints on fault stability even if more data is obtained.

Chapter 5

Conclusions

In this thesis I probe the geomechanics and rupture physics of microseismicity induced by hydraulic fracturing in the Horn River basin, Canada. The provided dataset has a vast catalogue of seismicity locations, magnitudes and includes source parameter estimates by the contractor. I recalculate stress drops and examine the spatio-temporal variation of stress drop estimates to provide insight into the rupture physics of induced seismicity when high pressure fluids are injected into a reservoir (Chapter 2 and 3). However, stress drop observations are affected by compromising effects at high frequencies in the form of resonances and high frequency cut-offs (Chapter 2 and 3). The seismicity linked to a particular stage of injection (stage A14) illuminates a fault structure which I use to estimate the fault stability (i.e., the amount of additional pore fluid needed to cause Mohr-Coloumb frictional failure), as documented in Chapter 4. I analyse the sensitivities of inferred fault stability to fault geometry and principle stress direction which relates to the question of how confidently we can calculate fault stability. In this chapter I start by summarising the results in each of the previous science chapters (Chapters 2-4) and then provide the broader significance, future directions and recommendations for each of the themes presented in this thesis.

5.1 Summary of results

The central aim of Chapter 2 was to calculate stress drops of microseismic events. However, I observed issues in the high frequency spectra which significantly diminished both the quantity and quality of stress drop estimates I could calculate. I started by examining the pre-phase arrival spectral features of the noise which displayed unexpected and challenging features in the form of high frequency cut-offs and resonances. The resonances were not clearly removed by empirically correcting for attenuation in Chapter 3. By systematically considering previous observations of resonances along geophone borehole arrays I concluded that receiver side instrument effects are the most likely origin. The compromised high frequency signals affect our ability to constrain high frequency parameters and accurate crustal attenuation models. Using a sub-catalogue of selected events which were least affected by the effects I estimated a crustal attenuation model and stress drops of 90 microseismic events. The average stress drop lies in the range expected from tectonic earthquakes (i.e., 0.3-50 MPa - Allmann and Shearer (2009)), which supports the self-similar scaling of the rupture size relative to the amount of slip towards the microseismic scale. I interpret the observed scaling between stress drop and M_w in the dataset as an artefact introduced by the high frequency cut-off. These stress drops are likely lower estimates of what are larger values. I did not observe an increasing stress drop with depth (Hardebeck and Hauksson, 1997; Allmann and Shearer, 2007; Boyd et al., 2017) or distance from the point of injection (Pearson, 1981; Allmann et al., 2011; Kwiatek et al., 2014). In the case of slow diffusion through intact rock we may expect a signal of increasing stress drop near to the point of injection as differential stresses are relatively low (and therefore stress drop budget is lower) compared to a dryer environment farther away. Therefore I explain an independence of stress drop with injection distance by relatively quick diffusion of hydraulic fluid along a fault zone.

In Chapter 3 I used a more sophisticated approach of calculating stress drops, which builds upon results from Chapter 2. Similar to Chapter 2 I tested systematic changes of stress drop with distance from the injection point and further examined time variations of stress drop variations within clusters of highly similar and closely spaced events. I started by applying the spectral ratio method to determine corner frequencies of seismic events along the major fault structure. In line with other studies, stress drops using spectral ratios are on average larger compared to estimates from directly fitting source models. I observed no dependence of stress drop on distance from the point of injection. The lack of anti-correlation between stress drop and distance from the point of injection verifies observations from Chapter 2. Similar to Chapter 2, I still observed a scaling of stress drop with magnitude, which is likely caused by high frequency limits which persist into more sophisticated approaches when using such high frequency signals. Within clusters of highly cross-correlated and co-located events I did not observe an anti-correlation of stress drop with time and instead observed quite large variations. A larger stress drop event within a patch of closely spaced events could indicate a new rupture forming as a result of higher differential stress compared to existing patches which have already released some stress. Other possibilities that could explain the observation of a stress drop invariant to injection distance are that the large stress drop variations express the pore pressure variations within the fault structure, material differences along the fault, fault zone damage or the fault patch depth.

In Chapter 4, I focused on geomechanically characterising the chance of reactivating the major fault structure that extends into the crystalline basement. Although Kettlety et al. (2019) provide an estimate of the fault structure stability, I gleaned new insight from calculating a compound focal mechanism and considered sensitivities of inferred fault stabilities to World Stress Map (WSM) data - a natural resource to use for characterising the stress state in the crust. I started by calculating different estimates of the maximum principal stress direction by averaging measurements for 3 different length scales (750, 100 and 35 km) and the closest recording. Each of these measurements could reasonably be considered as representative of the in-situ stress state prior to the start of a subsurface geo-energy operation. Intra- and inter SH_{max} variances between estimates were quite significant and suggestive of systematic changes in the stress field and measurement uncertainty. Then I constrained the strike of the major fault structure using two methods: seismicity locations and a compound focal mechanism. Each method gave a different fault strike, and both were considered in further analysis. For a given strike, I used two methods to estimate the fault stability, both of which provided estimates of the amount of additional pore pressure required to reach Mohr-Coloumb frictional failure. Using both methods, I found that given the large uncertainties of additional pore pressures that could reasonably cause failure, inferences of fault stability are quite uninformative.

5.2 Overall findings and future work

5.2.1 Stress drops

The most robust direct fits and spectral ratios showed quite clearly that stress drop is invariant to distance from the point of injection, which is contrary to empirical observations by Pearson (1981) and Allmann et al. (2011). There are several reasons that can explain the differences with my observations. Firstly, the proposed mechanism may not be appropriate in all cases. Whilst there is good lab evidence that increasing confining pressures causes an increase in stress drop, to my knowledge it is still unclear whether increasing pore pressures is directly linked to a decreasing stress drop. Another possibility is that there is a signal of increasing stress drop, but the high frequency limiting effects observed in this study preclude such an observation.

Based on the Mohr-Coloumb explanation provided by Pearson (1981) and Allmann et al. (2011) the observation here could be explained by pore fluids diffusing in a shorter period (i.e., a few hours) over hundreds of metres along a fracture conduit compared to empirical case studies which report a growing stress drop form the injection point (e.g., Allmann et al., 2011). Compared to the this study, seismicity emerges more gradually along low permeability cataclastite features during the enhanced geothermal systems project in Basel (Häring et al., 2008). One possible explanation for observations in the Horn River basin is that the analysed structure is more dilated, allowing pore pressures to diffuse quicker over the same fault length compared to the structural features in Basel.

Other hydraulic fracturing projects exemplify the fracture corridors which are illuminated by seismicity and act as conduits for fluids. The Tony Creek dual Microseismic Experiment (ToC2ME) (Igonin et al., 2021) shows clusters of seismicity in the exploited shale which are most likely linked to fluid diffusion along existing fracture corridors (Igonin et al., 2021). In the Preston New Road (PNR) dataset (Verdon and Kettlety, 2020) fault zones are illuminated by hydraulic fracturing (Kettlety et al., 2020). One of the clearest structures extends 250 m from the injection point. Thus, the existence of clear fracture corridors for pore fluids to diffuse and reduce effective stresses is observed in other studies that analyse seismicity in tight shales. Compared to ToC2ME and PNR, in the Horn River basin, the clearest structure is seen in the underlying crystalline basement.

The absolute stress drops I calculated using both direct fits and spectral ratios generated values that are quite typical of tectonic seismicity. The similar stress drops imply that the amount of slip expected from tiny ruptures (i.e., $\leq$ 10 m) follows that expected from geometrical scaling of tectonic earthquakes. Considering that induced seismicity linked to geo-energy operations is typically hosted in shallower crust compared to tectonic seismicity, it is surprising to observe similar stress drops in this study to tectonic earthquakes.

The stress drop observations have implications on hazard. Shallow earthquakes might be expected to have lower stress drops (and therefore a lower frequency content) because seismicity is hosted in rocks with a lower crustal shear stress budget compared to deeper seismicity. Such interpretations have been used to explain low stress drops of micro-earthquakes in the Himalayas (Sharma and Wason, 1994). However, here we find that that shallow earthquakes do not display low stress drops (i.e., lower than 0.1 MPa). As ground motion prediction equations are a function of frequency, a higher frequency content (linked to larger than expected stress drops) affects hazard estimates.

The relatively similar stress drops to tectonic earthquakes may be explained by the focal mechanism. Most of the studied seismicity occurs within the limestone basement, which could be more likely to display double couple focal mechanisms compared to tensile microseisms linked to the opening of hydraulic fractures. Self-similar scaling of tectonic stress drops towards the microseismic scale may be more expected for double couple focal mechanisms because the rupture surface is more clearly defined, than for a tensile microseism. Thus, seismicity occurring within crystalline rock along re-activated structures may be more likely to display tectonic stress drops (and therefore have a higher frequency content) compared to the shallow in-zone seismicity within the shale. However, future studies need to conform this interpretation, which will require better monitoring of source parameters within shales.

In the studied dataset the rupture planes likely experienced elevated pore pressures, which is empirically linked to lower stress drops (Pearson, 1981; Allmann et al., 2011). Thus, the fact that I observed similar stress drops to tectonic seismicity from induced microseismic events in a fluid rich environment is quite unexpected. One explanation questions the assumption that deeper tectonic earthquakes must correspond to higher differential stresses. Increasing pore pressures at depth may prevent the build up of larger fault strength and result in similar differential stresses for deeper tectonic earthquakes. Empirical observations which suggested stress drop increased with depth are now mostly interpreted to be an artefact of attenuation modelling, revealing that stress drops are more likely to be stable with depth (Abercrombie, 2021).

The relative stress drop values within the studied dataset showed clear scaling between stress drop and M_w which is highly likely a direct consequence of high frequency limits - an effect long known to cause a scaling at the microseismic scale (Hanks, 1982; Ide and Beroza, 2001; Deichmann, 2017). Whilst I can not fully rule out a physical cause for the scaling, my results suggest that towards microseismic asperity sizes, the amount of slip proportionally decreases in accordance to geometrical scaling of rupture size.

Most empirical observations of stress drop variation within a fluid rich environment have relied only on an idealised Mohr-Coloumb framework for interpreting results (Pearson, 1981; Allmann et al., 2011). However, the competing effects of fault zone damage, geological material, localised pore pressure differences, as well as quasi-static effects (e.g., slow slip) also drive stress drop variation. Future work could significantly benefit from a lab controlled study which examines the competing effects on recorded stress drops. Such a controlled study would provide a useful reference to interpret the signals from datasets collected from subsurface geo-energy operations rather than referring only to the Mohr-Coloumb frictional framework. A closer analysis of stress drop driving effects may also help explain why microfractures may still generate tectonic stress drops.

5.2.2 Attenuation

The discrepancies between stress drops obtained in Chapter 2 and 3 might be explained by the assumption of intrinsic attenuation in Chapter 2. The empirical based method (Chapter 3) directly removes the effect of attenuation, whereas, in Chapter 2 I used a model based approach which assumes intrinsic attenuation is the dominant mechanism of amplitude decay. The stress drop discrepancies may therefore may explained by the discrepancies in how attenuation is accounted for; spectral ratios account for all forms of attenuation (i.e., intrinsic attenuation, geometrical spreading, scattering effects and high frequency cut-offs), whereas, stress drops calculated using model fits in Chapter 2 only consider intrinsic attenuation. As Q trades-off with corner frequency, and therefore stress drop, the unaccounted sources of attenuation in Chapter 2 may explain the lower stress drop.

In the processing stages of calculating stress drops, future studies will benefit from first establishing the attenuation more robustly using spectral ratios, perhaps from a handful of the largest events. Once an attenuation function is established, the Q function (and any high frequency additional effects) can be applied to model-fitting methods to calculate a larger catalogue of stress drops. This method allows one to exploit the dataset beyond the spectral ratio criteria (which restrict the number of events) and could prevent significant disparity in stress drops using two different methods.

5.2.3 Inferring fault stabilities

From this study it is quite clear that establishing the stability of major fault structures before a subsurface geo-energy operation is difficult when relying on WSM data alone. In this thesis I showed that the significant epistemic uncertainty from SH_{max} direction renders FSP estimates of fault stability quite uninformative. For other pads that lie within a sufficiently heterogeneous stress field I would expect to calculate similarly uncertain inferences of fault stability. As a comparison, the study area of Walsh and Zoback (2016) (Central U.S.) shows a less heterogeneous SH_{max} direction. Therefore fault slip potential estimates are likely to be better constrained in the Central U.S. compared to the Horn River basin, but estimates are still affected by measurement uncertainty. In the Delaware basin, significant SH_{max} direction rotations of ~150° from North to South are observed (Snee and Zoback, 2018). Therefore, if we rely on WSM data, we expect to observe significant uncertainties in fault stability estimates.

Before an operation (i.e., before any drilling), when no in-situ measurements of SH_{max} direction have been made, any FSP estimates are likely to be quite uninformative because of the large uncertainties of SH_{max} direction from WSM data and the other variables such as fault orientation (if the mechanism of failure is strike slip, no previous throw may show up in the 3D seismic). Once wells have been drilled and the in-situ tests or seismicity within the reservoir reveals the in-situ SH_{max} direction, the uncertainty of FSP estimates reduces as long as a previously identified fault is hosted within the stimulated rock mass. If a fault structure emerges in the basement or above the reservoir, there is no guarantee that the SH_{max} direction measured in the reservoir is representative of another geological formation due to small scale heterogeneities in the Earth (Schoenball and Davatzes, 2017; Luttrell and Hardebeck, 2021). More site specific measurements of SH_{max} direction over different length scales to account for any rotation could improve our ability to constrain the epistemic uncertainty of SH_{max} variation. A series of in-situ measurements, perhaps made along monitoring wells (for logistical ease), and if possible at least one measurement in the underlying basement rock, would provide a more robust estimate of SH_{max} direction and the epistemic uncertainty within a reservoir.

However, even if the epistemic uncertainties on parameters used in the FSP model are low, there are broader points that must be addressed to gain confidence when using FSP to calculate fault stabilities. FSP relies on a probabilistic Mohr-Coloumb framework of an idealistic plane which experiences equal pore pressure increase. However, this approximation neglects the reality of fault zones, which, as illuminated through microsesimicity on reactivated fault structures, is more likely a series of asperities that might connect to form a larger rupture plane. FSP may be more useful for smooth fault planes which can approximate a single plane, and may explain the success of FSP on the mapped faults of the Pawnee sequence (Walsh and Zoback, 2016). However, a collection of asperities which do not clearly link to form a main fault rupture plane, may not be appropriate for FSP analysis. A controlled lab experiment which investigates how FSP performs on samples using a single, smooth cut plane (as close to idealistic as possible) and a sample with multiple asperities, would be informative.

5.2.4 Resonances

The high frequency resonances I reported significantly limited the phase arrivals and stations that I considered for constraining crustal attenuation and for fitting source models because the spectral shape was significantly distorted from the expected source model shape. The severity of resonances systematically increases towards deeper stations, and it is likely that the resonances are related to activation of spurious instrument frequencies and/or coupling issues, but may also be due to near-receiver effects.

Resonances that arise during hydraulic fracturing treatment when using geophone arrays are a recognised feature (Maxwell, 2014). As a comparison, the PNR dataset (Clarke et al., 2019) also displays resonances (Holmgren et al., 2020). Tube waves are observed, and higher frequencies (suspected instrument resonances) appear to decrease in strength with time in some frequency intervals (J. Holmgren, pers. comm.). Another example is from the Rolla Microseismic Experiment in Canada, where resonances are identified as a source effect from fluid filled cracks or fluid flow (Tary et al., 2014).

To improve the recording potential of geophone arrays it is useful to better understand the provenance of the resonances within this dataset. It is still unclear to what extent resonances are amplifications of existing background resonances or new features which arise upon a phase arrival. It is also unclear what the nature of the continuous resonance features are and if these features arise from mechanical/tool effects or are a result of other effects. By analysing how the spectral signal of the resonances appear on each component, and how the strength of the signals change with time for each station along a geophone array, we may better understand the nature of the resonances and help better characterise them.

Another way to better characterise the resonances is to use machine learning. Rather than relying on qualitative observations, by applying machine learning techniques we may be able to better classify the type of resonance. The signals arising from possible sources (e.g, tube waves, pumping, fluid filled cracks, etc.) could be characterised and then used as a template for other datasets, similar to methods applied when identifying phase arrivals using machine learning (Ross et al., 2018).

A cross-study examination of the resonances identified within other hydraulic fracturing datasets would be a useful reference for better characterisation of featres. There have been many studies which have analysed the effect of resonances (e.g., Sun and McMechan, 1988; Faber and Maxwell, 1997; Pettitt et al., 2009; Tary et al., 2014; Zhang et al., 2018). A comprehensive empirical documentation of the frequency bandwidth, instrument type, resonance type and recommended identification procedure could be useful reference for others to help identify resonances observed for a particular dataset.

5.2.5 Instrument setup

One of the major problems of calculating high frequency source parameters from microseismic signals is that even if geophone recording frequencies extend significantly above the dominant earthquake signal and are positioned close to the events, the severe attenuating effects experienced by microseismic signals are difficult to account for. As a result the number of seismic events that can be used to constrain stress drops significantly diminishes.

The severity of high frequency cut-offs increases with station depth along both the borehole arrays monitored. Future research would benefit from better understanding the systematic trends and the provenance of the severely attenuating effects I observed in this thesis. The deeper geophones in this study are closer to the microseismic cloud and it is quite possible that the increased fracture density causes more severe attenuation towards deeper stations, in which case the geophone array might be better positioned farther away from the top of the microseismic cloud. However, as geophones are placed farther from the seismic sources, the ability to resolve higher frequencies decreases. The number of events that can be detected also decreases when geophones are placed farther away from seismic events.

Including an array of shallow buried broadband sensors could significantly improve the ability to better constrain structural features and offers better constraint of attenuation/source parameters. Shallower broadband sensors allow: the body waves to separate out in time more, which allows an increase in the frequency resolution of spectra; additional constraints of the attenuation within the rock mass hosting the geophones and the near surface; better constraints of the strike ambiguity (in this study) of the major structure because of wider azimuthal coverage, which could improve estimates of fault stability. However, broadband sensors do not typically have Nyquist frequencies that go beyond the dominant frequencies of microseismic events (i.e., >100 Hz), and do not have the stacking capability of geophone arrays.

To suppress the effect of resonances, specific bandwidth filters could be applied. However, this relies on first knowing at what frequencies the resonances manifest, and also must assume that the resonances are a ubiquitous feature for all events, which depends on the resonance provenance; it may be the case that some phase arrivals do not require any filtering for resonances.

For mitigating seismic hazard stress drop is unlikely to be a useful parameter using the conventional geophone setup deployed here because of the paucity of measurements that can be accurately calculated in real-time and the inherently large model uncertainties. DAS (Distributed Acoustic sensing) could be a useful compliment to current microseismic monitoring practices. Whilst there are still some challenges in converting strain/strain-rates (as recorded by DAS cables) to displacements for source parameter estimation (Lior et al., 2021), the potential for high density sampling of the wavefield could improve our ability to determine accurate source parameter estimates from induced miroseismicity.

APPENDIX A

APPENDIX A

This appendix contains the supplementary figures for Chapter 2 of this thesis.

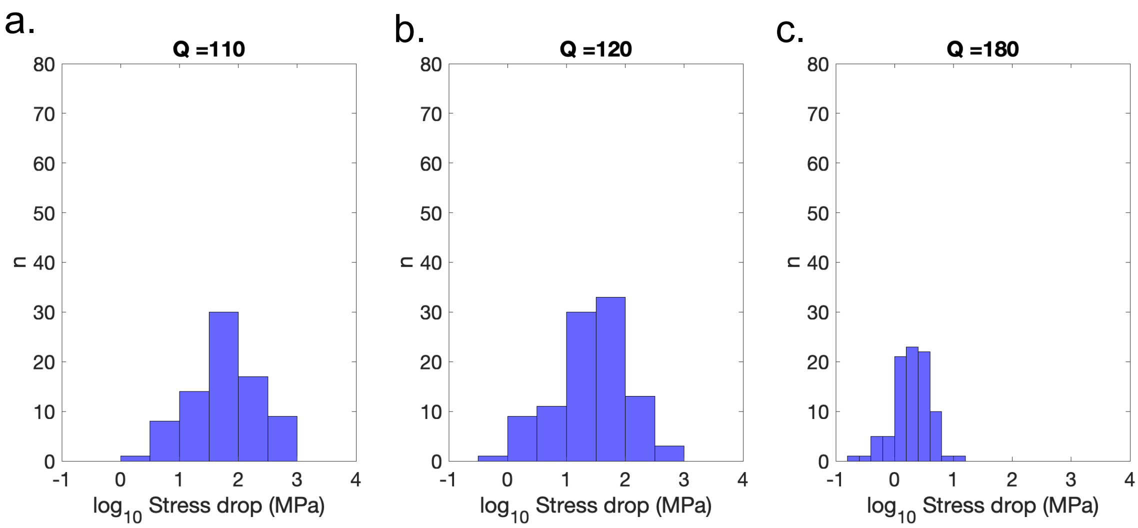

Figure A.1: Histograms of stress drop estimates for the three crustal attenuation models we consider. (a) Q = 110 (b) Q = 120 and (c) Q = 180.

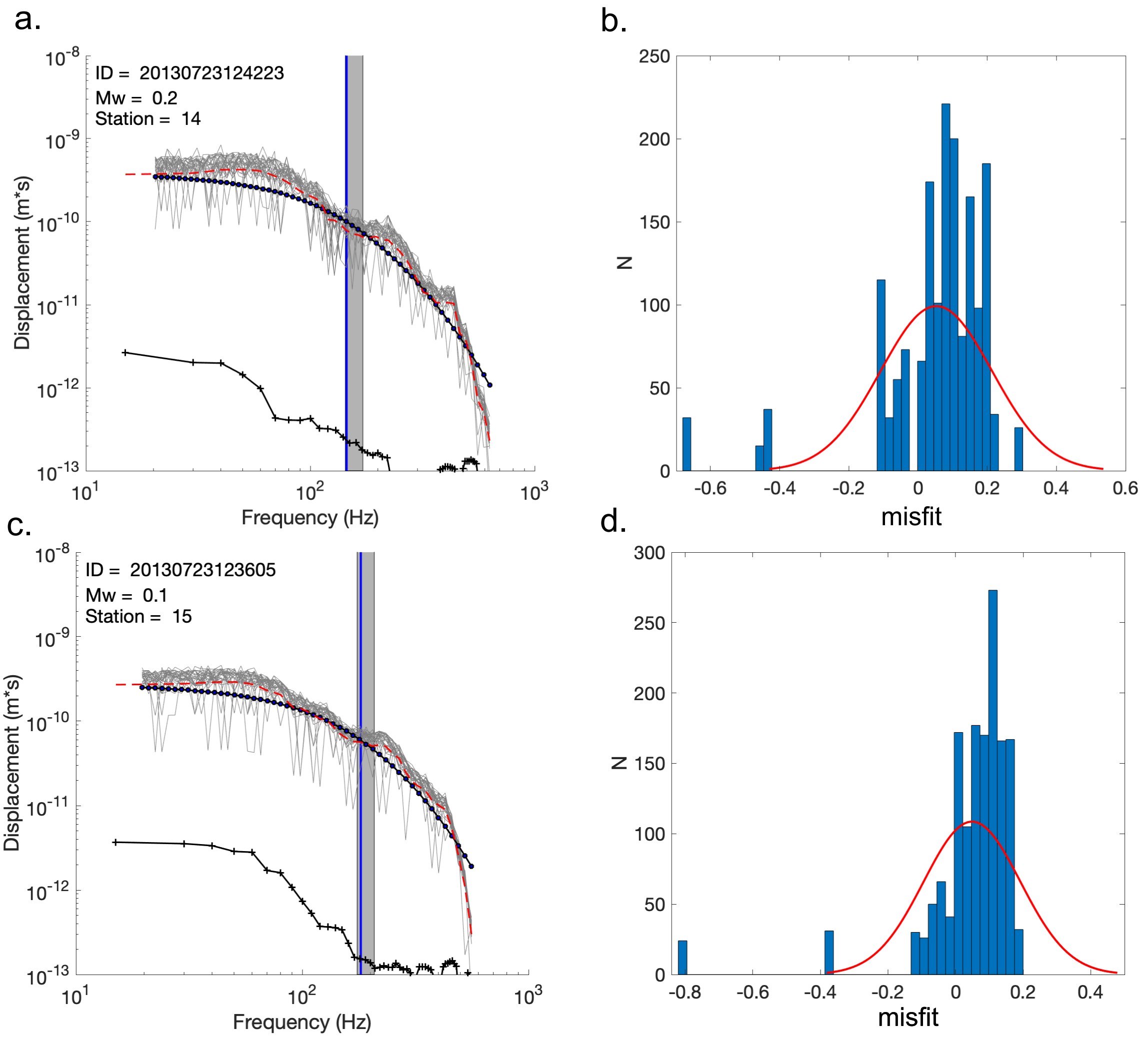

Figure A.2: Demonstration of observed spectra, model fits and synthetic spectra from bootstrapping, from 2 example events. The corresponding histograms of residuals and modelled Gaussian distributions are shown in (b) and (d), for (a) and (c), respectively. (a and c) Displacement-amplitude spectra where red dashed lines shows the P-phase arrival. The black solid line shows the best model fit (circles showing the log spaced sample points for inversion) and the corresponding corner frequency is shown by a blue vertical line. Grey lines show the synthetic spectra from bootstrapping and the range of bootstrapped corner frequencies is shown by the grey patch. The black solid line shows the pre-event noise, where multi-taper sample points are marked by a tick.

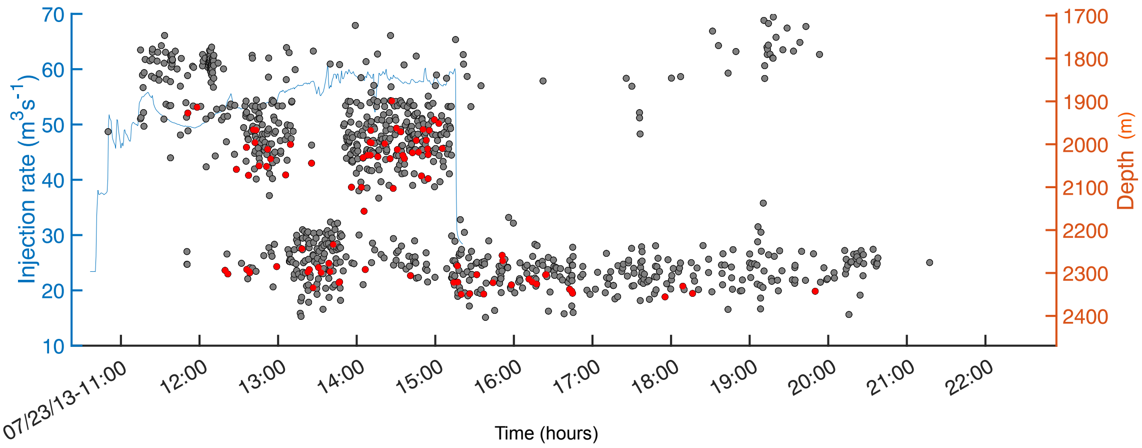

Figure A.3: Injection rate and depth of seismic events against time in hours for events during and just after injection into stage A14. Each seismic event is shown by a circle corresponding to the depth (right y-axis). Grey circles show all seismic events recorded by the contractor and red circle show events used in this study. Blue line shows injection rate corresponding to stage A14 (left-y axis).

natbib

Bibliography

Abercrombie, R., Leary, P., 1993.
Source parameters of small earthquakes recorded at 2.5 km depth, cajon pass, southern california: implications for earthquake scaling.
Geophysical Research Letters 20, 1511–1514.

Abercrombie, R.E., 1995.
Earthquake source scaling relationships from -1 to 5 using seismograms recorded at 2.5-km depth.
Journal of Geophysical Research 100, 24015–24036.

Abercrombie, R.E., 1997.
Near-surface attenuation and site effects from comparison of surface and deep borehole recordings.
Bulletin of the Seismological Society of America 87, 731–744.

Abercrombie, R.E., 1998.
A summary of attenuation measurements from borehole recordings of earthquakes: The 10 Hz transition problem.
Pure and Applied Geophysics 153, 475–487.

Abercrombie, R.E., 2015.
Investigating uncertainties in empirical Green's function analusis of earthquake source parameters.
Journal of Geophysical Research: Solid Earth 120, 4263–4277.
doi:`10.1002/2015JB012608.Received`.

Abercrombie, R.E., 2021.
Resolution and uncertainties in estimates of earthquake stress drop and energy release. volume 379.
doi:`10.1098/rsta.2020.0131`.

Adams, J., Eccles, D., 2002.
Controls on Fluid Flow Systems in Northern Alberta as Related to MVT Mineralization: A Contribution to the Carbonate-Hosted Pb-Zn (MVT) Targeted Geoscience Initiative Alberta.

EUB/AGS Geo-Note .

Ader, T., Chendorain, M., Free, M., Saarno, T., Heikkinen, P., Malin, P.E., Leary, P., Kwiatek, G., Dresen, G., Bluemle, F., Vuorinen, T., 2020.
Design and implementation of a traffic light system for deep geothermal well stimulation in Finland.
Journal of Seismology 24, 991–1014.
doi:10.1007/s10950-019-09853-y.

Aki, K., 1967.
Scaling Law of Seismic Spectrum.
Journal of Geophysical Research 72, 1217–1231.

Aki, K., Fehler, M., Das, S., 1977.
Source mechanism of volcanic tremor: Fluid-driven crack models and their application to the 1963 kilauea eruption.
Journal of volcanology and geothermal research 2, 259–287.

Aki, K., Richards, P.G., 2002.
Quantitative Seismology .

Allen, M.J., Kettlety, T., Faulkner, D.R., Kendall, J.M., De Paola, N., 2021.
Frictional properties of a faulted shale gas play: implications for induced seismicity, in: EGU General Assembly Conference Abstracts, pp. EGU21–12764.

Allen, R.V., 1978.
Automatic earthquake recognition and timing from single traces.
Bulletin of the Seismological Society of America 68, 1521–1532.

Allmann, B.P., Shearer, P.M., 2007.
Spatial and temporal stress drop variations in small earthquakes near Parkfield, California.
Journal of Geophysical Research: Solid Earth 112, 1–17.
doi:10.1029/2006JB004395.

Allmann, B.P., Shearer, P.M., 2009.
Global variations of stress drop for moderate to large earthquakes.
Journal of Geophysical Research: Solid Earth 114, 1–22.
doi:10.1029/2008JB005821.

Allmann, B.P.G., Goertz, A., Wiemer, S., 2011.
Stress drop variations of induced earthquakes at the Basel geothermal site.
Geophysical Research Letters 38, 1–5.
doi:10.1029/2011GL047498.

Anderson, E.M., 1905.
The dynamics of faulting.
Transactions of the Edinburgh Geological Society 8, 387–402.

Anderson, J.G., 1986.
Implication of attenuation for studies of the earthquake source.
Earthquake Source Mechanics 37, 311–318.

Anderson, J.G., Hough, S.E., 1984.
A model for the shape of the fourier amplitude spectrum of acceleration at high frequencies.
Bulletin of the Seismological Society of America 74, 1969–1993.

Archuleta, R.J., Cranswick, E., Mueller, C., Spudich, P., 1982.
Source Parameters of the 1980 Mammoth Lakes, California, Earthquake Sequence.
Journal of Geophysical Research 87, 4595–4607.

Baig, A., Urbancic, T., Viegas, G., Karimi, S., 2012.
Can small events (mw <0) observed during hydraulic fracture stimulations initiate large events (mw >0)?
The Leading Edge 31, 1470–1474.

Baird, A.F., Kendall, J.M., Fisher, Q.J., Budge, J., 2017.
The Role of Texture, Cracks, and Fractures in Highly Anisotropic Shales.
Journal of Geophysical Research: Solid Earth 122, 10,341–10,351.
doi:10.1002/2017JB014710.

Bao, X., Eaton, D.W., 2016.
Fault activation by hydraulic fracturing in western Canada.
Science 354, 1406–1409.
URL: http://www.sciencemag.org/lookup/doi/10.1126/science.aag2583, doi:10.1126/science.aag2583, arXiv:arXiv:1011.1669v3.

Barker, J., 2014.
Horn River Basin - Unconventional Shale Gas Play Atlas .

Barton, C.A., Zoback, M.D., 1994.
Stress perturbations associated with active faults penetrated by boreholes: Possible evidence for near-complete stress drop and a new technique for stress magnitude measurement.
99, 9373–9390.
doi:10.1029/93JB03359.

Bedford, J.D., Faulkner, D.R., Lapusta, N., 2022.
Fault rock heterogeneity can produce fault weakness and reduce fault stability.

Nature Communications 13, 1–7.
doi:10.1038/s41467-022-27998-2.

Bell, J.S., 2015.
In situ stress orientations and magnitudes in the Liard Basin of Western Canada.
Geological Survey of Canada OpenFile70, 1–410.
doi:10.4095/295742.

Bethmann, F., Deichmann, N., Mai, P.M., 2012.
Seismic wave attenuation from borehole and surface records in the top 2.5km beneath the city of Basel, Switzerland.
Geophysical Journal International 190, 1257–1270.
doi:10.1111/j.1365-246X.2012.05555.x.

Boatwright, J., 1978.
Detailed spectral analysis of two small new york state earthquakes.
Bulletin of the Seismological Society of America 68, 1117–1131.

Boatwright, J., 1980.
A specteal theory for circular sesimic sources.
Bulletin of the Seismological Society of America 70, 1–27.

Boitz, N., Reshetnikov, A., Shapiro, S.A., 2018.
Visualizing effects of anisotropy on seismic moments and their potency-tensor isotropic equivalent.
Geophysics 83, C85–C97.

Boyd, O.S., McNamara, D.E., Hartzell, S., Choy, G., 2017.
Influence of Lithostatic Stress on Earthquake Stress Drops in North America.
Bulletin of the Seismological Society of America 107, 856–868.
URL: https://doi.org/10.1785/0120160219, doi:10.1785/0120160219,
arXiv:https://pubs.geoscienceworld.org/ssa/bssa/article-pdf/107/2/856/4149646/bssa-20162

Brune, J.N., 1970.
Tectonic Stress and the Spectra of Seismic Shear Waves from Earthquakes.
Journal of Geophysical Research 75, 4997–5009.

Butcher, A., 2018.
Microseismology : Characteristics , Magnitudes and Shallow Crustal Effects .

Butcher, A., Luckett, R., Kendall, J.M., Baptie, B., 2020.
Seismic magnitudes, corner frequencies, and microseismicity: Using ambient noise to correct for high-frequency attenuation.

Bulletin of the Seismological Society of America 110, 1260–1275.

Byerlee, J., 1978.
Friction of rocks.
Pure and Applied Geophysics PAGEOPH 116, 615–626.
doi:10.1007/BF00876528.

Byerlee, J.D., 1968.
Stick Slip, Stable Sliding, and Earthquakes. Effect of Rock Type, Pressure, Strain Rate, and Stiffness.
J Geophysical Research 73, 6031–6037.
doi:10.1029/jb073i018p06031.

Carafa, M.M., Barba, S., 2013.
The stress field in Europe: Optimal orientations with confidence limits.
Geophysical Journal International 193, 531–548.
doi:10.1093/gji/ggt024.

Carstens, P., 2019.
Science for Clean Energy Model for Fluid Migration in the Sub-surface , 1–52.

Catalli, F., Meier, M.A., Wiemer, S., 2013.
The role of Coulomb stress changes for injection-induced seismicity: The Basel enhanced geothermal system.
Geophysical Research Letters 40, 72–77.
doi:10.1029/2012GL054147.

Chou, Q., Gao, J., Somerwil, M., 2011.
Analysis of geomechanical data for horn river basin gas shales, ne british columbia, canada, in: SPE Middle East Unconventional Gas Conference and Exhibition, OnePetro.

Cieślik, J., 2015.
Stress Drop as a Result of Splitting, Brittle and Transitional Faulting of Rock Samples in Uniaxial and Triaxial Compression Tests.
Studia Geotechnica et Mechanica 37, 17–23.
doi:10.1515/sgem-2015-0003.

Clarke, H., Eisner, L., Styles, P., Turner, P., 2014.
Felt seismicity associated with shale gas hydraulic fracturing: The first documented example in Europe.
Geophysical Research Letters 41, 8308–8314.
doi:10.1002/2014GL062047.

Clarke, H., Verdon, J.P., Kettlety, T., Baird, A.F., Kendall, J.M., 2019.
Real-time imaging, forecasting, and management of human-induced seismicity at Preston new road, Lancashire, England.
Seismological Research Letters 90, 1902–1915.
doi:10.1785/0220190110.

Clerc, F., Harrington, R.M., Liu, Y., Gu, Y.J., 2016.
Stress drop estimates and hypocenter relocations of induced seismicity near Crooked Lake, Alberta.
Geophysical Research Letters 43, 6942–6951.
doi:10.1002/2016GL069800.

Cochran, E.S., Skoumal, R.J., McPhillips, D., Ross, Z.E., Keranen, K.M., 2020.
Activation of optimally and unfavourably oriented faults in a uniform local stress field during the 2011 prague, oklahoma, sequence.
Geophysical Journal International 222, 153–168.

Deichmann, N., 2017.
Theoretical basis for the observed break in ML/MW scaling between small and large earthquakes.
Bulletin of the Seismological Society of America 107, 505–520.
doi:10.1785/0120160318.

Deichmann, N., Giardini, D., 2009.
Earthquakes Induced by the stimulation of an enhanced geothermal system below Basel (Switzerland).
Seismological Research Letters 80, 784–798.
doi:10.1785/gssrl.80.5.784.

Deng, K., Liu, Y., Harrington, R.M., 2016.
Poroelastic stress triggering of the December 2013 Crooked Lake, Alberta, induced seismicity sequence.
Geophysical Research Letters 43, 8482–8491.
doi:10.1002/2016GL070421.

Dvory, N.Z., Zoback, M.D., 2021.
Assessing Fault Slip Potential in a Continuously Varying Stress Field - Application in the Delaware Basin.
ARMA-2021-2025.

D'Errico, J., 2012.
Fminsearchbnd, fminsearchcon.

Eaton, D.W., van der Baan, M., Birkelo, B., Tary, J.B., 2014. Scaling relations and spectral characteristics of tensile microseisms: Evidence for opening/closing cracks during hydraulic fracturing. Geophysical Journal International 196, 1844–1857. doi:10.1093/gji/ggt498.

Eaton, D.W., Igonin, N., Poulin, A., Weir, R., Zhang, H., Pellegrino, S., Rodriguez, G., 2018. Induced seismicity characterization during hydraulic-fracture monitoring with a shallow-wellbore geophone array and broadband sensors. Seismological Research Letters 89, 1641–1651. doi:10.1785/0220180055.

Edwards, B., Kraft, T., Cauzzi, C., Kästli, P., Wiemer, S., 2015. Seismic monitoring and analysis of deep geothermal projects in st Gallen and Basel, Switzerland. Geophysical Journal International 201, 1022–1039. doi:10.1093/gji/ggv059.

Ellsworth, W.L., 2013. Injection-Induced Earthquakes. Science 341, 1–8.

Ellsworth, W.L., Giardini, D., Townend, J., Ge, S., Shimamoto, T., 2019. Triggering of the Pohang, Korea, Earthquake (Mw 5.5) by enhanced geothermal system stimulation. Seismological Research Letters 90, 1844–1858. doi:10.1785/0220190102.

van der Elst, N.J., Page, T., Weiser, D.A., Goebel, T.H., Hoesseini, S., 2016. Induced earthquake magnitudes are as large as (statistically) expected. Journal of Geophysical Research: Solid Earth , 3782–3803doi:10.1002/2015JB012608.Received.

Eshelby, J.D., 1957. The determination of the elastic field of an ellipsoidal inclusion, and related problems. Proceedings of the Royal Society of London. Series A, Mathematical and Physical Sciences 241, 376–396.

Ester, M., Kriegel, H.P., Sander, J., Xu, X., 1996. A density-based algorithm for discovering clusters in large spatial databases with noise, AAAI Press. pp. 226–231.

Evans, D.M., 1966.
The Denver Area Earthquakes and the Rocky Mountain Arsenal Disposal Well.
Mt.Geology , 25–32.

Eyre, T., Zecevic, M., Salvage, R., Eaton, D., 2020.
A Long-Lived Swarm of Hydraulic Fracturing-Induced Seismicity Provides Evidence for Aseismic Slip.
Bulletin of the Seismological Society of America , 1–11.

Eyre, T.S., Eaton, D.W., Garagash, D.I., Zecevic, M., Venieri, M., Weir, R., Lawton, D.C., 2019.
The role of aseismic slip in hydraulic fracturing–induced seismicity.
Science Advances 5, 1–11.
doi:10.1126/sciadv.aav7172.

Faber, K., Maxwell, P.W., 1997.
Geophone spurious frequency: What is it and how does it affect seismic data quality?
Canadian Journal of Exploiration Geophysics 33, 46–54.
doi:10.1190/1.1826773.

Fornasini, P., 2008.
The uncertainty in physical measurements: an introduction to data analysis in the physics laboratory.
Springer Science & Business Media.

Foulger, G.R., Wilson, M.P., Gluyas, J.G., Julian, B.R., Davies, R.J., 2018.
Global review of human-induced earthquakes.
Earth-Science Reviews 178, 438–514.

Gaiser, J.E., Fulp, T.J., Petermann, S.G., Karner, G.M., 1988.
Vertical seismic profile sonde coupling.
Geophysics 53, 206–214.

Goebel, T., Weingarten, M., Chen, X., Haffener, J., Brodsky, E., 2017.
The 2016 mw5. 1 fairview, oklahoma earthquakes: Evidence for long-range poroelastic triggering at> 40 km from fluid disposal wells.
Earth and Planetary Science Letters 472, 50–61.

Goebel, T.H., Hauksson, E., Shearer, P.M., Ampuero, J.P., 2015.
Stress-drop heterogeneity within tectonically complex regions: A case study of San Gorgonio Pass, southern California.
Geophysical Journal International 202, 514–528.
doi:10.1093/gji/ggv160.

Goebel, T.H.W., Brodsky, E.E., 2018.
The spatial footprint of injection wells in a global compilation of induced earthquake sequences.
Science 361, 899–904.
URL: https://science.sciencemag.org/content/361/6405/899, doi:10.1126/science.aat5449.

Gubbins, D., 2005.
Time Series Analysis and Inverse Theory for Geophysicists.
Technometrics 47, 374.
doi:10.1198/tech.2005.s291.

Gudmundsson, A., Simmenes, T.H., Larsen, B., Philipp, S.L., 2010.
Effects of internal structure and local stresses on fracture propagation, deflection, and arrest in fault zones.
Journal of Structural Geology 32, 1643–1655.
URL: https://www.sciencedirect.com/science/article/pii/S0191814109001916, doi:https://doi.org/10.1016/j.jsg.2009.08.013. fault Zones.

Guglielmi, Y., Cappa, F., Avouac, J.P., Henry, P., Elsworth, D., 2015.
Seismicity triggered by fluid injection-induced aseismic slip.
Science 348, 1224–1226.
doi:10.1126/science.aab0476.

Haldorsen, J.B., Johnson, D.L., Plona, T., Sinha, B., Valero, H.P., Winkler, K., 2006.
Borehole acoustic waves.
Oilfield review 18, 34–43.

Hanks, B.Y.T.C., 1982.
Fmax 72, 1867–1879.

Hanks, T.C., Kanamori, H., 1979.
A moment magnitude scale.
Journal of Geophysical Research: Solid Earth 84, 2348–2350.
doi:10.1029/JB084iB05p02348.

Hardebeck, J.L., Hauksson, E., 1997.
Static stress drop in the 1994 Northridge, California, aftershock sequence.
Bulletin of the Seismological Society of America 87, 1495–1501.
doi:10.1785/bssa0870061495.

Häring, M.O., Schanz, U., Ladner, F., Dyer, B.C., 2008.
Characterisation of the Basel 1 enhanced geothermal system.

Geothermics 37, 469–495. doi:10.1016/j.geothermics.2008.06.002.

Harrington, R.M., Kwiatek, G., Moran, S.C., 2015. Self-similar rupture implied by scaling properties of volcanic earthquakes occurring during the 2004-2008 eruption of Mount St. Helens, Washington. Journal of Geophysical Research: Solid Earth 120, 4966–4982. doi:10.1002/2014JB011744.

Healy, D., Hicks, S.P., 2021. De-risking the energy transition by quantifying the uncertainties in fault stability .

Heidbach, O., Rajabi, M., Reiter, Karsten, a.Z.M., 2016. World Stress Map Database Release 2016. V. 1.1. GFZ Data Services doi:https://doi.org/10.5880/WSM.2016.001.

Heidbach, O., Reinecker, J., Tingay, M., Müller, B., Sperner, B., Fuchs, K., Wenzel, F., 2007. Plate boundary forces are not enough: Second- and third-order stress patterns highlighted in the World Stress Map database. Tectonics 26, 1–19. doi:10.1029/2007TC002133.

Hennings, P.H., Nicot, J.P., Gao, R.S., DeShon, H.R., Lund Snee, J.E., Morris, A.P., Brudzinski, M.R., Horne, E.A., Breton, C., 2021. Pore Pressure Threshold and Fault Slip Potential for Induced Earthquakes in the Dallas-Fort Worth Area of North Central Texas. Geophysical Research Letters 48, 1–9. doi:10.1029/2021GL093564.

Hennings, P.H., Snee, J.E.L., Osmond, J.L., Deshon, H.R., Dommisse, R., Horne, E., Lemons, C., Zoback, M.D., 2019. Injection-induced seismicity and fault-slip potential in the fort worth basin, Texas. Bulletin of the Seismological Society of America 109, 1615–1634. doi:10.1785/0120190017.

Hiramatsu, Y., Yamanaka, H., Tadokoro, K., Nishigami, K., Ohmi, S., 2002. Scaling law between corner frequency and seismic moment of microearthquakes: Is the breakdown of the cube law a nature of earthquakes? Geophysical Research Letters 29, 52–1–52–4. doi:10.1029/2001gl013894.

Holmgren, J., Werner, M.J., Baptie, B., 2020.

Contaminated High-Frequency Data in Borehole Geophones from Induced Seismicity in the UK, in: AGU Fall Meeting Abstracts, pp. S011–0014.

Holmgren, J.M., Atkinson, G.M., Ghofrani, H., 2019.
Stress drops and directivity of induced earthquakes in the western Canada sedimentary basin.
Bulletin of the Seismological Society of America 109, 1635–1652.
doi:10.1785/0120190035.

Holmgren, J.M., Werner, M.J., 2021.
Raspberry Shake Instruments Provide Initial Ground-Motion Assessment of the Induced Seismicity at the United Downs Deep Geothermal Power Project in Cornwall, United Kingdom.
The Seismic Record 1, 27–34.
doi:10.1785/0320210010.

Hough, S.E., 2014.
Short Note Shaking from Injection-Induced Earthquakes in the Central and Eastern United States 104, 2619–2626.
doi:10.1785/0120140099.

Hua, W., Chen, Z., Zheng, S., 2013.
Source Parameters and Scaling Relations for Reservoir Induced Seismicity in the Longtan Reservoir Area.
Pure and Applied Geophysics 170, 767–783.
doi:10.1007/s00024-012-0459-7.

Huang, Y., Beroza, G.C., Ellsworth, W.L., 2016.
Stress drop estimates of potentially induced earthquakes in the Guy-Greenbrier sequence.
Journal of Geophysical Research 121, 6597–6607.
doi:10.1002/2016JB013067.Received.

Huang, Y., Ellsworth, W.L., Beroza, G.C., 2017.
Stress drops of induced and tectonic earthquakes in the central United States are indistinguishable.
Science Advances 3, 1–7.

Hurd, O., Zoback, M., 2012.
Stimulated shale volume characterization: Multiwell case study from the horn river shale: I. geomechanics and microseismicity All Days.
URL: https://doi.org/10.2118/159536-MS, doi:10.2118/159536-MS. sPE-159536-MS.

Ide, S., Beroza, G.C., 2001.
Does apparent stress vary with earthquake size?
Geophysical Research Letters 28, 3349–3352.

Ide, S., Beroza, G.C., Prejean, S.G., Ellsworth, W.L., 2003.
Apparent break in earthquake scaling due to path and site effects on deep borehole recordings.
Journal of Geophysical Research: Solid Earth 108.
URL: `http://doi.wiley.com/10.1029/2001JB001617`, doi:`10.1029/2001JB001617`.

Ide, S., Matsubara, M., Obara, K., 2004.
Exploitation of high-sampling Hi-net data to study seismic energy scaling: The aftershocks of the 2000 Western Tottori, Japan, earthquake.
Earth, Planets and Space 56, 859–871.
doi:`10.1186/BF03352533`.

Igonin, N., Verdon, J.P., Kendall, J.M., Eaton, D.W., 2021.
Large-Scale Fracture Systems Are Permeable Pathways for Fault Activation During Hydraulic Fracturing.
Journal of Geophysical Research: Solid Earth 126, 1–19.
doi:`10.1029/2020JB020311`.

Imanishi, K., Ellsworth, W.L., Prejean, S.G., 2004.
Earthquake source parameters determined by the SAFOD Pilot Hole seismic array.
Geophysical Research Letters 31, 3–7.
doi:`10.1029/2004GL019420`.

Kanamori, H., Anderson, D., 1975.
Theoretical basis of some empirical relations in seismology.
Bulletin of the seismological society of America 65, 1073–1095.

Kanamori, H., Rivera, L., 2006.
Energy partitioning during an earthquake.
Geophysical Monograph Series 170, 3–13.
doi:`10.1029/170GM03`.

Kaneko, Y., Shearer, P.M., 2014.
cohesive-zone models of circular subshear rupture.
Geophysical Journal International 197, 1002–1015.
doi:`10.1093/gji/ggu030`.

Kao, H., Hyndman, R., Jiang, Y., Visser, R., Smith, B., Babaie Mahani, A., Leonard, L., Ghofrani, H., He, J., 2018.
Induced Seismicity in Western Canada Linked to Tectonic Strain Rate: Implications for Regional Seismic Hazard.
Geophysical Research Letters 45, 11,104–11,115.
doi:`10.1029/2018GL079288`.

Keranen, K., Weingarten, M., Bekins, B., Ge, S., 2014.
Sharp Increase in central Oklahoma seismicity since 2008 induced by massive wastewater injection.
Science 345.

Kettlety, T., Verdon, J.P., 2021.
Fault triggering mechanisms for hydraulic fracturing-induced seismicity from the preston new road, uk case study.
Frontiers in Earth Science 9, 382.

Kettlety, T., Verdon, J.P., Butcher, A., Hampson, M., Craddock, L., 2021.
High-resolution imaging of the ml 2.9 august 2019 earthquake in lancashire, united kingdom, induced by hydraulic fracturing during preston new road pnr-2 operations.
Seismological Society of America 92, 151–169.

Kettlety, T., Verdon, J.P., Werner, M.J., Kendall, J.M., 2020.
Stress Transfer From Opening Hydraulic Fractures Controls the Distribution of Induced Seismicity.
Journal of Geophysical Research: Solid Earth 125.
doi:10.1029/2019JB018794.

Kettlety, T., Verdon, J.P., Werner, M.J., Kendall, J.M., Budge, J., 2019.
Investigating the role of elastostatic stress transfer during hydraulic fracturing-induced fault activation.
Geophysical Journal International , 1200–1216doi:10.1093/gji/ggz080.

Kilb, D., Gomberg, J., Bodin, P., 2000.
Triggering of earthquake aftershocks by dynamic stresses.
Nature 408, 570–574.
doi:10.1038/35046046.

Kim, K.I., Min, K.B., Kim, K.Y., Choi, J.W., Yoon, K.S., Yoon, W.S., Yoon, B., Lee, T.J., Song, Y., 2018.
Protocol for induced microseismicity in the first enhanced geothermal systems project in pohang, korea.
Renewable and Sustainable Energy Reviews 91, 1182–1191.
URL: https://www.sciencedirect.com/science/article/pii/S1364032118302430, doi:https://doi.org/10.1016/j.rser.2018.04.062.

Klinger, A.G., Werner, M.J., 2021.
Microseismic source parameters from induced seismicity in the Horn river basin (British Columbia) [Dataset].

doi:10.5281/zenodo.5603088.

Klinger, A.G., Werner, M.J., 2022.
Stress drops of hydraulic fracturing induced microseismicity in the Horn River basin: Challenges at high frequencies recorded by borehole geophones.
Geophysical Journal International URL: https://doi.org/10.1093/gji/ggab458, doi:10.1093/gji/ggab458, arXiv:https://academic.oup.com/gji/advance-article-pdf/doi/10.1093/gji/g
ggab458.

Ktenidou, O.J., Cotton, F., Abrahamson, N.A., Anderson, J.G., 2014.
Taxonomy of κ: A review of definitions and estimation approaches targeted to applications.
Seismological Research Letters 85, 135–146.

Kwiatek, G., Bulut, F., Bohnhoff, M., Dresen, G., 2014.
High-resolution analysis of seismicity induced at Berlín geothermal field, El Salvador.
Geothermics 52, 98–111.
URL: http://dx.doi.org/10.1016/j.geothermics.2013.09.008, doi:10.1016/j.geothermics.2013.09.008.

Kwiatek, G., Martínez-Garzón, P., Dresen, G., Bohnhoff, M., Sone, H., Hartline, C., 2015.
Effects of long-term fluid injection on induced seismicity parameters and maximum magnitude in northwestern part of the geysers geothermal field.
Journal of Geophysical Research: Solid Earth 120, 7085–7101.

Kwiatek, G., Plenkers, K., Dresen, G., 2011.
Source parameters of picoseismicity recorded at Mponeng deep gold mine, South Africa: Implications for scaling relations.
Bulletin of the Seismological Society of America 101, 2592–2608.
doi:10.1785/0120110094.

Kwiatek, G., Saarno, T., Ader, T., Bluemle, F., Bohnhoff, M., Chendorain, M., Dresen, G., Heikkinen, P., Kukkonen, I., Leary, P., Leonhardt, M., Malin, P., Martínez-Garzón, P., Passmore, K., Passmore, P., Valenzuela, S., Wollin, C., 2019.
Controlling fluid-induced seismicity during a 6.1-km-deep geothermal stimulation in Finland.
Science Advances 5, 1–12.
doi:10.1126/sciadv.aav7224.

Lagarias, J.C., Reeds, J.A., Wright, M.H., Wright, P.E., 1998.
Convergence properties of the nelder–mead simplex method in low dimensions.
SIAM Journal on Optimization 9, 112–147.
doi:10.1137/S1052623496303470.

Lei, X., Huang, D., Su, J., Jiang, G., Wang, X., Wang, H., Guo, X., Fu, H., 2017. Fault reactivation and earthquakes with magnitudes of up to Mw4.7 induced by shale-gas hydraulic fracturing in Sichuan Basin, China. Scientific Reports 7, 7971. URL: https://doi.org/10.1038/s41598-017-08557-y, doi:10.1038/s41598-017-08557-y.

Lengliné, O., Lamourette, L., Vivin, L., Cuenot, N., Schmittbuhl, J., 2014. Journal of Geophysical Research : Solid Earth Fluid-induced earthquakes with variable stress drop , 1–14doi:10.1002/2014JB011282.Received.

Lin, Y.Y., Lapusta, N., 2018. Microseismicity Simulated on Asperity-Like Fault Patches: On Scaling of Seismic Moment With Duration and Seismological Estimates of Stress Drops. Geophysical Research Letters 45, 8145–8155. doi:10.1029/2018GL078650.

Lin, Y.Y., Ma, K.F., Kanamori, H., Alex Song, T.R., Lapusta, N., Tsai, V.C., 2016. Evidence for non-self-similarity of microearthquakes recorded at a Taiwan borehole seismometer array. Geophysical Journal International 206, 757–773. doi:10.1093/gji/ggw172.

Lior, I., Sladen, A., Mercerat, D., Ampuero, J.P., Rivet, D., Sambolian, S., 2021. Strain to ground motion conversion of distributed acoustic sensing data for earthquake magnitude and stress drop determination. Solid Earth 12, 1421–1442. doi:10.5194/se-12-1421-2021.

Lomax, A., Michelini, A., Curtis, A., 2009. Earthquake location, direct, global-search methods .

Luttrell, K., Hardebeck, J., 2021. A Unified Model of Crustal Stress Heterogeneity From Borehole Breakouts and Earthquake Focal Mechanisms. Journal of Geophysical Research: Solid Earth 126, 1–13. doi:10.1029/2020JB020817.

Madariaga, B.Y.R., 1976. Dynamics of an explanding circular fault. Bulletin of the Seismological Society of America 66, 639–665.

Mancini, S., Werner, M.J., Segou, M., Baptie, B., 2021. Probabilistic Forecasting of Hydraulic Fracturing-Induced Seismicity Using an Injection-Rate Driven ETAS Model doi:10.1785/0220200454.Supplemental.

Maxwell, S.C., 2014. Microseismic Imaging of Hydraulic Fracturing: Improved Engineering of Unconventional shale Reservois, Society of Exploration Geophysicists, SEG Books, 212 p. 17.

McGarr, A., 1999. On relating apparent stress to the stress causing earthquake fault slip. Journal of Geophysical Research: Solid Earth 104, 3003–3011.

McGarr, A., 2014. Journal of Geophysical Research : Solid Earth. AGU: Journal of Geophysical Research, Solid Earth 119, 3678–3699. doi:10.1002/2013JB010597.Received.

Moos, D., Zoback, M.D., 1990. Utilization of observations of well bore failure to constrain the orientation and magnitude of crustal stresses: application to continental, Deep Sea Drilling Project, and Ocean Drilling Program boreholes. Journal of Geophysical Research 95, 9305–9325. doi:10.1029/JB095iB06p09305.

Moyer, P.A., Boettcher, M.S., McGuire, J.J., Collins, J.A., 2018. Spatial and temporal variations in earthquake stress drop on gofar transform fault, east pacific rise: Implications for fault strength. Journal of Geophysical Research: Solid Earth 123, 7722–7740.

Mueller, C.S., 1985. Source pulse enhancement by deconvolution of an empirical green's function. Geophysical Research Letters 12, 33–36.

Nadeau, R.M., McEvitty, T.V., 2004. Periodic Pulsing of Characteristic Microearthquakes on the San Andreas Fault. Science 303, 220–222. doi:10.1126/science.1090353.

Nantanoi, S., Rodríguez-Pradilla, G., Verdon, J., 2021. 3d-seismic interpretation and fault slip potential analysis from hydraulic fracturing in the bowland shale, uk. Petroleum Geoscience .

Oil, B.C., Commission, G., 2012.
Investigation of Observed Seismicity in the Horn River Basin .

Onwuemeka, J., Liu, Y., Harrington, R.M., 2018.
Earthquake Stress Drop in the Charlevoix Seismic Zone, Eastern Canada.
Geophysical Research Letters 45, 12,226–12,235.
doi:10.1029/2018GL079382.

Pearson, C., 1981.
The Relationship Between Microseismicity and High Pore Pressures During Hydraulic Stimulation Experiments in Low Permeability Granitic Rocks.
Journal of Geophysical Research 86, 7855–7864.

Pettitt, W., Montes, J.R., Hemmings, B., Hughes, E., Young, R.P., et al., 2009.
Using continuous microseismic records for hydrofracture diagnostics and mechanics, in: 2009 SEG Annual Meeting, Society of Exploration Geophysicists.

Podvin, P., Lecomte, I., 1991.
Finite difference computation of traveltimes in very contrasted velocity models: a massively parallel approach and its associated tools.
Geophysical Journal International 105, 271–284.
doi:10.1111/j.1365-246X.1991.tb03461.x.

Prieto, G.A., Parker, R.L., Thomson, D.J., Vernon, F.L., Graham, R.L., 2007.
Reducing the bias of multitaper spectrum estimates.
Geophysical Journal International , 1269–1281doi:10.1111/j.1365-246X.2007.03592.x.

Prieto, G.A., Shearer, P.M., Vernon, F.L., Kilb, D., 2004.
Earthquake source scaling and self-similarity estimation from stacking P and S spectra.
Journal of Geophysical Research B: Solid Earth 109, 1–13.
doi:10.1029/2004JB003084.

Raleigh, C.B., Healy, J.H., Bredehoeft, J.D., 1976.
An experiment in earthquake control at Rangely, Colorado.
Science 191, 1230–1237.
doi:10.1126/science.191.4233.1230.

Ross, Z.E., Meier, M.A., Hauksson, E., Heaton, T.H., 2018.
Generalized seismic phase detection with deep learning.
Bulletin of the Seismological Society of America 108, 2894–2901.
doi:10.1785/0120180080, arXiv:1805.01075.

Rubinstein, J.L., Mahani, A.B., 2015.
Myths and facts on wastewater injection, hydraulic fracturing, enhanced oil recovery, and induced seismicity.
Seismological Research Letters 86, 1060–1067.
doi:10.1785/0220150067.

Ruhl, C.J., Abercrombie, R.E., Smith, K.D., 2017.
Spatiotemporal Variation of Stress Drop During the 2008 Mogul, Nevada, Earthquake Swarm.
Journal of Geophysical Research: Solid Earth 122, 8163–8180.
doi:10.1002/2017JB014601.

Sato, T., Hirasawa, T., 1973.
Body wave spectra from propagating shear cracks.
Journal of Physics of the Earth 21, 415–431.

Sayers, C., Den Boer, L., Dasgupta, S., Goodway, B., 2015.
Anisotropy estimate for the Horn River Basin from sonic logs in vertical and deviated wells.
Leading Edge 34, 296–306.
doi:10.1190/tle34030296.1.

Sayers, C., Lascano, M., Gofer, E., Boer, L.D., Walz, M., Hannan, A., Dasgupta, S., Goodway, W., Perez, M., Purdue, G., 2016.
Geomechanical model for the Horn River Formation based on seismic AVA inversion.
SEG-2016-13711507.

Schoenball, M., Davatzes, N.C., 2017.
Quantifying the heterogeneity of the tectonic stress field using borehole data.
Journal of Geophysical Research: Solid Earth 122, 6737–6756.
doi:10.1002/2017JB014370.

Sharma, M.L., Wason, H.R., 1994.
Occurrence of low stress drop earthquakes in the Garhwal Himalaya region.
Physics of the Earth and Planetary Interiors 85, 265–272.
doi:10.1016/0031-9201(94)90117-1.

Shearer, P.M., 2009.
Introduction to Seismology.
Cambridge University press, New York.

Shearer, P.M., Abercrombie, R.E., Trugman, D.T., Wang, W., 2019.
Comparing EGF Methods for Estimating Corner Frequency and Stress Drop From P Wave Spectra.

Journal of Geophysical Research: Solid Earth 124, 3966–3986. doi:10.1029/2018JB016957.

Simpson, D.W., Leith, W., 1985. The 1976 and 1984 Gazli, USSR, earthquakes - Were they induced? Bulletin of the Seismological Society of America 75, 1465–1468.

Sleefe, G., Warpinski, N., Engler, 1993. Observations of broad-band micro-seisms during reservoir stimulation. SEG .

Sleefe, G., Warpinski, N., Engler, B., et al., 1995. The use of broadband microseisms for hydraulic fracture mapping. SPE Formation Evaluation 10, 233–240.

Snee, J.E.L., Zoback, M.D., 2018. State of stress in the permian basin, texas and new mexico: Implications for induced seismicity. The Leading Edge 37, 127–134.

Stein, R.S., 1999. The role of stress transfer in earthquake occurence. Nature 402, 605–609.

Streit, J.E., 1997. Low frictional strength of upper crustal faults: A model. Journal of Geophysical Research B: Solid Earth 102, 24619–24626. doi:10.1029/97jb01509.

Sumy, D.F., Neighbors, C.J., Cochran, E.S., Keranen, K.M., 2017. Low stress drops observed for aftershocks of the 2011 Mw 5.7 Prague, Oklahoma, earthquake. Journal of Geophysical Research: Solid Earth 122, 3813–3834. doi:10.1002/2016JB013153.

Sun, R., McMechan, G.A., 1988. Nonlinear reverse-time inversion of elastic offset vertical seismic profile data. Geophysics 53, 1295–1302.

Tan, Y., Hu, J., Zhang, H., Chen, Y., Qian, J., Wang, Q., Zha, H., Tang, P., Nie, Z., 2020. Hydraulic Fracturing Induced Seismicity in the Southern Sichuan Basin Due to Fluid Diffusion Inferred From Seismic and Injection Data Analysis. Geophysical Research Letters 47, 1–10. doi:10.1029/2019GL084885.

Tary, J.B., van der Baan, M., Eaton, D., 2014.
Journal of Geophysical Research : Solid Earth.
AGU: Journal of Geophysical Research, Solid Earth 120, 1195–1209.
doi:10.1002/2014JB011376.Received.

Tomic, J., Abercrombie, R.E., do Nascimento, A.F., 2009.
Source parameters and rupture velocity of small M 2.1 reservoir induced earthquakes.
Geophysical Journal International 179, 1013–1023.
doi:10.1111/j.1365-246X.2009.04233.x.

Trugman, D.T., 2020.
Stress-Drop and Source Scaling of the 2019 Ridgecrest, California, Earthquake Sequence.
Bulletin of the Seismological Society of America , 1859–1871doi:10.1785/0120200009.

Trugman, D.T., Shearer, P.M., 2017.
Application of an improved spectral decomposition method to examine earthquake source scaling in Southern California.
Journal of Geophysical Research: Solid Earth 122, 2890–2910.
doi:10.1002/2017JB013971.

US Energy Information Administration, 2013.
Shale Gas Resources: An Assessment of 137 Shale Formations in 41 Countries Outside the United States.
Technically recoverable shale oil and shale gas resources: An assessment of 137 shale formations in 41 countries outside the United States: Washington, DC , 76.

Vaezi, Y., Van der Baan, M., 2014.
Analysis of instrument self-noise and microseismic event detection using power spectral density estimates.
Geophysical Journal International 197, 1076–1089.
doi:10.1093/gji/ggu036.

Van Der Baan, M., 2009.
The origin of sh-wave resonance frequencies in sedimentary layers.
Geophysical Journal International 178, 1587–1596.

Venkataraman, A., Kanamori, H., 2004.
Observational constraints on the fracture energy of subduction zone earthquakes.
Journal of Geophysical Research: Solid Earth 109.
doi:10.1029/2003JB002549.

Venkataranman, A., Beroza, G.C., Ide, S., Imanishi, K., Ito, H., Iio, Y., 2006.

Measurements of spectral similarity for microearthquakes in western Nagano, Japan.
Journal of Geophysical Research: Solid Earth 111, 1–10.
doi:10.1029/2005JB003834.

Verdon, J., Kettlety, T., 2020.
Geomechanical Interpretation of Induced Seismicity at the Preston New Road PNR-2 Well , Lancashire , England April 2020 .

Verdon, J.P., Bommer, J.J., 2021.
Green, yellow, red, or out of the blue? An assessment of Traffic Light Schemes to mitigate the impact of hydraulic fracturing-induced seismicity.
Journal of Seismology 25, 301–326.
doi:10.1007/s10950-020-09966-9.

Verdon, J.P., Budge, J., 2018.
Examining the capability of statistical models to mitigate induced seismicity during hydraulic fracturing of shale gas reservoirs.
Bulletin of the Seismological Society of America 108, 690–701.
doi:10.1785/0120170207.

Verdon, J.P., Kendall, J.M., Stork, A.L., Chadwick, R.A., White, D.J., Bissell, R.C., 2013.
Comparison of geomechanical deformation induced by megatonne-scale co2 storage at sleipner, weyburn, and in salah.
Proceedings of the National Academy of Sciences 110, E2762–E2771.
URL: https://www.pnas.org/content/110/30/E2762, doi:10.1073/pnas.1302156110, arXiv:https://www.pnas.org/content/110/30/E2762.full.pdf.

Viegas, G., Abercrombie, R.E., Kim, W.Y., 2010.
The 2002 M5 Au Sable Forks, NY, earthquake sequence: Source scaling relationships and energy budget.
Journal of Geophysical Research: Solid Earth 115, 1–20.
doi:10.1029/2009JB006799.

Waldhauser, F., Ellsworth, W.L., 2000.
A Double-difference Earthquake location algorithm: Method and application to the Northern Hayward Fault, California.
Bulletin of the Seismological Society of America 90, 1353–1368.
doi:10.1785/0120000006.

Walsh, F.R., Zoback, M.D., 2016.
Probabilistic assessment of potential fault slip related to injectioninduced earthquakes: Application to north-central Oklahoma, USA.

Geology 44, 991–994.
doi:10.1130/G38275.1.

Walsh, F.R.I., Zoback, M.D., Pais, D., Weingarten, M., Tyrell, T., 2017.
FSP 1.0: A Program for Probabilistic Estimation of Fault Slip Potential Resulting From Fluid Injection , 46URL: https://scits.stanford.edu/software.

Wang, R., Gu, Y.J., Schultz, R., Chen, Y., 2018.
Faults and Non-Double-Couple Components for Induced Earthquakes.
Geophysical Research Letters 45, 8966–8975.
doi:10.1029/2018GL079027.

Wilson, T.K., 2019.
Basin Modelling and Thermal History of the Horn River and Liard Basins , Cordova Embayment , and Adjacent Parts of the Western Canada Sedimentary Basin , 1–20.

Wu, Q., Chapman, M., 2017.
Stress-drop estimates and source scaling of the 2011 mineral, Virginia, mainshock and aftershocks.
Bulletin of the Seismological Society of America 107, 2703–2720.
doi:10.1785/0120170098.

Wu, Q., Chapman, M., Chen, X., 2018.
Stress-drop variations of induced earthquakes in Oklahoma.
Bulletin of the Seismological Society of America 108, 1107–1123.
doi:10.1785/0120170335.

Yaskevich, S., Duchkov, A.A., Myasnikov, A., 2019.
A case study on receiver-clamping quality assessment from the seismic-interferometry processing of downhole seismic noise recordings.
Geophysics 84, B195–B203.
doi:10.1190/geo2018-0293.1.

Yenier, E., Atkinson, G.M., 2015.
An equivalent point-source model for stochastic simulation of earthquake ground motions in California.
Bulletin of the Seismological Society of America 105, 1435–1455.
doi:10.1785/0120140254.

Yoon, S.H., Joe, Y.J., Koh, C.S., Woo, J.H., Lee, H.S., 2018.
Sedimentary processes and depositional environments of the gas-bearing Horn River shale in British Columbia, Canada.

Geosciences Journal 22, 33–46. doi:10.1007/s12303-017-0053-1.

York, D., Evensen, N.M., Martınez, M.L., De Basabe Delgado, J., 2004. Unified equations for the slope, intercept, and standard errors of the best straight line. American Journal of Physics 72, 367–375.

Yoshida, K., Saito, T., Urata, Y., Asano, Y., Hasegawa, A., 2017. Temporal Changes in Stress Drop, Frictional Strength, and Earthquake Size Distribution in the 2011 Yamagata-Fukushima, NE Japan, Earthquake Swarm, Caused by Fluid Migration. Journal of Geophysical Research: Solid Earth 122, 10,379–10,397. doi:10.1002/2017JB014334.

Yu, H., Harrington, R.M., Kao, H., Liu, Y., Abercrombie, R.E., Wang, B., 2020. Well Proximity Governing Stress Drop Variation and Seismic Attenuation Associated with Hydraulic Fracturing Induced Earthquakes. Journal of Geophysical Research: Solid Earth , 1–17doi:10.1029/2020jb020103.

Zhang, H., Eaton, D.W., Li, G., Liu, Y., Harrington, R.M., 2016. Discriminating induced seismicity from natural earthquakes using moment tensors and source spectra. Journal of Geophysical Research: Solid Earth 121, 972–993. doi:10.1002/2015JB012603.

Zhang, Z., Rector, J.W., Nava, M.J., 2018. Microseismic hydraulic fracture imaging in the Marcellus Shale using head waves. Geophysics 83, KS1–KS10. doi:10.1190/geo2017-0184.1.

Zoback, M.D., 2009. Rock failure in compression, tension and shear. doi:10.1017/cbo9780511586477.005.